

UNIVERSITY OF OKLAHOMA

GRADUATE COLLEGE

COMPUTATIONAL STUDY OF LIQUID-SOLID INTERFACE

A DISSERTATION

SUBMITTED TO THE GRADUATE FACULTY

In partial fulfillment of the requirements for the

Degree of

DOCTOR OF PHILOSOPHY

By

Guobing Zhou

Norman, Oklahoma

2020

COMPUTATIONAL STUDY OF LIQUID-SOLID INTERFACE
A DISSERTATION APPROVED FOR THE
SCHOOL OF CHEMICAL, BIOLOGICAL, AND MATERIALS ENGINEERING

BY THE COMMITTEE CONSISTING OF

Dr. Liangliang Huang, Chair

Dr. Dimitrios V. Papavassiliou

Dr. Jeffrey H. Harwell

Dr. Wang Bin

Dr. Yihan Shao

© Copyright by Guobing Zhou 2020
All Rights Reserved

Acknowledgements

Foremost, I would like to express my sincere gratitude to my advisor Dr. Liangliang Huang for the continuous support of my PhD study and research, and for his supervision and guidance over the past four years at University of Oklahoma. Dr. Huang is an open-minded advisor who can always listen to my thoughts and give me very useful feedback and suggestions. His enthusiasm and concentration on teaching and research always inspire me and I really benefit a lot from working with him. His kindness and dedication to students makes me really enjoy the four-year PhD study. Also, He always encourages me to get out of my comfort zone and creatives opportunities for me to communicate with other people. Beyond the study and research, he also gives me great support on a personal level and shares his experience with me, which makes me feel that he is not only a great academic research advisor but also an intimate friend. I am a leaf of his academic tree, and continue to grow under his guidance.

I would also like to thank my committee members, Dr. Dimitrios V. Papavassiliou, Dr. Jeffrey H. Harwell, Dr. Wang Bin, and Dr. Yihan Shao for their patience and insightful comments on the examinations and my research projects, especially during the final defense.

I am also grateful to Dr. Zhen Yang at Jiangxi Normal University for his help in my research, and particularly in my marriage and job seeking.

I also want to thank Dr. Chang Liu at Nanjing University of Technology, and Dr. Rong An at Nanjing University of Science and Technology, Dr. Yan Song (now at Nanjing University) and Yao An at the University of North Carolina at Chapel Hill for sharing exciting experimental results. I learned a lot from them and I am so proud of the publications that we have put together. Also, I

want to express my special thanks to Prof. Xiaohua Lu and Prof. Xin Feng at Nanjing University of Technology for their encouragement.

I also want to thank Qiao “Jennifer” Qi, currently a PhD student also advised by Dr. Huang, for her help in reactive molecular dynamics simulations. Particularly thank her help in my tough time when I first came to the university. I would like to thank Garrett Tow, Trevor Fisher, and Bradley Schoen for the interesting discussions of my research.

I would also like to thank my friends, Tong Mou, Yu Yan, Hao Xiong, Hao Li, Dawei Wang, Quanquan Zhou, Jianwen Teng, Yongping Zhang, Qiang Zheng, and other friends now in China, for their company over the four years. Their friendship gives me a lot of power and makes my journey easier. Wherever I run into trouble or encounter setbacks, they always stand up for me and help me overcome the tough time.

Finally, I want to thank my wife, my parents, my parents-in-law, my sister and other family members for their unconditional support and trust. I love all of you.

The work presented in this dissertation is supported by grants from the National Science Foundation (Grant CHE-1710102). I am very grateful for the supercomputer resource provided by the OU Supercomputing Center for Education & Research (OSCER) at University of Oklahoma.

Contents

Acknowledgements.....	iv
List of Tables	viii
List of Figures.....	ix
Abstract.....	xiv
Chapter 1: Introduction.....	1
1.1. Solid Interfaces	1
1.2 Self-Assembled Monolayers on Metal Surfaces.....	2
1.3 Water models	4
1.4 Water on Metal Surfaces.....	6
1.5 Water on Metal Oxide Surfaces.....	9
1.6 Ionic liquid.....	11
1.7 Research Approach.....	13
1.8 References.....	14
Chapter 2: Computational Methods.....	28
2.1 Density Functional Theory	28
2.2 Molecular Dynamics Simulation	33
2.3 Computational Characterizations.....	38
2.4 Reference	41
Chapter 3: Force Field Parameter Development for the Thiolate/Defective Au(111) Interface* 51	
3.1 Introduction.....	51
3.2 Methods and Simulation Details.....	53
3.3 Results and Discussions.....	57
3.4 Force Field Validation	63
3.5 Conclusions.....	71
3.6 References.....	72
Chapter 4: First Adsorbed Water Layer and its Wettability Transition under Compressive Lattice Strain*	79
4.1 Introduction.....	79
4.2 Models and Simulation Details.....	81
4.3 Results and Discussions.....	84

4.4 Conclusion	96
4.5 References.....	97
Chapter 5: Molecular Dynamics Simulation of First Adsorbed Water Layer at Titanium Dioxide Surfaces*	102
5.1 Introduction.....	102
5.2 Simulation Methods and Details.....	104
5.3 Results and Discussions.....	107
5.4 Conclusions.....	122
5.5 References.....	124
Chapter 6: Interfacial Potassium Induced Enhanced Raman Spectroscopy for Single-Crystal TiO ₂ Nanowhisker*	133
6.1 Introduction.....	133
6.2 Experimental.....	135
6.3 Results and discussion	137
6.4 Conclusions.....	148
6.5 References.....	148
Chapter 7: Friction of Ionic Liquid–Glycol Ether Mixtures at Titanium Interfaces: Negative Load Dependence*.....	152
7.1 Introduction.....	152
7.2 Experiments and Simulations	154
7.3 Results and Discussion	158
7.4 Conclusions.....	171
7.5 References.....	172
Chapter 8: Conclusions and Outlook	178
8.1 Conclusions.....	178
8.2 Outlook	181

List of Tables

Table 1. The Lennard-Jones parameters and partial atomic charges used in this work.	55
Table 2. Typical vibrational frequency of various modes of staple motif and bridge models.	58
Table 3. Bond stretching potential parameters for staple motif and bridge models.	59
Table 4. Angle bending potential parameters for staple motif and bridge models.	60
Table 5. Torsion parameters for both staple motif and bridge models.	62
Table 6. The average tilt angle, azimuthal angle, and film thickness for the alkane chains in model A, B, and C from MD and AIMD calculations at 300 K.	70
Table 7. Lattice constant and water-water distance in FAWL on metal surfaces with various strains. Note: green and yellow refer to the FAWL with hydrophobic and hydrophilic features, respectively.	88
Table 8. Average number of HBs of the FAWL with: (A) substrate, (B) FAWL, and (C) other water. The calculated HB number for bulk water is 3.58.	119
Table 9. Normal loads and diffusion coefficients of [P _{4,4,4,8}][BScB] confined in the slit pore (between tip and substrate), calculated by MD simulations.	169

List of Figures

Figure 1. The general shape for different water models.	5
Figure 2. Chemical structures of the typical IL cations and anions. (a) Cations: imidazolium, pyridinium, pyrrolidinium, phosphonium, ammonium, and sulfonium, and (b) Anions: alkylsulfate, tosylate, methanesulfonate, bis(trifluoromethyl-sulfonyl)imide, hexafluorophosphate, tetrafluorob-	12
Figure 3. Schematic illustration for (a) cylindrical bin by dividing the water droplet, (b) volume element by dividing the cylindrical bin shown in (a) and (c) fitting of the air-water interface and the contact angle calculation.	38
Figure 4. Top view (upper panel) and side view (lower panel) of the optimized structures for the staple motif (a, c) and the bridge (b, d) models. Color code: Au, gold; S, yellow; C, gray; H, white.	56
Figure 5. Torsion energy profiles from MD and DFT calculations: (a) Au(a)-S(m)-C-C, (b) Au(s)-S(m)-C-C, (c) Au(a)-S(m)-C-H, (d) Au(s)-S(m)-C-H of the staple motif model; (e) Au(s)-S(b)-C-C and (f) Au(s)-S(b)-C-H of the bridge model. Note: A small interval of 5° was used around the equilibrium dihedral value.	61
Figure 6. Atomistic structures for three Au-S interface models with a $(2\sqrt{3}\times 3)$ unit cell including four $C_{10}S$ thiolate molecules on the Au(111) surface. Note: the C and H atoms are not shown for clarity. Au(s), Au(a), S(m), and S(b) correspond to the Au atom in the substrate, Au adatom, S atom in the staple motif, and S atom in the bridge model.	63
Figure 7. The average bond length for characteristic bonds in (a) model A and B and (b) model C from MD and AIMD calculations at 300 K. All standard deviations are less than $\pm 0.05 \text{ \AA}$. The error bars are smaller than the symbol size, therefore not shown.	64
Figure 8. The average angle values for various angles in (a) model A and B and (b) model C from MD and AIMD calculations at 300 K. All standard deviations are less than $\pm 1.5^\circ$. The error bars are smaller than the symbol size, so they are not shown.	65
Figure 9. Density distributions of the C atoms in alkane chain along the z-direction for (a) model A, (b) model B, and (c) model C at 300.0 K.	68
Figure 10. Density distributions of the C atoms in alkane chain along the z direction for (a) molecule 1, (b) molecule 2, (c) molecule 3, and (d) molecule 4 in model C at 200.0 K.	69
Figure 11. A schematic illustration to the compressive strain applied in the simulations.	81

Figure 12. The equilibrium configuration of a 1.0 nm water film on (a) Pd(100); (b) Au(100). An ordered first adsorbed water layer was observed on both surfaces but with significantly different wettability properties: hydrophobic for Pd(100); hydrophilic for Au(100)..... 85

Figure 13. Equilibrium configurations of a 1.0 nm water film on metal surfaces under compressive strains: (a) Pd(100); (b) Au(100). 0% strain represents a pristine metal surface. Strains up to 5% have been studied, corresponding to ~0.3 GPa to Au and ~5.0 GPa to Pd, respectively; (c) Calculated contact angles to water droplets at Pd(100) and Au(100) surfaces; (d) Interaction energies between the FAWL and the metal surfaces. All standard deviations are less than $\pm 2.73^\circ$ 87

Figure 14. Schematic illustration of the simulation system in of a bimetallic junction model. First, two separate metal surfaces, Pd(100) and Au(100), were prepared and then the Au(100) surface is uniformly compressed in the Y direction (4.61% strain) to match the lattice constant of Pd(100). A water film of 1.0 nm was placed on the obtained bimetallic junction. Side and top views of (a) initial simulation box; (b) the simulation box at equilibrium where a water droplet is on the top of the compressive Au(100) region. 90

Figure 15. (a) Lateral density distribution of Ow-Ow for water molecules of the FAWL from both the pristine Pd(100) and compressed Au(100) regions; (b) Probability of dipole distribution angle θ , which is defined as the angle between the projection of dipole moment in the x-y plane and the unit vector along the x direction; (c) Probability of O-H bond distribution angle ϕ , formed by the O-H bond and the unit vector normal to the metal substrate; (d) Orientation distribution of water in the FAWL as a function of height h above the substrate and angle formed by the O-H bond and the surface normal vector. Note: the insets of (b) and (c) show schematic illustrations to θ and ϕ angles. Note: the P-Pd(100) and C-Au(100) refer to the pristine Pd(100) and compressed Au(100) surfaces, respectively. 91

Figure 16. (a) Continuous time correlation functions (TCFs), $S_{HB}(t)$, for the HB network formed within the FAWL on pristine Pd(100) and compressed Au(100) surfaces; (b) The second-order reorientational TCF $C_2(t)$ for water molecules in the FAWL of pristine Pd(100) and compressed Au(100). Note: the P-Pd(100) and C-Au(100) refer to the pristine Pd(100) and compressed Au(100) surfaces, respectively. 93

Figure 17. Free energy profile of water molecules in the FAWL of pristine Pd(100) and compressed Au(100) regions. The dash line indicates the boundary of the two regions. Note: the

P-Pd(100) and C-Au(100) refer to the pristine Pd(100) and compressed Au(100) surfaces, respectively.	95
Figure 18. Density distribution of water molecules at different TiO ₂ surfaces along the z direction.	108
Figure 19. Top view of the FAWL on the TiO ₂ -B (001) surface at t =20.0 ns: HB assisted water clusters. The HBs are in green, while the Ti and O atoms are colored by gray and blue, respectively.	111
Figure 20. Angular distribution of the FAWL at TiO ₂ surfaces: u ₁ is the unit vector normal to the surface; u ₂ is the vector pointing from O atom to H atom; θ is the angle defining the two vectors.	112
Figure 21. Fourier transformation vibrational spectra analysis of the hydrogen atoms of FAWL at (a) Rutile (110), (b) Rutile (011), (c) TiO ₂ -B (100), and (d) TiO ₂ -B (001) surfaces. For comparison, the result from pure water is also shown.	116
Figure 22. The analysis of averaged HBs between: (a) FAWL-substrate; (b) FAWL-FAWL; (c) FAWL-other water. Note: in the system of TiO ₂ -B (001), the percentage of more than 2.0 HB is included in the percentage of 2.0 HB for clarity.....	118
Figure 23. Continuous time correlation function $S_{HB}(t)$ for HB network between (a) FAWL-substrate and (b) FAWL-other water on different TiO ₂ surfaces. The inset in (a) is the $S_{HB}(t)$ for HB network between FAWL-FAWL on TiO ₂ -B (001) surface. For comparison, the result from bulk water is also shown.	122
Figure 24. Schematic diagram of TiO ₂ nanowhisker preparation.....	136
Figure 25. Morphology, crystal structure and SERS properties of four TiO ₂ nanowhisker samples. (a) SEM images of Z700, Z800, Z900 and Z1000. (b) XRD pattern of four TiO ₂ nanowhiskers. (c) Raman spectra of the 10 ⁻⁵ M MB ethanol solution on four TiO ₂ nanowhiskers and bare glass (inset: the 1630 cm ⁻¹ intensity of four nanowhiskers). (d) Raman EFs obtained for MB on the Z900 sample, as a function of MB concentrations at the 1630 cm ⁻¹ peak. (e) The detection limitation test of MB on the Z900 sample.....	138
Figure 26. Morphology, Remote SERS and SERS performance of TiO ₂ samples. SEM images of Z700 (a), ZB700 (b) and T700(c). The propagation of light along TiO ₂ nanowhisker (Z700) under visible light (d) and laser (e). (f) Raman spectra of MB (10 ⁻⁵ M) adsorbed on T700, ZB 700 and Z700 samples.	140

Figure 27. UV–vis DRS spectra of (a) TiO ₂ nanowhiskers and (b) Z900 compared with pristine Z900 and MB. XPS spectra and binding energies of (c) titanium, (d) oxygen and (e) potassium. (f) Zeta potential as a function of pH: the comparison between four studied TiO ₂ nanowhiskers and the commercial P25 sample.	141
Figure 28. Comparing Raman spectra of bulk dye and SERS spectra of 10 ⁻⁵ M dye solution adsorbed on Z700. (a Crystal violet, insert: CV structure; b Methyl orange, insert: MO structure.)	143
Figure 29. Potassium treated TiO ₂ particles and their SERS performance. (a) Raman spectra of commercial TiO ₂ particles doped with different content of potassium (0.14, 0.26, 0.50 and 2.45 wt %) and (b) SERS spectra of MB (10 ⁻⁵ M) on TiO ₂ particles.	144
Figure 30. The K-coated TiO ₂ model via K ₂ O dissociative adsorption at the anatase (001) surface. (a) side and top views of the initial configuration, where a 2 × 2 K ₂ O (001) supercell is placed on top of a 4-layer anatase (001) surface; (b) side and top views of the equilibrium K-coated TiO ₂ model at 300 K; (c) side and top views of the equilibrium K-coated TiO ₂ model at 1000 K. Color code: purple, potassium; red, oxygen; gray, titanium.	146
Figure 31. Bader charge analysis for the interfacial potassium and oxygen sites: potassium carries a positive while the oxygen sites have negative charges. For charity, only the interfacial charge information is displayed. The bottom TiO ₂ structures is shown by a line model and the charge information is not shown. Colour code: purple, potassium; red, oxygen.	147
Figure 32. Illustration and connection map of AFM experiments and theoretical simulations.	155
Figure 33. Structures of two cations, [P _{4,4,4,8}] ⁺ and [P _{6,6,6,14}] ⁺ ; four anions, [BOB] ⁻ , [BMB] ⁻ , [DCA] ⁻ , and [BScB] ⁻ ; base oil DEGDBE. Color codes are: P (black), B (olive), C (blue), H (gray), O (orange), N (navy).	158
Figure 34. Friction measurements for (a) the IL/oil mixtures coated Ti interfaces, where 75 wt% of ILs, namely, [P _{6,6,6,14}][BOB], [P _{6,6,6,14}][BMB], [P _{6,6,6,14}][DCA], [P _{4,4,4,8}][BScB], and [P _{6,6,6,14}][BScB], have been studied; (b) bare Ti and base oil lubricated Ti interfaces.	161
Figure 35. XPS spectra of [P _{4,4,4,8}][BScB]-oil mixtures at Ti interfaces, before ([P _{4,4,4,8}][BScB]-B) and after ([P _{4,4,4,8}][BScB]-A) AFM friction measurements: a) survey, b) high resolution C 1s scans. .	162
Figure 36. Topographic images of [P _{4,4,4,8}][BScB]-oil mixtures at Ti interfaces at a) smaller normal load of 9.6 nN and b) larger normal load of 76.6 nN.	163

Figure 37. Typical friction loops taken for $[P_{4,4,4,8}][BScB]$ with concentration of 75 wt% in oil at Ti interfaces at two different normal loads (F_N). Friction values, here given in V, are calculated as the average difference for each interfaces, in the friction loop between the back and forth scans. The back-and-forth displacement is in the directions indicated by black arrows. 164

Figure 38. Friction as a function of normal load in the $[P_{4,4,4,8}][BScB]$ case, from NEMD simulations. 165

Figure 39. Orientational probabilities of (a) the angle θ between the interface normal vector z and the alkyl chain vector P_{4-1} , P_{4-2} , P_{4-3} , P_8 in the cation $[P_{4,4,4,8}]^+$ (left) around the tip and (right) in the bulk system, (b) the angle ψ between the interface normal vector z and the vector B_1 , B_2 in the anion $[BScB]^-$ (left) around the tip and (right) in the bulk system. The insets in right panels of (a) and (b) show the vector definition for the orientation analysis of cation and anion, respectively. 166

Figure 40. (a) and (b) are the sketch map showing the main orientations of P_{4-1} , P_{4-2} , P_{4-3} , P_8 in the cation $[P_{4,4,4,8}]^+$, and B_1 , B_2 in the anion $[BScB]^-$, respectively. Here hydrogen atoms were not shown in (a) and (b) to make the illustration more clear. 167

Figure 41. The tree of dissertation outline with the color codes: black-the keyword for the topic; blue-the computational method; red-the chapter number. 178

Abstract

The solid interface is of fundamental importance to numerous scientific and technological fields, such as heterogeneous catalysis, water splitting, electrochemistry, corrosion, drug delivery, tribology, and wetting. However, there is still limited knowledge of the structures and properties of the first adsorbed monolayer at distinct solid interfaces. We perform theoretical calculations to study the interactions between the solid surfaces and the first adsorbed monolayer at the interface, to understand from the electronic/atomic levels how the properties of solid surface influence the adsorption of the first monolayer at the solid interfaces.

In Chapter 3, we developed the force field parameter for the thiolate/defective Au(111) interface. A molecular-level understanding of the interplay between self-assembled monolayers (SAMs) of thiolates and gold surface is of great importance to a wide range of applications in surface science and nanotechnology. Despite theoretical research progress of the past decade, an atomistic model, capable of describing key features of SAMs at reconstructed gold surfaces, is still missing. We carried out the periodic ab initio density functional theory (DFT) calculations to develop a new atomistic force field model for alkanethiolate SAMs on a reconstructed Au(111) surface. Based on the newly-developed force field parameters, the molecular dynamics (MD) simulations showed that the geometrical features of the investigated Au–S interface models and structural properties of the C₁₀S SAMs are in good agreement with the ab initio MD studies.

In Chapter 4, we investigate the wettability transition of the first adsorbed water layer (FAWL) on metal surfaces under a compressive lattice strain. A molecular-level description of a near-surface water structure and a handy manipulation of its properties are relevant to a broad range of scientific and technological phenomena. Through a series of MD simulations, we report the observation and characterization of a low-mobility FAWL and its tunable wetting transition at

three metal surface models. The results reveal that (i) there is a formation of the FAWL, resulting from competitive water–water hydrogen bonding and water–solid interactions, which in turn dictates the wettability at water–metal interfaces, (ii) applying compressive lattice strain to metal substrates can induce interfacial wettability transition, and (iii) by adjusting the lattice strains, the bimetallic junction can host a switchable wettability transition.

In Chapter 5, we study the structures and dynamics of the FAWL at distinct titanium dioxide (TiO_2) surfaces. The behavior of the FAWL at TiO_2 surfaces is critical to the fundamental understanding of TiO_2 -based applications. Using classical MD simulations, we study the properties of FAWL at four TiO_2 surfaces, including the density profile, the angular orientation distribution, the HB structural and dynamic properties, and the vibrational spectra of water molecules in the FAWL. The calculation results demonstrate that the water molecules show distinct adsorption structures and HB properties at the studied TiO_2 surfaces, leading to completely different vibrational signatures for the OH groups.

In Chapter 6, we explore the role of interfacial potassium on the surface-enhanced Raman spectroscopy for single-crystal TiO_2 nanowhisker by combining experiments and theoretical calculations. For TiO_2 -based surface-enhanced Raman spectroscopy (SERS) substrates, maintaining a good crystallinity is critical to achieving excellent Raman scattering. we report the successful synthesis of TiO_2 nanowhiskers with excellent SERS properties. The enhancement factor, an index of SERS performance, is 4.96×10^6 for methylene blue molecule detecting, with a detection sensitivity around $10^{-7} \text{ mol} \cdot \text{L}^{-1}$. The DFT calculations reveal that interfacial potassium can form a monolayer structure on the TiO_2 surface, resulting in a negatively charged TiO_2 nanowhisker surface. Such structures would promote the adsorption of methylene blue molecules and thereby significantly improves SERS performance via the electrostatic adsorption effect.

In Chapter 7, we investigate the friction of ionic liquid (IL)–glycol ether mixtures by combining AFM experiments and nonequilibrium MD (NEMD) simulations. We have measured the negative “friction–load dependence” of IL/oil mixtures at Ti interfaces. Such a negative phenomenon was also confirmed by our NEMD simulations, in which the friction force declines as the normal load increases. NEMD simulations revealed a structural reorientation of the studied IL as the normal load increases, i.e., the cation alkyl chains of ILs change the orientation to preferentially stay parallel to the tip scanning path, similar to the “blooming lotus leaf.” This reoriented IL structures produce a new sliding interface and reduce the friction force.

Chapter 1: Introduction

1.1. Solid Interfaces

The solid interfaces has been an important area for several decades due to their critical importance in determining the properties, structures, and functionalities of nanomaterials.¹⁻³ The solid interfaces can dominate the extrinsic activity, responsiveness, and stability for numerous materials, including nanocrystals, battery materials, nanoporous materials, soft matters, and supramolecular assemblies.¹ In this case, a large number of interesting phenomena have been observed at the solid interfaces, for example, wetting transparency of graphene,⁴ superlubricity between graphene nanosheets,⁵ ice nucleation on graphene oxide,⁶ vapor condensation on soft matter,⁷ water dissociation on metal surface,⁸ and ultrafast diffusion of water inside carbon nanotube.⁹ For these phenomena at the solid interfaces, they always involves multiple phases and diverse molecular components, making it a great challenge to understand the complexity of interfacial structures and the interplay of their constituents.

To probe the solid interfaces at a molecular level, a series of advanced characterization techniques, including scanning tunneling microscope (STM), atomic tunneling microscope (AFM), X-ray photoelectron spectroscopy (XPS), X-ray absorption spectroscopy (XAS), reflection-absorption infrared spectroscopy (RAIRS), Low-energy electron diffraction (LEED), nuclear magnetic resonance (NMR), and He atom scattering (HAS), have been extensively employed to probe the interfacial structures and properties of different species on solid substrates. Although the aforementioned characterization tools can provide detailed interfacial information, there still exist limitations if one only uses experimental techniques to understand the behaviors at the solid interfaces, particularly for the liquid/solid interface. For example, most experiments focus on the first adsorbed water layer (FAWL) at solid surfaces, little is known regarding the variation of

interfacial water properties when the thickness of water film changes. Therefore, it is still challenging for the experiments to obtain a complete interpretation of the interfacial behaviors. Alternatively, theoretical calculations and simulations can not only provide atomic details but also structural evolutions at the solid interfaces. Till now, multiscale computational methods, including ab initio density functional theory (DFT), ab initio molecular dynamics (AIMD), reactive molecular dynamics (RxMD), and classical molecular dynamics (MD), have been widely applied to investigate distinct processes at the solid interfaces. In this spite of this, there is still limited knowledge on the properties and structures of the first adsorbed monolayer at distinct solid interfaces. In order to answer this question, herein we choose five different systems as representatives and carry out computational studies to study the interactions between the solid surface and the first adsorbed monolayer at the interface, to understand from the electronic/atomic levels how the properties of solid surface influence the adsorption structures of the first monolayer at the solid interfaces. Those molecular level understandings can provide useful information for material design and process control.

1.2 Self-Assembled Monolayers on Metal Surfaces

Self-assembly is one of the most important processes in surface science, which can occur spontaneously without guidance from external stimuli. Self-assembled monolayers (SAMs) are the typical products of the intermolecular self-assembly that happens at gas-liquid, gas-solid, and liquid-solid interfaces. Solid surfaces, such as metal, oxide and semiconductors, can be used as template to build these supramolecular systems via the adsorption of molecules from solution phase.¹⁰⁻¹² For the generated SAMs, they are basically two-dimensional molecular structures with a thickness between 1.0 and 3.0 nm and their patterns can be tuned by changing different

substrates.¹⁰ For each molecule in the SAMs, it has three different parts: the headgroup (linking group), the backbone (main chain), and the specific terminal (active) group. The headgroup is responsible for guiding the self-assembly process at the solid surface and connecting the hydrocarbon chain to the surface via strong bonded interactions. The van der Waals and hydrophobic interactions among the hydrocarbon chains contribute to an efficient packing of the monolayer. The terminal groups can be designed with specific properties and used to anchor different molecules, biomolecules, or nanostructures by weak interaction or covalent bonds.¹¹

SAMs of thiol molecules on metal surfaces are the fundamental building blocks for creating complex structures. These SAMs can be easily prepared by employing thiols, alkyldisulfides, alkylthiosulfates, organicxanthates, and alkylthiocyanates on single-crystal or nanoparticle surface.¹⁰ It is well-accepted that the head group can form a strong thiolate-metal bond after the adsorption from the liquid phase to the metal surface. Prior studies reported that such thiolate-metal interactions play a critical role to stabilize the metal substrate and regulate the functionality of SAMs.¹³ Over the past decades, increasing research interest has been devoted to understanding the molecular nature of the metal-sulfur interface, particularly the gold-sulfur (Au-S) interface, to further promote their applications in nanoelectronics,¹⁴ biological sensings,¹⁵ molecular recognition,¹⁶ heterogeneous catalysis,¹⁷ and drug delivery,¹⁸ to just name a few.

Initially, Nuzzo and coworkers proposed that the Au-S interface is defect-free and S atoms of the thiolates are adsorbed via the three-fold hollow sites of the Au(111) surface.¹⁹ Later, it is demonstrated that the pristine Au(111) surface would undergo a reconstruction during the thiolate adsorption, to generate vacancies and adatoms of the gold substrate and promote different binding sites for S atoms.^{10, 13, 20-23} Of those defective models, the staple motif (S-Au_{ad}-S) model has been recommended, where an intermediate Au adatom is bonded with two S atoms located atop of the

Au atoms in the first layer of substrate.^{13, 23} Since the discovery of defective Au-S interface model, extensive theoretical efforts have been also developed to the understanding of adatoms and vacancies of gold substrates and how they affect the packing configuration and stability of SAMs.^{11, 21, 24-26} For example, DFT calculations of Wang and Selloni²⁴ showed that the packing structures of $c(4\times 2)$ alkanethiolate SAMs are remarkably different from the previously accepted $(\sqrt{3}\times\sqrt{3})R30^\circ$ configuration, if adatom/vacancy of the gold substrate is considered. Similarly, a large number of classical molecular dynamics (MD) simulations have been also employed to understand the behavior of SAMs.²⁷⁻³¹ However, we note that with the better understanding of defective gold substrate characteristics, a re-parameterization is necessary of force fields to better describe SAMs/Au systems. In this dissertation, we have developed a new atomistic force field model for alkanethiolate SAMs on a reconstructed Au(111) surface by using periodic ab initio density functional theory calculations.

1.3 Water models

Water is a relatively simple substance consisted of one oxygen and two hydrogen atoms, which can separately act as acceptors and donors to form hydrogen bonds (HBs) with neighboring water molecules. To reproduce the specific nature of water molecules, people have proposed many types of water models, which can be classified in terms of following three points: (a) whether the model is rigid or flexible model; (b) the number of interaction points called site; (c) whether the model consider the polarization effects. In the rigid water models, the bonded interactions are implicitly treated by using a constraint potential and thereby the water molecules only have nonbonded van der Waals and electrostatic interactions, which can be calculated by employing the

Lennard-Jones potential and Coulomb's law, respectively. In the case of flexible models, harmonic potentials are always used to describe the intramolecular stretching and bending motions.

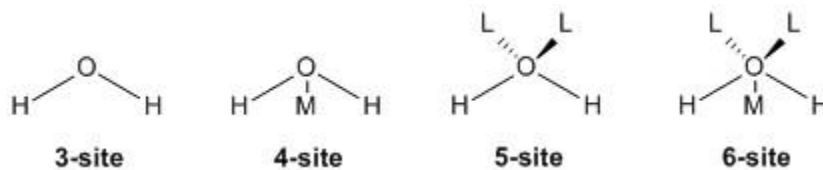


Figure 1. The general shape for different water models.

On the other hand, according to different number of interaction sites, the water models can be divided into four categories: 3- site, 4-site, 5-site, and 6-site, as shown in Figure 1. In the 3-site model, three interaction sites represent three atoms in a water molecule, with a partial charge for each site, but only the site corresponding to the oxygen atom can have the Lennard-Jones parameters to calculate the van der Waals interactions. The famous 3-site model includes SPC,³² SPC/E,³²⁻³³ and TIP3P.³⁴ It is worth noting that the TIP3P model has been reported to provide a reliable description of HB properties and vibrational spectra, but fails to quantitatively reproduce the dynamics properties of water, such as translational and rotational motions.³⁵ In the 4-site model, an additional dummy atom (labeled M in Figure 1) is added near the oxygen atom along the bisector of the HOH angle with respect to the 3-site model, and a negative charge is assigned to the dummy atom M instead of oxygen atom. Therefore, the 4-site model improves the electrostatic distribution around the water molecule. The first 4-site model is Bernal-Fowler model, proposed by Bernal and Fowler in 1933,³⁶ but it fails to provide a good prediction of the bulk properties of water, such as density and heat of vaporization. In 1983, Jorgensen and coworkers developed the TIP4P model, which has become one of the most widely-used water model in molecular simulations for biomolecular systems.³⁴ Later, people also proposed several modified TIP4P

models for specific uses: the TIP4P-Ew model,³⁷ for use with Ewald summation methods; the TIP4P/Ice,³⁸ for simulation of solid water ice; and TIP4P/2005,³⁹ a general parameterization for simulating the entire phase diagram of condensed water. When it comes to the 5-site model, there are two dummy atoms (labeled L) on the opposite side of the two hydrogen atoms, making it show a tetrahedral-like geometry. The negative charge is distributed to them, representing the lone-pair electrons of oxygen atom. A typical example of 5-site model is TIP5P developed by Mahoney and Jorgensen in 2000.⁴⁰ Compared to other models, the TIP5P has an improvement in the geometry for water dimer, the prediction of the radial distribution function, and the water density from -37.5 to 62.5 °C at 1 atm.

1.4 Water on Metal Surfaces

When water molecules are in contact with metal surfaces, their adsorption structures are determined by combined contributions of water-metal and water-water interactions. For an isolated water molecule on metal surface, the binding energy is in the range of 0.1-0.5 eV,⁴¹ comparable to that of a water in bulk ice, and the OH groups prefer the orientation parallel to the surface. With the increase of water coverage, there would form an intact water overlayer with $(\sqrt{3} \times \sqrt{3})R30^\circ$ structure on a few close-packed transition metal surfaces.⁴²⁻⁴⁴ Later, an “ice-like” bilayer structure was proposed to interpret the $(\sqrt{3} \times \sqrt{3})R30^\circ$ structure, considering a close match between their lattice parameter and the lattice spacing in ice Ih (0001).⁴³⁻⁴⁵ The bilayer model has a buckled hexagonal network. Wherein, the lower water molecules directly interact with surface metal atoms via their oxygen atoms, while the upper molecules are stabilized through the HB interactions with neighboring water molecules. In addition, on the face-centered-cubic (FCC) (110) surface, a $c(2 \times 2)$ structure was observed for the FAWL, which has distorted hexagonal network to fit the

rectangular unit cell.^{43, 46} Indeed, the adsorption structures of water on metal surfaces are very complicated because of their sensitivity to both chemical nature and geometry of solid substrates.

Over the past decades, a large number of studies have reported the behaviors of water molecules on distinct metal surfaces. The pioneering investigation on water adsorption on metal surface is H₂O/Ru(0001), due to its smallest lattice mismatch with bulk ice compared to other transition metal surfaces.^{43, 47} Previous LEED studies reported that the wetting layer on Ru(0001) adopts an “ice-like” bilayer structure with a $(\sqrt{3} \times \sqrt{3})R30^\circ$ phase.⁴⁸ Later, Held and Menzel⁴⁹ presented the first complete intensity-voltage LEED analysis of an ordered water bilayer structure adsorbed on Ru(0001) surface. In their observed $(\sqrt{3} \times \sqrt{3})R30^\circ$ structure, the vertical distance between the O atoms in the bilayer was found to be only 0.10 Å, rather than the 0.96 Å as observed in ice I_h. Besides, the DFT calculations by Feibelman⁵⁰ showed that the adsorption energy of intact water layers with coplanar O atoms lie 0.15 to 0.20 eV below the heat of sublimation of ice-I_h. Alternatively, The energetics and adsorption geometries of half-dissociated structures are in much better agreement with experiment. Analogously, King and coworkers⁵¹ found that a partially dissociated OH + H₂O overlayer is energetically favored over pure intact H₂O bilayers on the surface. Also, they further reported that the barrier of a chemisorbed H₂O monomer dissociation is 0.8 eV, whereas the barrier to dissociate a H₂O in a bilayer is only 0.5 eV. Since the discovery of mixed H₂O/OH in the wetting layer on Ru(0001) surface, great efforts from both experimental and theoretical studies have been devoted to the unique water overlayer.^{42-44, 47, 51-57} For example, Tatarkhanov *et al.*⁵³ investigated the water structures on Ru(0001) surface through a combination of STM, XAS, and DFT calculations. They found a stable partially dissociated H₂O-OH phase of water adsorbed on Ru(0001) at 180 K, and the XPS and XAS results revealed an average ratio of 3:1 for H₂O and OH. Furthermore, the STM measurements and DFT calculations results showed

that the mixed H₂O–OH phase has a honeycomb structure forming elongated stripes, with H₂O molecules preferentially lay flat and OH groups to be inside the stripes.⁵³

On the other hand, for the water molecules on Pt(111) surface, an early LEED study by Firment and Somorjai⁵⁸ demonstrated that the wetting layer on Pt(111) surface has a simple commensurate $(\sqrt{3} \times \sqrt{3})R30^\circ$ structure. However, later STM studies reported that the bilayer structure resulting from the exposure of Pt(111) to H₂O at 140 K has four different phases, only part of which exhibits the $(\sqrt{3} \times \sqrt{3})R30^\circ$ structure.⁵⁹ Also, the HAS⁶⁰ and LEED⁶¹⁻⁶² further revealed that the water overlayer on Pt(111) surface forms two highly ordered and epitaxially rotated water phase, namely $(\sqrt{37} \times \sqrt{37})R25.3^\circ$ and $(\sqrt{39} \times \sqrt{39})R16.1^\circ$. These two phases show slightly difference in their density and alignment with respect to the surface. Meanwhile, it is reported that the $(\sqrt{37} \times \sqrt{37})R25.3^\circ$ structure first forms at submonolayer coverage, and it then compresses to form the $(\sqrt{39} \times \sqrt{39})R16.1^\circ$ structure when the coverage is at saturation.⁶² In response to the experimental results, a number of theoretical studies have been performed to examine the water structures on Pt(111) surface.⁶³⁻⁶⁸ By means of ab initio molecular dynamics simulation, Meng *et al.*⁶³ investigated the adsorption structures and vibrational spectra of H-up and H-down $(\sqrt{3} \times \sqrt{3})R30^\circ$ bilayer. Their calculation results showed that the vibrational frequencies for the bilayer, either H-up or H-down case, agree well with the experimental data. However, the adsorption energy results revealed that the H-down structure (534 meV) is slightly more stable compared to the H-up one (522 meV),⁶⁴ which is in good agreement with the DFT results by Michaelides and coworkers.⁶⁵ Besides, Meng *et al.*⁶⁴ also determined the adsorption structures for the water overlayers on Pt(111) surface with $(\sqrt{37} \times \sqrt{37})R25.3^\circ$ and $(\sqrt{39} \times \sqrt{39})R16.1^\circ$ phases. They obtained an adsorption energy of 597 meV for the former and 615 meV for the latter, compared to a corresponding value of 534 meV for the $(\sqrt{3} \times \sqrt{3})R30^\circ$ phase. Such results

confirmed that the $(\sqrt{37} \times \sqrt{37})R25.3^\circ$ and $(\sqrt{39} \times \sqrt{39})R16.1^\circ$ structures are more stable than the $(\sqrt{3} \times \sqrt{3})R30^\circ$ structure. Despite great progress in this field, aforementioned studies mainly focus on the structures and properties of FAWL on the metal surface, and there is little knowledge on how the FAWL affect the behavior of other water molecules above the monolayer water. In this dissertation, we will investigate the wetting behaviors of bulk water on distinct FAWL adsorbed on the monometallic Pd(100), Au(100) surfaces, and the Pd(100)/Au(100) bimetallic junction.

1.5 Water on Metal Oxide Surfaces

For the metal oxide surfaces, the water molecules can be adsorbed chemically or physically on distinct surface active sites, including unsaturated metal sites, acid or base sites, and defect sites. This makes the water structures on oxide surfaces more complicated than those on metal surfaces. Besides, compared to the weak adsorption on metal surfaces, water molecules generally have strong interactions with oxide surfaces. As a result of this, it may result in the water dissociation on the unsaturated metal or defect sites. Furthermore, it is reported that the adsorption and/or dissociation of water molecules on some oxide surfaces can lead to surface reconstruction⁶⁹, making it a great challenge to explore the water behaviors at the interface from experiments. In this regard, different water structures, like multiple rings, one-dimensional (1D) chain, two-dimensional (2D) network, and various ice forms, have been reported from both experiments and calculations^{42, 69-72}. During the past years, using the advanced surface science techniques, including STM and atomic tunneling microscope (AFM), combined with theoretical calculations, provides us a direct image on local structures of interfacial water molecules, and thereby enables us to obtain many groundbreaking understandings in this aspect.

Among all the metal oxides, titanium dioxide (TiO_2) is one of the most widely-studied system. Understanding the behavior of water molecules at TiO_2 surfaces is of great significance to promote further progress in practical applications of TiO_2 ⁷³⁻⁷⁵. In nature, TiO_2 exists in three crystal forms: rutile, anatase, and brookite, among which the extensive studies mainly focus on the interaction of water with rutile and anatase. From the structural point of view, the topmost TiO_2 surface consists of under-coordinated titanium (Ti) and oxygen (O) sites. These sites can interact strongly with interfacial water molecules and affect significantly the adsorption structures of water molecules on TiO_2 surfaces. In the past decades, great efforts have been made to investigate the $\text{H}_2\text{O}/\text{TiO}_2$ system, from ab initio quantum mechanics calculations to force-field-based molecular dynamics simulations⁷⁶⁻⁷⁹. In the review by Sun *et al.*⁷⁶, they summarized the theoretical insights into the $\text{H}_2\text{O}/\text{TiO}_2$ interactions. Specifically, for the rutile (110) surface, an intact water structure is observed at a full monolayer coverage, whereas a mixed OH/ H_2O structure is proposed at a low water coverage (e.g., 1/8 monolayer) because of a partial dissociation⁸⁰. In the case of water molecules on rutile (100) surface, earlier experimental studies reported a molecular adsorption structure⁸¹, while recent spectroscopy results showed that a dissociated adsorption is favorable⁸². Such discrepancies also exist among the theoretical studies, probably due to the different methods and functionals employed in the calculations⁷⁶. When it comes to rutile (011) surface, the DFT calculations revealed that water molecules can dissociate to produce the $\text{Ti}_{5c}\text{-OH}$ and $\text{O}_{2c}\text{-H}$ species on this surface⁸³. On the other hand, the combined experimental and theoretical work by Beck *et al.*⁸⁴ showed that rutile (011) surface exhibits a (2×1) reconstruction with onefold coordinated (titanyl) O atoms. Later, Diebold and coworkers⁸⁵ explored the water structures on the reconstructed rutile (011) surface. They found that a mixed molecular/dissociative layer is the most stable configuration at low temperatures, whereas a fully dissociative layer appears when the

temperature goes up to 250 K. As for anatase surfaces, the studies of Vittadini and coworkers⁸⁶⁻⁸⁷ reported that the molecular adsorption is favored on the anatase (101) surface. Meanwhile, it is found that the O atom in water molecule binds to the surface Ti_{5c} atom and two H atoms form HBs with the surface bridge O atoms. However, other calculation and XPS results proposed a mixture of dissociated and molecular water in the FAWL.⁸⁸⁻⁹⁰ For anatase (001) and (100) surfaces, theoretical calculations showed that a low coverage would lead to dissociative adsorption of water molecules on the surfaces, while a mixed molecular/dissociative adsorption was only observed for (001) surface at a full coverage.⁷⁶ Despite numerous efforts in understanding of water behaviors on TiO₂ surfaces in the relatively low humidity, it is still unclear on what happens if the TiO₂ surface is in contact with bulk water. In this dissertation, we will explore the structures and dynamics of the FAWL on distinct TiO₂ surfaces when they are exposed to bulk water.

1.6 Ionic liquid

The ionic liquid generally refers to an organic molten salt with a melting point below 100° C, which is mainly composed of organic cations and inorganic or organic anions. Compared with the traditional ionic compounds, ionic liquids cannot form well-stacked crystals due to the presence of asymmetric groups in cations and/or anions. As a result of this, the melting point of ionic liquids is lower than traditional ionic compounds. In the past decades, ionic liquids have received increasing attention due to their unique properties, such as near-zero vapor pressure, high thermal conductivity and thermal stability, non-flammability, high conductivity, strong solubility, to name just a few.⁹¹⁻⁹⁴ More importantly, the physical and chemical properties of ionic liquids can be easily tailored by changing the combinations of cations and anions, which is promising in the molecular-level design and preparation of desired ILs with specific properties.⁹⁵⁻⁹⁷ With the unique properties,

ionic liquids have been extensively applied in numerous applications, currently involving catalysis,^{92, 98-101} medicine,¹⁰¹ CO₂ capture,¹⁰²⁻¹⁰⁵ cellulose treatment,¹⁰⁶⁻¹⁰⁸ supercapacitor,¹⁰⁹⁻¹¹¹ carbon nanotube dispersion,¹¹²⁻¹¹⁴ and lubricants.¹¹⁵⁻¹¹⁷

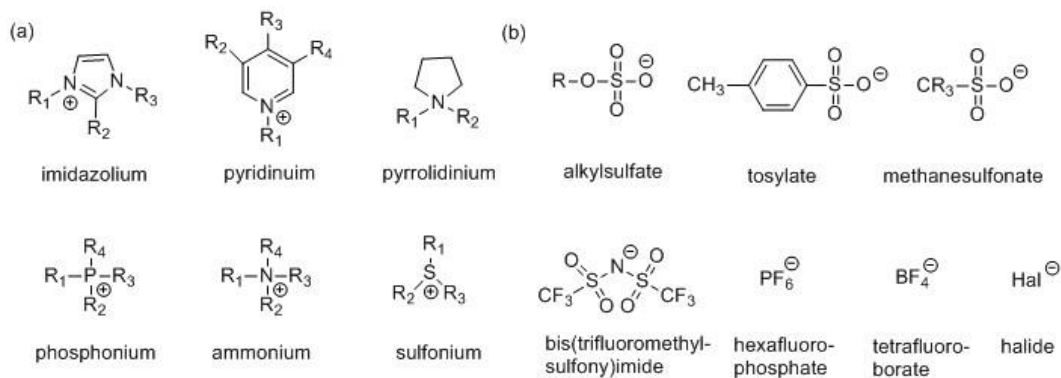


Figure 2. Chemical structures of the typical IL cations and anions. (a) **Cations:** imidazolium, pyridinium, pyrrolidinium, phosphonium, ammonium, and sulfonium, and (b) **Anions:** alkylsulfate, tosylate, methanesulfonate, bis(trifluoromethyl-sulfonyl)imide, hexafluorophosphate, tetrafluoroborate, and halide.

There are many types of ionic liquids by combining distinct cations and anions, and the structure of typical cations and anions are shown in Figure 2. It is found that the cations are organic with larger molecular volumes and the anions are inorganic with better geometric symmetry. The ionic liquid can be divided into aprotic ionic liquid and protic ionic liquid, which is determined by whether there is any transferable proton in the ionic liquid. Protic ionic liquids are formed by proton transfer between equimolar Bronsted acid and Bronsted base.¹¹⁸ Compared to aprotic ionic liquids, protic ionic liquids have a number of unique properties, such as building a three-dimensional hydrogen-bonded network like water.¹¹⁸⁻¹²⁰ In addition, the halogen-free chelated orthoborate are new novel ionic liquids containing tetraalkylphosphonium, pyrrolidinium, and imidazolium cations and stable chelated orthoborate anions, which can effectively avoid the

hydrolysis in a range of applications.¹²¹⁻¹²³ As neat lubricants, the halogen-free orthoborate-phosphonium ionic liquids considerably better antiwear and friction reducing properties under boundary lubrication conditions for steel–aluminum contacts as compared with fully formulated engine oil.¹²¹ In this dissertation, we will investigate the friction properties of some typical halogen-free orthoborate-phosphonium ionic liquids by combining AFM experiment and MD simulations.

1.7 Research Approach

Despite great progress in understanding the distinct behaviors on solid interfaces, there is still limited knowledge on the structures and properties of the first adsorbed monolayer at distinct solid interfaces. From the view of computational studies, the challenge comes from the complexity of interfacial structures and the interplay of different constituents at the solid interfaces. In this dissertation, we choose five different systems as representatives and carry out computational studies to study the interactions between the solid surface and the first adsorbed monolayer film at the interface from the electronic/atomic levels. The dissertation is organized as follows: In Chapter 2, we briefly the computational methods used in this dissertation, including DFT and classical MD calculations. We also introduce the employed computational characterizations in this chapter. Chapter 3 discusses the force field parameter development for the thiolate-gold Interface. Chapter 4 applies the classical MD simulations to investigate the wettability transition of FAWL on metal surfaces. The role of compressive lattice strain has been investigated. In Chapter 5, we perform the classical MD simulations to explore the structures and dynamics of the FAWL at distinct titanium dioxide surfaces. As discussed in Chapter 6, a combined experimental and theoretical study is carried out to study the role of interfacial potassium on the surface enhanced Raman

spectroscopy for single-crystal TiO₂ nanowhisker. In Chapter 7, the friction of ionic liquid–glycol ether mixtures is investigated by the AFM experiments and nonequilibrium MD simulations. Finally, we give a summary of the obtained results and discuss the future direction for the interfacial studies.

1.8 References

1. Marchetti, A.; Chen, J. E.; Pang, Z. F.; Li, S. H.; Ling, D. S.; Deng, F.; Kong, X. Q., Understanding Surface and Interfacial Chemistry in Functional Nanomaterials via Solid-State NNM. *Adv. Mater.* **2017**, *29* (14), 1605895.
2. Bjorneholm, O.; Hansen, M. H.; Hodgson, A.; Liu, L. M.; Limmer, D. T.; Michaelides, A.; Pedevilla, P.; Rossmeisl, J.; Shen, H.; Tocci, G.; Tyrode, E.; Walz, M. M.; Werner, J.; Bluhm, H., Water at Interfaces. *Chem. Rev.* **2016**, *116* (13), 7698.
3. Park, S.-J.; Seo, M.-K., Interface Science and Composites. Academic Press: Amsterdam; Oxford, 2011.
4. Rafiee, J.; Mi, X.; Gullapalli, H.; Thomas, A. V.; Yavari, F.; Shi, Y. F.; Ajayan, P. M.; Koratkar, N. A., Wetting Transparency of Graphene. *Nat. Mater.* **2012**, *11* (3), 217.
5. Sinclair, R. C.; Suter, J. L.; Coveney, P. V., Graphene-Graphene Interactions: Friction, Superlubricity, and Exfoliation. *Adv. Mater.* **2018**, *30* (13), 1705791.
6. Bai, G. Y.; Gao, D.; Liu, Z.; Zhou, X.; Wang, J. J., Probing the Critical Nucleus Size for Ice Formation with Graphene Oxide Nanosheets. *Nature* **2019**, *576* (7787), 437.
7. Dai, X. M.; Sun, N.; Nielsen, S. O.; Stogin, B. B.; Wang, J.; Yang, S. K.; Wong, T. S., Hydrophilic Directional Slippery Rough Surfaces for Water Harvesting. *Sci. Adv.* **2018**, *4* (3), eaq0919.

8. Donadio, D.; Ghiringhelli, L. M.; Delle Site, L., Autocatalytic and Cooperatively Stabilized Dissociation of Water on a Stepped Platinum Surface. *J. Am. Chem. Soc.* **2012**, *134* (46), 19217.
9. Joseph, S.; Aluru, N. R., Why Are Carbon Nanotubes Fast Transporters of Water? *Nano Lett.* **2008**, *8* (2), 452.
10. Vericat, C.; Vela, M. E.; Corthey, G.; Pensa, E.; Cortes, E.; Fonticelli, M. H.; Ibanez, F.; Benitez, G. E.; Carro, P.; Salvarezza, R. C., Self-Assembled Monolayers of Thiolates on Metals: A Review Article on Sulfur-Metal Chemistry and Surface Structures. *RSC Adv.* **2014**, *4* (53), 27730.
11. Vericat, C.; Vela, M. E.; Benitez, G.; Carro, P.; Salvarezza, R. C., Self-Assembled Monolayers of Thiols and Dithiols on Gold: New Challenges for a Well-Known System. *Chem. Soc. Rev.* **2010**, *39* (5), 1805.
12. Love, J. C.; Estroff, L. A.; Kriebel, J. K.; Nuzzo, R. G.; Whitesides, G. M., Self-Assembled Monolayers of Thiolates on Metals as a Form of Nanotechnology. *Chem. Rev.* **2005**, *105* (4), 1103.
13. Hakkinen, H., The Gold-Sulfur Interface at the Nanoscale. *Nat. Chem.* **2012**, *4* (6), 443.
14. Akkerman, H. B.; Blom, P. W. M.; de Leeuw, D. M.; de Boer, B., Towards Molecular Electronics with Large-Area Molecular Junctions. *Nature* **2006**, *441* (7089), 69.
15. Chaki, N. K.; Vijayamohanan, K., Self-Assembled Monolayers as a Tunable Platform for Biosensor Applications. *Biosens. Bioelectron.* **2002**, *17* (1-2), 1.
16. Love, J. C.; Estroff, L. A.; Kriebel, J. K.; Nuzzo, R. G.; Whitesides, G. M., Self-Assembled Monolayers of Thiolates on Metals as a Form of Nanotechnology. *Chem. Rev.* **2005**, *105* (4), 1103.
17. Daniel, M. C.; Astruc, D., Gold Nanoparticles: Assembly, Supramolecular Chemistry, Quantum-Size-Related Properties, and Applications toward Biology, Catalysis, and Nanotechnology. *Chem. Rev.* **2004**, *104* (1), 293.

18. Giljohann, D. A.; Seferos, D. S.; Daniel, W. L.; Massich, M. D.; Patel, P. C.; Mirkin, C. A., Gold Nanoparticles for Biology and Medicine. *Angew. Chem. Int. Edit.* **2010**, *49* (19), 3280.
19. Nuzzo, R. G.; Zegarski, B. R.; Dubois, L. H., Fundamental-Studies of the Chemisorption of Organosulfur Compounds on Au(111)-Implications for Molecular Self-Assembly on Gold Surfaces. *J. Am. Chem. Soc.* **1987**, *109* (3), 733.
20. Longo, G. S.; Bhattacharya, S. K.; Scandolo, S., A Molecular Dynamics Study of the Role of Adatoms in SAMs of Methylthiolate on Au(111): A New Force Field Parameterized from Ab Initio Calculations. *J. Phys. Chem. C* **2012**, *116* (28), 14883.
21. Cossaro, A.; Mazzarello, R.; Rousseau, R.; Casalis, L.; Verdini, A.; Kohlmeyer, A.; Floreano, L.; Scandolo, S.; Morgante, A.; Klein, M. L.; Scoles, G., X-Ray Diffraction and Computation Yield the Structure of Alkanethiols on Gold(111). *Science* **2008**, *321* (5891), 943.
22. Burgi, T., Properties of the Gold-Sulphur Interface: From Self-Assembled Monolayers to Clusters. *Nanoscale* **2015**, *7* (38), 15553.
23. Pensa, E.; Cortés, E.; Corthey, G.; Carro, P.; Vericat, C.; Fonticelli, M. H.; Benítez, G.; Rubert, A. A.; Salvarezza, R. C., The Chemistry of the Sulfur–Gold Interface: In Search of a Unified Model. *Acc. Chem. Res.* **2012**, *45* (8), 1183.
24. Wang, J. G.; Selloni, A., The C(4 X 2) Structure of Short-and Intermediate-Chain Length Alkanethiolate Monolayers on Au(111): A DFT Study. *J. Phys. Chem. C* **2007**, *111* (33), 12149.
25. Torres, E.; Biedermann, P. U.; Blumenau, A. T., The Role of Gold Adatoms in Self-Assembled Monolayers of Thiol on Au(111). *Int. J. Quantum. Chem.* **2009**, *109* (14), 3466.
26. Wang, Y.; Chi, Q. J.; Hush, N. S.; Reimers, J. R.; Zhang, J. D.; Ulstrup, J., Scanning Tunneling Microscopic Observation of Adatom-Mediated Motifs on Gold-Thiol Self-Assembled Monolayers at High Coverage. *J. Phys. Chem. C* **2009**, *113* (45), 19601.

27. Rai, B.; Sathish, P.; Malhotra, C. P.; Pradip; Ayappa, K. G., Molecular Dynamic Simulations of Self-Assembled Alkylthiolate Monolayers on an Au(111) Surface. *Langmuir* **2004**, *20* (8), 3138.
28. Devi, J. M., A Simulation Study on the Thermal and Wetting Behavior of Alkane Thiol SAM on Gold (111) Surface. *Prog. Nat. Sci.* **2014**, *24* (4), 405.
29. Xu, Z.; Song, K.; Yuan, S. L.; Liu, C. B., Microscopic Wetting of Self-Assembled Monolayers with Different Surfaces: A Combined Molecular Dynamics and Quantum Mechanics Study. *Langmuir* **2011**, *27* (14), 8611.
30. Tobias, D. J.; Mar, W.; Blasie, J. K.; Klein, M. L., Molecular Dynamics Simulations of a Protein on Hydrophobic and Hydrophilic Surfaces. *Biophys. J.* **1996**, *71* (6), 2933.
31. Hung, S. W.; Kikugawa, G.; Shiomi, J., Mechanism of Temperature Dependent Thermal Transport across the Interface between Self-Assembled Monolayer and Water. *J. Phys. Chem. C* **2016**, *120* (47), 26678.
32. Zielkiewicz, J., Structural Properties of Water: Comparison of the SPC, SPCE, TIP4P, and TIP5P Models of Water. *J. Chem. Phys.* **2005**, *123* (10), 104501.
33. Berendsen, H. J. C.; Grigera, J. R.; Straatsma, T. P., The Missing Term in Effective Pair Potentials. *J. Phys. Chem.* **1987**, *91* (24), 6269.
34. Jorgensen, W. L.; Chandrasekhar, J.; Madura, J. D.; Impey, R. W.; Klein, M. L., Comparison of Simple Potential Functions for Simulating Liquid Water. *J. Chem. Phys.* **1983**, *79* (2), 926.
35. Vega, C.; Abascal, J. L. F., Simulating Water with Rigid Non-Polarizable Models: A General Perspective. *Phys. Chem. Chem. Phys.* **2011**, *13* (44), 19663.
36. Bernal, J. D.; Fowler, R. H., A Theory of Water and Ionic Solution, with Particular Reference to Hydrogen and Hydroxyl Ions. *J. Chem. Phys.* **1933**, *1* (8), 515.

37. Horn, H. W.; Swope, W. C.; Pitner, J. W.; Madura, J. D.; Dick, T. J.; Hura, G. L.; Head-Gordon, T., Development of an Improved Four-Site Water Model for Biomolecular Simulations: TIP4P-Ew. *J. Chem. Phys.* **2004**, *120* (20), 9665.
38. Abascal, J. L. F.; Sanz, E.; Fernandez, R. G.; Vega, C., A Potential Model for the Study of Ices and Amorphous Water: TIP4P/Ice. *J. Chem. Phys.* **2005**, *122* (23), 234511.
39. Abascal, J. L. F.; Vega, C., A General Purpose Model for the Condensed Phases of Water: TIP5P/2005. *J. Chem. Phys.* **2005**, *123* (23), 234505.
40. Mahoney, M. W.; Jorgensen, W. L., A Five-Site Model for Liquid Water and the Reproduction of the Density Anomaly by Rigid, Nonpolarizable Potential Functions. *J. Chem. Phys.* **2000**, *112* (20), 8910.
41. McBride, F.; Hodgson, A., Water and Its Partially Dissociated Fragments at Metal Surfaces. *Int. Rev. Phys. Chem.* **2017**, *36* (1), 1-38.
42. Bjornhohn, E.; Hansen, M. H.; Hodgson, A.; Liu, L. M.; Limmer, D. T.; Michaelides, A.; Pedevilla, P.; Rossmeisl, J.; Shen, H.; Tocci, G.; Tyrode, E.; Walz, M. M.; Werner, J.; Bluhm, H., Water at Interfaces. *Chem. Rev.* **2016**, *116* (13), 7698.
43. Hodgson, A.; Haq, S., Water Adsorption and the Wetting of Metal Surfaces. *Surf. Sci. Rep.* **2009**, *64* (9), 381.
44. Carrasco, J.; Hodgson, A.; Michaelides, A., A Molecular Perspective of Water at Metal Interfaces. *Nat. Mater.* **2012**, *11* (8), 667.
45. Thiel, P. A.; Madey, T. E., The Interaction of Water with Solid-Surfaces: Fundamental Aspects. *Surf. Sci. Rep.* **1987**, *7* (6-8), 211.

46. Forster, M.; Raval, R.; Hodgson, A.; Carrasco, J.; Michaelides, A., C(2×2) Water-Hydroxyl Layer on Cu(110): A Wetting Layer Stabilized by Bjerrum Defects. *Phys. Rev. Lett.* **2011**, *106* (4), 046103.
47. Maier, S.; Salmeron, M., How Does Water Wet a Surface? *Acc. Chem. Res.* **2015**, *48* (10), 2783.
48. Thiel, P. A.; Hoffmann, F. M.; Weinberg, W. H., Monolayer and Multilayer Adsorption of Water on Ru(001). *J. Chem. Phys.* **1981**, *75* (11), 5556.
49. Held, G.; Menzel, D., The Structure of the P($\sqrt{3} \times \sqrt{3}$) R30-Degrees Bilayer of D₂O on Ru(001). *Surf. Sci.* **1994**, *316* (1-2), 92.
50. Feibelman, P. J., Partial Dissociation of Water on Ru(0001). *Science* **2002**, *295* (5552), 99.
51. Michaelides, A.; Alavi, A.; King, D. A., Different Surface Chemistries of Water on Ru{0001}: From Monomer Adsorption to Partially Dissociated Bilayers. *J. Am. Chem. Soc.* **2003**, *125* (9), 2746.
52. Kim, Y.; Shin, S.; Moon, E. S.; Kang, H., Spectroscopic Monitoring of the Acidity of Water Films on Ru(0001): Orientation-Specific Acidity of Adsorbed Water. *Chem-Eur J* **2014**, *20* (12), 3376.
53. Tatarkhanov, M.; Fomin, E.; Salmeron, M.; Andersson, K.; Ogasawara, H.; Pettersson, L. G. M.; Nilsson, A.; Cerda, J. I., The Structure of Mixed H₂O-Oh Monolayer Films on Ru(0001). *J. Chem. Phys.* **2008**, *129* (15), 154109.
54. Maier, S.; Lechner, B. A. J.; Somorjai, G. A.; Salmeron, M., Growth and Structure of the First Layers of Ice on Ru(0001) and Pt(111). *J. Am. Chem. Soc.* **2016**, *138* (9), 3145.

55. Messaoudi, S.; Dhouib, A.; Abderrabba, M.; Minot, C., Wetting of Intact and Partially Dissociated Water Layer on Ru(0001): A Density Functional Study. *J. Phys. Chem. C* **2011**, *115* (13), 5834.
56. Tatar khanov, M.; Ogletree, D. F.; Rose, F.; Mitsui, T.; Fomin, E.; Maier, S.; Rose, M.; Cerda, J. I.; Salmeron, M., Metal- and Hydrogen-Bonding Competition During Water Adsorption on Pd(111) and Ru(0001). *J. Am. Chem. Soc.* **2009**, *131* (51), 18425.
57. Hamada, I.; Meng, S., Water Wetting on Representative Metal Surfaces: Improved Description from Van Der Waals Density Functionals. *Chem. Phys. Lett.* **2012**, *521*, 161.
58. Firment, L. E.; Somorjai, G. A., Surface-Structures of Vapor-Grown Ice and Naphthalene Crystals Studied by Low-Energy Electron-Diffraction. *Surf. Sci.* **1976**, *55* (2), 413.
59. Morgenstern, M.; Muller, J.; Michely, T.; Comsa, G., The Ice Bilayer on Pt(111): Nucleation, Structure and Melting. *Z. Phys. Chem.* **1997**, *198*, 43.
60. Glebov, A.; Graham, A. P.; Menzel, A.; Toennies, J. P., Orientational Ordering of Two-Dimensional Ice on Pt(111). *J. Chem. Phys.* **1997**, *106* (22), 9382.
61. Haq, S.; Harnett, J.; Hodgson, A., Growth of Thin Crystalline Ice Films on Pt(111). *Surf. Sci.* **2002**, *505* (1-3), 171.
62. Harnett, J.; Haq, S.; Hodgson, A., Electron Induced Restructuring of Crystalline Ice Adsorbed on Pt(111). *Surf. Sci.* **2003**, *528* (1-3), 15.
63. Meng, S.; Xu, L. F.; Wang, E. G.; Gao, S. W., Vibrational Recognition of Hydrogen-Bonded Water Networks on a Metal Surface. *Phys. Rev. Lett.* **2002**, *89* (17), 176104.
64. Meng, S.; Wang, E. G.; Gao, S. W., Water Adsorption on Metal Surfaces: A General Picture from Density Functional Theory Studies. *Phys. Rev. B* **2004**, *69* (19), 195404.

65. Michaelides, A.; Ranea, V. A.; de Andres, P. L.; King, D. A., General Model for Water Monomer Adsorption on Close-Packed Transition and Noble Metal Surfaces. *Phys. Rev. Lett.* **2003**, *90* (21), 216102.
66. Meng, S., Dynamical Properties and the Proton Transfer Mechanism in the Wetting Water Layer on Pt(111). *Surf. Sci.* **2005**, *575* (3), 300.
67. Nie, S.; Feibelman, P. J.; Bartelt, N. C.; Thurmer, K., Pentagons and Heptagons in the First Water Layer on Pt(111). *Phys. Rev. Lett.* **2010**, *105* (2), 026102.
68. Feibelman, P. J.; Bartelt, N. C.; Nie, S.; Thurmer, K., Interpretation of High-Resolution Images of the Best-Bound Wetting Layers on Pt(111). *J. Chem. Phys.* **2010**, *133* (15), 154703.
69. Mu, R. T.; Zhao, Z. J.; Dohnalek, Z.; Gong, J. L., Structural Motifs of Water on Metal Oxide Surfaces. *Chem. Soc. Rev.* **2017**, *46* (7), 1785.
70. Sterrer, M.; Nilius, N.; Shaikhutdinov, S.; Heyde, M.; Schmidt, T.; Freund, H. J., Interaction of Water with Oxide Thin Film Model Systems. *J. Mater. Res.* **2019**, *34* (3), 360.
71. Yang, J. J.; Wang, E. G., Reaction of Water on Silica Surfaces. *Curr. Opin. Solid State Mater. Sci.* **2006**, *10* (1), 33.
72. Rimola, A.; Costa, D.; Sodupe, M.; Lambert, J. F.; Ugliengo, P., Silica Surface Features and Their Role in the Adsorption of Biomolecules: Computational Modeling and Experiments. *Chem. Rev.* **2013**, *113* (6), 4216.
73. Bai, J.; Zhou, B. X., Titanium Dioxide Nanomaterials for Sensor Applications. *Chem. Rev.* **2014**, *114* (19), 10131.
74. Kapilashrami, M.; Zhang, Y. F.; Liu, Y. S.; Hagfeldt, A.; Guo, J. H., Probing the Optical Property and Electronic Structure of TiO₂ Nanomaterials for Renewable Energy Applications. *Chem. Rev.* **2014**, *114* (19), 9662.

75. Rajh, T.; Dimitrijevic, N. M.; Bissonnette, M.; Koritarov, T.; Konda, V., Titanium Dioxide in the Service of the Biomedical Revolution. *Chem. Rev.* **2014**, *114* (19), 10177.
76. Sun, C. H.; Liu, L. M.; Selloni, A.; Lu, G. Q.; Smith, S. C., Titania-Water Interactions: A Review of Theoretical Studies. *J. Mater. Chem.* **2010**, *20* (46), 10319.
77. Raju, M.; Kim, S. Y.; van Duin, A. C. T.; Fichthorn, K. A., Reaxff Reactive Force Field Study of the Dissociation of Water on Titania Surfaces. *J. Phys. Chem. C* **2013**, *117* (20), 10558.
78. Huang, L. L.; Gubbins, K. E.; Li, L. C.; Lu, X. H., Water on Titanium Dioxide Surface: A Revisiting by Reactive Molecular Dynamics Simulations. *Langmuir* **2014**, *30* (49), 14832.
79. Kim, S. Y.; Kumar, N.; Persson, P.; Sofo, J.; van Duin, A. C. T.; Kubicki, J. D., Development of a Reaxff Reactive Force Field for Titanium Dioxide/Water Systems. *Langmuir* **2013**, *29* (25), 7838.
80. Kowalski, P. M.; Meyer, B.; Marx, D., Composition, Structure, and Stability of the Rutile $\text{TiO}_2(110)$ Surface: Oxygen Depletion, Hydroxylation, Hydrogen Migration, and Water Adsorption. *Phys. Rev. B* **2009**, *79* (11), 115410.
81. Suda, Y.; Morimoto, T., Molecularly Adsorbed H_2O on the Bare Surface of TiO_2 (Rutile). *Langmuir* **1987**, *3* (5), 786.
82. Diebold, U., The Surface Science of Titanium Dioxide. *Surf. Sci. Rep.* **2003**, *48* (5-8), 53.
83. Barnard, A. S.; Zapol, P.; Curtiss, L. A., Modeling the Morphology and Phase Stability of TiO_2 Nanocrystals in Water. *J. Chem. Theory Comput.* **2005**, *1* (1), 107.
84. Beck, T. J.; Klust, A.; Batzill, M.; Diebold, U.; Di Valentin, C.; Selloni, A., Surface Structure of $\text{TiO}_2(011)-(2 \times 1)$. *Phys. Rev. Lett.* **2004**, *93* (3), 036104.

85. Di Valentin, C.; Tilocca, A.; Selloni, A.; Beck, T. J.; Klust, A.; Batzill, M.; Losovyj, Y.; Diebold, U., Adsorption of Water on Reconstructed Rutile $\text{TiO}_2(011)-(2 \times 1)$: $\text{Ti}=\text{O}$ Double Bonds and Surface Reactivity. *J. Am. Chem. Soc.* **2005**, *127* (27), 9895.
86. Vittadini, A.; Selloni, A.; Rotzinger, F. P.; Gratzel, M., Structure and Energetics of Water Adsorbed at TiO_2 Anatase (101) and (001) Surfaces. *Phys. Rev. Lett.* **1998**, *81* (14), 2954.
87. Selloni, A.; Vittadini, A.; Gratzel, M., The Adsorption of Small Molecules on the TiO_2 Anatase(101) Surface by First-Principles Molecular Dynamics. *Surf. Sci.* **1998**, *402* (1-3), 219.
88. Patrick, C. E.; Giustino, F., Structure of a Water Monolayer on the Anatase $\text{TiO}_2(101)$ Surface. *Phys Rev Appl* **2014**, *2* (1), 014001.
89. Martinez-Casado, R.; Mallia, G.; Harrison, N. M.; Perez, R., First-Principles Study of the Water Adsorption on Anatase(101) as a Function of the Coverage. *J. Phys. Chem. C* **2018**, *122* (36), 20736.
90. Schaefer, A.; Lanzilotto, V.; Cappel, U.; Uvdal, P.; Borg, A.; Sandell, A., First Layer Water Phases on Anatase $\text{TiO}_2(101)$. *Surf. Sci.* **2018**, *674*, 25.
91. Petkovic, M.; Seddon, K. R.; Rebelo, L. P. N.; Pereira, C. S., Ionic Liquids: A Pathway to Environmental Acceptability. *Chem. Soc. Rev.* **2011**, *40* (3), 1383.
92. Hallett, J. P.; Welton, T., Room-Temperature Ionic Liquids: Solvents for Synthesis and Catalysis. 2. *Chem. Rev.* **2011**, *111* (5), 3508.
93. Maton, C.; De Vos, N.; Stevens, C. V., Ionic Liquid Thermal Stabilities: Decomposition Mechanisms and Analysis Tools. *Chem. Soc. Rev.* **2013**, *42* (13), 5963.
94. Hayes, R.; Warr, G. G.; Atkin, R., Structure and Nanostructure in Ionic Liquids. *Chem. Rev.* **2015**, *115* (13), 6357.

95. Maginn, E. J., Atomistic Simulation of the Thermodynamic and Transport Properties of Ionic Liquids. *Acc. Chem. Res.* **2007**, *40* (11), 1200.
96. Rogers, R. D., Materials Science - Reflections on Ionic Liquids. *Nature* **2007**, *447* (7147), 917.
97. Tokuda, H.; Tsuzuki, S.; Susan, M. A. B. H.; Hayamizu, K.; Watanabe, M., How Ionic Are Room-Temperature Ionic Liquids? An Indicator of the Physicochemical Properties. *J. Phys. Chem. B* **2006**, *110* (39), 19593.
98. Dupont, J.; de Souza, R. F.; Suarez, P. A. Z., Ionic Liquid (Molten Salt) Phase Organometallic Catalysis. *Chem. Rev.* **2002**, *102* (10), 3667.
99. Parvulescu, V. I.; Hardacre, C., Catalysis in Ionic Liquids. *Chem. Rev.* **2007**, *107* (6), 2615.
100. Chakraborti, A. K.; Roy, S. R., On Catalysis by Ionic Liquids. *J. Am. Chem. Soc.* **2009**, *131* (20), 6902.
101. Zakrewsky, M.; Lovejoy, K. S.; Kern, T. L.; Miller, T. E.; Le, V.; Nagy, A.; Goumas, A. M.; Iyer, R. S.; Del Sesto, R. E.; Koppisch, A. T.; Fox, D. T.; Mitragotri, S., Ionic Liquids as a Class of Materials for Transdermal Delivery and Pathogen Neutralization. *Proc. Natl. Acad. Sci. USA* **2014**, *111* (37), 13313.
102. Bara, J. E.; Camper, D. E.; Gin, D. L.; Noble, R. D., Room-Temperature Ionic Liquids and Composite Materials: Platform Technologies for CO₂ Capture. *Acc. Chem. Res.* **2010**, *43* (1), 152.
103. Bates, E. D.; Mayton, R. D.; Ntai, I.; Davis, J. H., Co₂ Capture by a Task-Specific Ionic Liquid. *J. Am. Chem. Soc.* **2002**, *124* (6), 926.
104. Zhang, J. M.; Zhang, S. J.; Dong, K.; Zhang, Y. Q.; Shen, Y. Q.; Lv, X. M., Supported Absorption of CO₂ by Tetrabutylphosphonium Amino Acid Ionic Liquids. *Chem-Eur J* **2006**, *12* (15), 4021.

105. Zhang, Y. Q.; Zhang, S. J.; Lu, X. M.; Zhou, Q.; Fan, W.; Zhang, X. P., Dual Amino-Functionalised Phosphonium Ionic Liquids for CO₂ Capture. *Chem-Eur J* **2009**, *15* (12), 3003.
106. Pinkert, A.; Marsh, K. N.; Pang, S. S.; Staiger, M. P., Ionic Liquids and Their Interaction with Cellulose. *Chem. Rev.* **2009**, *109* (12), 6712.
107. Wang, H.; Gurau, G.; Rogers, R. D., Ionic Liquid Processing of Cellulose. *Chem. Soc. Rev.* **2012**, *41* (4), 1519.
108. Swatloski, R. P.; Spear, S. K.; Holbrey, J. D.; Rogers, R. D., Dissolution of Cellulose with Ionic Liquids. *J. Am. Chem. Soc.* **2002**, *124* (18), 4974.
109. MacFarlane, D. R.; Tachikawa, N.; Forsyth, M.; Pringle, J. M.; Howlett, P. C.; Elliott, G. D.; Davis, J. H.; Watanabe, M.; Simon, P.; Angell, C. A., Energy Applications of Ionic Liquids. *Energy Environ. Sci.* **2014**, *7* (1), 232.
110. Forse, A. C.; Griffin, J. M.; Merlet, C.; Bayley, P. M.; Wang, H.; Simon, P.; Grey, C. P., Nmr Study of Ion Dynamics and Charge Storage in Ionic Liquid Supercapacitors. *J. Am. Chem. Soc.* **2015**, *137* (22), 7231.
111. Tamura, T.; Hachida, T.; Yoshida, K.; Tachikawa, N.; Dokko, K.; Watanabe, M., New Glyme-Cyclic Imide Lithium Salt Complexes as Thermally Stable Electrolytes for Lithium Batteries. *J. Power Sources* **2010**, *195* (18), 6095.
112. Chen, S.; Kobayashi, K.; Kitaura, R.; Miyata, Y.; Shinohara, H., Direct Hrtem Observation of Ultrathin Freestanding Ionic Liquid Film on Carbon Nanotube Grid. *ACS Nano* **2011**, *5* (6), 4902.
113. Fukushima, T.; Kosaka, A.; Ishimura, Y.; Yamamoto, T.; Takigawa, T.; Ishii, N.; Aida, T., Molecular Ordering of Organic Molten Salts Triggered by Single-Walled Carbon Nanotubes. *Science* **2003**, *300* (5628), 2072.

114. Fukushima, T.; Aida, T., Ionic Liquids for Soft Functional Materials with Carbon Nanotubes. *Chem-Eur J* **2007**, *13* (18), 5048.
115. Ye, C. F.; Liu, W. M.; Chen, Y. X.; Yu, L. G., Room-Temperature Ionic Liquids: A Novel Versatile Lubricant. *Chem. Commun.* **2001**, (21), 2244.
116. An, R.; Zhou, G. B.; Zhu, Y. D.; Zhu, W.; Huang, L. L.; Shah, F. U., Friction of Ionic Liquid-Glycol Ether Mixtures at Titanium Interfaces: Negative Load Dependence. *Adv. Mater. Interfaces* **2018**, *5* (14), 1800263.
117. Zhou, Y.; Qu, J., Ionic Liquids as Lubricant Additives: A Review. *ACS Appl. Mater. Interfaces* **2017**, *9* (4), 3209.
118. Greaves, T. L.; Drummond, C. J., Protic Ionic Liquids: Properties and Applications. *Chem. Rev.* **2008**, *108* (1), 206.
119. Dong, K.; Zhang, S. J., Hydrogen Bonds: A Structural Insight into Ionic Liquids. *Chem-Eur J* **2012**, *18* (10), 2748.
120. Hayes, R.; Imberti, S.; Warr, G. G.; Atkin, R., The Nature of Hydrogen Bonding in Protic Ionic Liquids. *Angew. Chem. Int. Edit.* **2013**, *52* (17), 4623.
121. Shah, F. U.; Glavatskih, S.; MacFarlane, D. R.; Somers, A.; Forsyth, M.; Antzutkin, O. N., Novel Halogen-Free Chelated Orthoborate-Phosphonium Ionic Liquids: Synthesis and Tribophysical Properties. *Phys. Chem. Chem. Phys.* **2011**, *13* (28), 12865.
122. Shah, F. U.; Glavatskih, S.; Dean, P. M.; MacFarlane, D. R.; Forsyth, M.; Antzutkin, O. N., Halogen-Free Chelated Orthoborate Ionic Liquids and Organic Ionic Plastic Crystals. *J. Mater. Chem.* **2012**, *22* (14), 6928.

123. Chiappe, C.; Signori, F.; Valentini, G.; Marchetti, L.; Pomelli, C. S.; Bellina, F., Novel (Glycerol)Borate-Based Ionic Liquids: An Experimental and Theoretical Study. *J. Phys. Chem. B* **2010**, *114* (15), 5082.

Chapter 2: Computational Methods

2.1 Density Functional Theory

Density functional theory (DFT) is primarily a theory of electronic ground state structure, in terms of the electronic density distribution $n(r)$. Since its birth, it has become increasingly useful for the understanding and calculation of the ground state density and energy of molecules, clusters, and solids. In the DFT scheme, it is assumed that the electrons do not interact with one another. The electron density then is written as a simple sum over a set of squares of (or occupied) noninteracting orbitals ϕ_i :¹

$$\rho(r) = \sum_i |\phi_i(r)|^2 = 2 \sum_i^{occ} |\phi_i(r)|^2 \quad (2 - 1)$$

where r represents a particular point in the real space and ϕ_i refers to the orbital i at position r . In the above equation, the usual wave functions, Ψ_i , are replaced by orbitals ϕ_i . In addition, the amplitudes of each orbital are converted to a positive density of electrons $\rho(r)$. After adding up all the electron densities over the whole space, we can obtain the total number of electrons n .

In the following section, we will provide a brief introduction to some principles related to the DFT mythology, including Born-Oppenheimer approximation, Hohenberg-Kohn theorem, Kohn-Sham formalism, and exchange-correlation energy. Besides, we also give some discussions on the application and limitation of DFT method. A complete understanding of the origin and evolution of DFT can be found in other books²⁻⁴ or review papers.⁵⁻⁸

2.1.1 Born-Oppenheimer approximation

For any molecule, the Hamiltonian can be written as (*defining* $r_{\alpha\beta} = |r_\alpha - r_\beta|$):

$$\hat{H} = -\frac{1}{2} \sum_I^{nuclei} \frac{1}{M_I} \nabla_I^2 - \frac{1}{2} \sum_i^{electron} \nabla_i^2 + \frac{1}{2} \sum_{IJ}^{nuclei} \frac{Z_I Z_J}{R_{IJ}} + \frac{1}{2} \sum_{ij}^{electron} \frac{1}{r_{ij}} - \sum_{I,i} \frac{Z_I}{|r_i - R_I|} \quad (2 - 2)$$

where the five terms correspond to nuclear kinetic energy, electronic kinetic energy, nuclear-nuclear repulsion, electron-electron repulsion, and electron-nuclear attraction, respectively. The physical motivation behind the Born-Oppenheimer approximation is that the nuclei are much heavier than the electrons, so that the electrons respond almost instantaneously to the changes of nuclei positions, and thus the kinetic energy of nuclei can be ignored. This is known as Born-Oppenheimer approximation and it shows a high accuracy in calculating the band structure of crystals, the nuclear vibration model of solids, and the electrical transport for metals.³⁻⁴

Based on the Born-Oppenheimer approximation, the many-body Hamiltonian then can be expressed as:

$$\hat{H} = \hat{T} + \hat{V}_{ext} + \hat{V}_{int} + E_{II} \quad (2 - 3)$$

where

$$\hat{T} = \sum_i -\frac{1}{2} \nabla_i^2, \text{ the kinetic energy operator of the electrons;}$$

$$\hat{V}_{ext} = \sum_{i,I} V_I(|r_i - R_I|), \text{ the potential acting on the electrons due to the nuclei;}$$

$$\hat{V}_{int} = \frac{1}{2} \sum_{i \neq j} \frac{1}{|r_i - r_j|}, \text{ the potential energy operator of the electron - electron interactions;}$$

E_{II} , the potential energy operator of the nuclei interactions, including the contributions from the external fields. The Hamiltonian can be used to determine the ground state and its energy can be obtained by solving the eigenvalue equation $H\Psi_0 = E_0\Psi_0$.

2.1.2 Hohenberg-Kohn Theorem

The concept of DFT was first developed in the early 20th century based on the Thomas-Fermi model, introducing the idea of expressing the energy of a system as a function of the total electron density.⁹ However, it was subject to formal verification until Hohenberg-Kohn finally proved it with two theorems,¹⁰ which completed the links between electron density, external energy, Hamiltonian, and wave function. The first Hohenberg-Kohn theorem demonstrates that the ground state of a many-electron system are uniquely determined by an electron density that depends on only three spatial coordinates¹. The second Hohenberg-Kohn theorem identified a way to find the minimum energy of a system and proved that the ground state of a system could be searched by using the variational principle. At a given external potential, if we minimize the system energy as much as we can with varying electron density, then we will reach the very bottom of the energy well, yet not below it. This is called the variational principle in the framework of DFT, and the electron density that minimizes the system energy is the ground-state electron density¹. Although the Hohenberg-Kohn theorem is the core part of DFT, but it does not provide the exact form of the density functional.

2.1.3. Kohn-Sham Method

The Hohenberg-Kohn theorem gives a theoretical guideline of searching the ground energy state by minimizing energy in terms of the electron density. However, it fails to produce the kinetic energy with a satisfactory level of accuracy, albeit it is quite easy to calculate the kinetic energy from the wave function. In this case, Kohn and Sham proposed an ingenious method in 1965, of combining the electron density and the wave functions.¹¹ They used a non-interacting reference system and repartitioned the total energy functional into the following form:

$$E[\rho] = T_0[\rho] + \int [\hat{V}_{ext}(r) + \hat{V}_{int}(r)]\rho(r)dr + E_{XC}[\rho] \quad (2 - 4)$$

where $T_0[\rho]$ corresponds to the kinetic energy of the electrons of the non-interacting reference system, which has the same electron density ρ as the real system. The non-interacting term means that there is no electron-electron interaction, but the electrons interact with the nuclei. The $\hat{V}_{ext}(r)$ refers to the external potential from the nuclei, defined as:

$$\hat{V}_{ext}(r) = \sum_I \frac{-Z_I}{|R_I - r|} \quad (2 - 5)$$

$\hat{V}_{int}(r)$ means the electrostatic interaction among the electrons. It includes the electron self-interaction explicitly and represents the interaction of ρ with itself. $\hat{V}_{int}(r)$ can be expressed as:

$$\hat{V}_{int}(r) = \int \frac{\rho(r' - r)}{|r' - r|} dr' \quad (2 - 6)$$

The last term $E_{XC}[\rho]$ represents the exchange-correlation energy. It includes all the energy contributions that have not been accounted for by the previous three terms:

- (1) The electron exchange;
- (2) The electron correlation;
- (3) A portion of the kinetic energy which is necessary to correct $T_0[\rho]$ to obtain the kinetic energy of the real system $T_e[\rho]$;

The philosophy is to put the energy contributions, which are not easy to calculate, into the $E_{XC}[\rho]$ functional, and then construct a reliable and reasonable approximation for $E_{XC}[\rho]$. However, it is still the biggest challenge in DFT up to now.

2.1.4. Exchange-Correlation Functional

The exchange-correlation functional $E_{XC}[\rho]$ is generally comprised of two individual parts: the exchange part $E_X[\rho]$ and the correlation part $E_C[\rho]$, although the legitimacy of such separation has been the subject of doubts.

$$E_{XC}[\rho] = E_X[\rho] + E_C[\rho] \quad (2 - 7)$$

Basically, the exchange part is related to the interactions between the electrons with the same spin, and the correlation part represents the interactions for those electrons with opposite spins. Both exchange and correlation parts can have two different types: the local functional and the gradient corrected functional. The former depends on the electron density $\rho(r)$ at a local position r , and the latter is dependent on both the electron density $\rho(r)$ and its gradient $\Delta\rho$. A specific and detailed discussion on the exchange-correlation functionals can be found from other publications.¹²⁻¹⁵

2.1.5. Application and Limitation of DFT

Nowadays DFT has become one of the most popular calculation tools in fundamental science and engineering processes. It has been widely used for numerous systems, including the biomolecules,¹⁶⁻¹⁸ polymers,¹⁹⁻²¹ transition metal complexes,²²⁻²³ metals,²⁴⁻²⁷ metal oxides,²⁷⁻²⁹ zeolites,³⁰⁻³¹ graphene,³² to name just a few. Also, DFT is powerful to analyze different types of properties for these systems, such as the calculation of vibrational spectra,³³⁻³⁴ scanning tunneling microscopy,³⁵⁻³⁶ and nuclear magnetic resonance,³⁷⁻³⁸ and the study of chemical reactions, including activation energy barrier, reaction mechanism, and reaction kinetics.³⁹⁻⁴¹ Moreover, DFT method can be employed to develop the force field parameters for both reactive molecular dynamics⁴²⁻⁴³ and classical molecular dynamics⁴⁴⁻⁴⁵ simulations. Despite the great popularity and success, the DFT method still has some limitations:

- (a) The underestimation of the chemical reaction barriers, the band gaps of materials, the dissociating energies of molecular ions, and the charge transfer excitation energies;
- (b) The overestimation of the binding energies of charge transfer complexes, the cohesive energies, bulk moduli;
- (c) The difficulty in describing strongly correlated systems, degenerate and near-degenerate states;
- (d) The poor treatment of long-range noncovalent interactions;

More discussions about the limitations and challenges of DFT method can be found in other review papers.⁴⁶⁻⁴⁸

2.2 Molecular Dynamics Simulation

Molecular dynamics (MD) is a computer simulation method used to analyze the physical movements of atoms and molecules. In molecular dynamics, successive configuration of the system are generated by integrating Newton's laws of motion. The result is a trajectory that specifies how the positions and velocities of the particles in the system vary with time. Based on the generated coordinates, we can then use the statistical analysis to calculate the numerous properties, including heat capacity, thermal conductivity, thermal expansion coefficient, melting point, phase diagram, free energy, radial distribution function, diffusion coefficient, hydrogen bond, vibrational spectra, etc. The accuracy of the simulation is significantly dependent on the force field parameters. Currently, the most widely used classic force fields include AMBER,⁴⁹ CHARMM,⁵⁰ GROMAS,⁵¹ COMPASS,⁵² OPLS,⁵³ MM2,⁵⁴ UFF,⁵⁵ DREIDING,⁵⁶ and TraPPE.⁵⁷

Force field is a functional form used to calculate the potential energy of a system in MD simulations. When two atoms are close to each other, they will start to feel the attraction and

repulsion interactions and finally settle down at the equilibrium position where the force is equal to zero for two atoms. The sum of all forces acting on an atom, \mathbf{F} , is

$$\mathbf{F} = m\mathbf{a} = m \frac{d\mathbf{v}}{dt} = m \frac{d^2\mathbf{r}}{dt^2} = \frac{d\mathbf{p}}{dt} \quad (2 - 8)$$

where \mathbf{a} is the acceleration, \mathbf{v} is the velocity, t is the time, \mathbf{r} is the position, and \mathbf{p} is the momentum. The force field potential for specific systems can be obtained by fitting certain functions with the experimental or calculated data. The experimental data used for fitting includes the lattice parameter, bulk modulus, thermal expansion coefficient, vibrational spectra, dielectric constants, and surface energy.¹ Over the past decades, great progress has been obtained in developing accurate and reliable potentials for distinct systems. In the following, we will give a brief discussion of five popular potentials

2.2.1 Pair potentials

For a simulation system with a number of N atoms, the potential energy of an atom i interacts with all the other atoms at a certain time can be expressed as:

$$U = \sum_{i < j}^N U_2(r_i, r_j) + \sum_{i < j < k}^N U_3(r_i, r_j, r_k) + \dots \quad (2 - 9)$$

where the first two terms represent the potential for two atoms and three atoms. Here, we only consider the two-atom pair interactions. The pair potentials are the simplest ones that consider only two-atom interactions and ignore all other interactions. The most popular pair potential is the L-J potential $U_{LJ}(r)$, which is expressed as:

$$U_{LJ}(r) = 4\varepsilon \left[\left(\frac{\sigma}{r} \right)^{12} - \left(\frac{\sigma}{r} \right)^6 \right] \quad (2 - 10)$$

where parameter ε is the well depth and σ is the interatomic distance at which the potential is zero. The r^{-12} term, which is the repulsive term, describes Pauli repulsion at short ranges due to

overlapping electron orbitals, and the r^{-6} term, which is the attractive long-range term, describes attraction at long ranges.

2.2.2 Embedded atom method potentials

In metal and transition metals, the atoms are typically coordinated with 8-12 neighboring atoms and thereby surrounded by the electron cloud. Significant efforts have been devoted to including the many-atom effects within the framework of empirical potentials. The embedded atom method (EAM) considers the effective electron density at a given atomic sites as one of the parameters, thereby capturing some electronic effects while keeping the simplicity of a potential.⁵⁸ The EAM includes the contributions from both pair potential and embedding energy, and therefore its functional form has two parts: one part for the pair interaction and the other part for the embedding energy as a function of electron density at atom i :

$$U_{EAM} = \sum_{i<j} U_{ij}(r_{ij}) + \sum_{i<j} F_i(\rho_i) \quad (2 - 11)$$

where $F_i(\rho_i)$ is the embedding energy function; r_{ij} is the scalar distance between atoms i and j , which corresponds to the atom-atom distance in three dimensions. The first term has the following expression:

$$\sum_{i<j} U_{ij}(r_{ij}) = U_{12} + U_{13} + \cdots + U_{23} + U_{24} + \cdots + U_{34} + U_{35} + \cdots \quad (2 - 12)$$

The electron density at site i is simply the linear superposition of valence-electron clouds from all other atoms:

$$\rho_i = \frac{1}{2} \sum_{j(\neq i)} \rho_j(r_{ij}) \quad (2 - 13)$$

Since the electron density is a summation over many atoms, usually limited by a cutoff radius, the EAM potential is a many-body potential. For a single element system of atoms, three scalar functions must be specified: the embedding function, a pair-wise interaction, and an electron cloud contribution function.⁵⁸

2.2.3 Buckingham potential

The Buckingham potential, proposed by Richard Buckingham in 1938,⁵⁹ is a formula used to describe the Pauli exclusion principle and van der Waals energy for interaction of two atoms. It has the following functional form:

$$E(r_{ij}) = A \exp(-Br_{ij}) - \frac{C}{r_{ij}^6} \quad (2-14)$$

where A, B, and C are constant, r_{ij} is the distance between atoms i and j . The first derivatives for the two terms on the right is negative and positive, respectively, and therefore the first term represents the repulsion interaction, while the second term describes the attraction interaction. One thing should be noted is that, when the distance r is close to zero, the first exponential term would converge to a constant, while the r^{-6} term diverges. This would lead to the Buckingham potential show attractive interactions, and therefore it may be problematic when dealing with a structure with very short interatomic distances

2.2.4 Reactive force field potentials

For the aforementioned classical potentials, they can only describe the physical interactions between different species, but do not allow the bond breaking or forming, making them fail to describe the chemical reactions. In 2001, van Duin *et al.* proposed a reactive force field (ReaxFF),⁴² based on a bond order concept initially proposed by Tersoff,⁶⁰ to describe the stability

and geometry of hydrocarbon system. In the ReaxFF, the bond order BO'_{ij} for a pair of atoms can be calculated from the interatomic distance r_{ij} , defined as:

$$\begin{aligned}
 BO'_{ij} &= BO'_{ij}{}^{\sigma} + BO'_{ij}{}^{\pi} + BO'_{ij}{}^{\pi\pi} \\
 &= \exp \left[p_{bo1} \cdot \left(\frac{r_{ij}}{r_0^{\sigma}} \right)^{p_{bo2}} \right] + \exp \left[p_{bo3} \cdot \left(\frac{r_{ij}}{r_0^{\pi}} \right)^{p_{bo4}} \right] + \exp \left[p_{bo5} \cdot \left(\frac{r_{ij}}{r_0^{\pi\pi}} \right)^{p_{bo6}} \right] \quad (2-15)
 \end{aligned}$$

where the six bond order parameters in above equation have been divided into three groups, namely, (p_{bo1}, p_{bo2}) , (p_{bo3}, p_{bo4}) , $(p_{bo5}$ and $p_{bo6})$, to describe the σ , π and $\pi\pi$ bonds, respectively. Eq. (2-17) is defined so that the value of the three exponentials is unity below a threshold interatomic distance and zero at longer distances.

Since the emerge of the ReaxFF, tremendous efforts have been devoted to developing a large number of force field parameters for different systems. To date, ReaxFF parameter sets have been developed for more than 40 elements of the periodic table and have been successfully employed to describe numerous complex process, such as the growth the carbon nanotube on nickel-based catalyst,⁶¹ the removal of toxic gases with graphene oxide,⁶² the exploration of the thermal stability of metal organic framework,⁶³ the prediction of surface reactivity for water dissociation,⁶⁴ and the oxidation of butane over a pyrite-covered Cr_2O_3 catalyst,⁶⁵ and abundant liquid/solid interface systems, including $\text{H}_2\text{O}/\text{TiO}_2$ ^{64, 66}, $\text{H}_2\text{O}/\text{ZnO}$ ⁶⁷, $\text{H}_2\text{O}/\text{SiO}_2$ ⁶⁸, $\text{H}_2\text{O}/\text{Si}$ ⁶⁹, $\text{H}_2\text{O}/\text{Ni}$ ⁷⁰, and $\text{H}_2\text{O}/\text{Cu}$ ⁷¹, to just name a few. Yet we point out that development of ReaxFF is nontrivial, due to the large number of parameters implemented in the concept and formulations of ReaxFF. For non-reacting systems of water on solid surfaces, classical MD simulations provide equivalent accuracy of predictions and similar level of insights of diffusion, wetting, and ice nucleation. of water on solid surfaces.

2.3 Computational Characterizations

2.3.1 Contact angle calculation

The contact angle of formed water droplet was calculated with the method reported in previous studies.⁷²⁻⁷⁴ The algorithm is listed below, with illustrations shown in Figure 3:

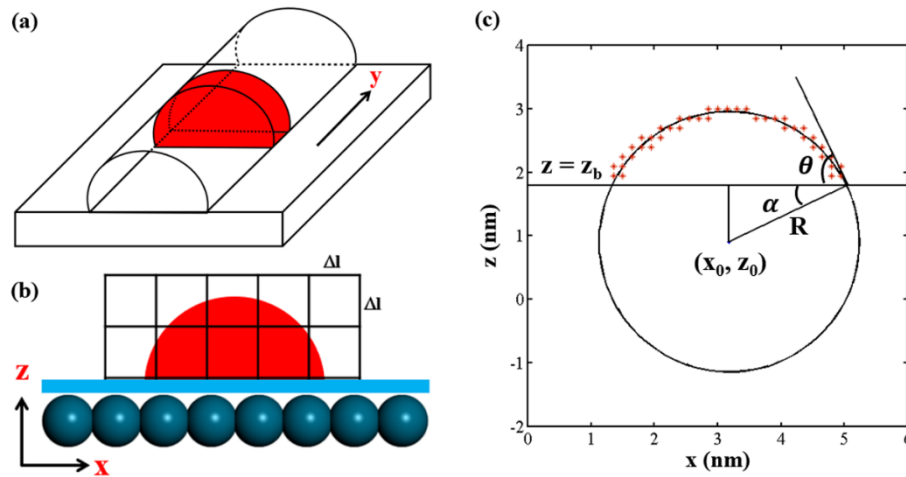


Figure 3. Schematic illustration for (a) cylindrical bin by dividing the water droplet, (b) volume element by dividing the cylindrical bin shown in (a) and (c) fitting of the air-water interface and the contact angle calculation.

(a) The cylindrical water droplet is divided into a number of bins with a thickness of 0.15 nm along the y direction.

(b) Each bin is further divided into identical volumetric elements with a dimension of 0.15 nm in both x and z directions. Then, the water density of each volumetric element is calculated. It should be mentioned that the coordinates of O atoms are employed to determine the position distribution of water molecules.

(c) The air-water interface is approximated where the water density in the volume element is about half of bulk water. Those corresponding volumetric elements are then extracted and labeled.

(d) A MATLAB script is prepared to fit the positions of the air-water interface to a circle equation

by the method of least squares where the regression equation is denoted as $(x-x_0)^2 + (z-z_0)^2 = R^2$.

The obtained parameters in the regression equation is further applied to calculate the contact angle by the following equation:

$$\theta = 90^\circ - \arcsin\left(\frac{z_b - z_0}{R}\right) \quad (2-16)$$

where R is the radius of the fitted circle, and z_b is the lowest position of water droplet in z direction.

2.3.2 Hydrogen bond calculation

The hydrogen bond (HB) interactions are very important for the structures, properties, and stability of the water molecules at the solid interface. Herein, the HB of water molecule is calculated based on the following geometry criteria:⁷⁵⁻⁷⁷

$$R^{OO} < R_c^{OO} \quad \text{and} \quad \theta^{OOH} < \theta_c^{OOH} \quad (2-17)$$

where R^{OO} is the distance between two O atoms, one of which serves as the HB acceptor and the other is HB donor; θ^{OOH} represents the angle of the two water molecules, O...O-H. Similarly, R_c^{OO} and θ_c^{OOH} represent the critical upper limit to the distance and angle of hydrogen bonded water molecules. The two thresholds are 3.5 Å and 30°, respectively. In addition, the HB strength was calculated by the continuous time correlation functions (TCFs), $S_{HB}(t)$:⁷⁵⁻⁷⁶

$$S_{HB}(t) = \frac{\langle h(0)h(t) \rangle}{\langle h(t) \rangle} \quad (2-18)$$

where the population variable of $h(t)$ is unity when a tagged HB pair could maintain for a time period from 0 to t, otherwise, $h(t)$ is zero.

2.3.3 Reorientation rate calculation

The dynamical stability of the adsorbed monolayer water on solid surface can be characterized by the reorientation dynamics of water molecules, as proposed by Zeng and co-workers.⁷⁸ Here, the

water reorientation dynamics was calculated by employing the second-order Legendre polynomial time-correlation function defined as:

$$c_2(t) = \langle P_2[\vec{u}(0) \cdot \vec{u}(t)] \rangle \quad (2 - 19)$$

where $\vec{u}(0)$ and $\vec{u}(t)$ correspond to the dipole moment of water molecule at time 0 and t, respectively. The second-order Legendre polynomial is expressed as $P_2(x) = \frac{1}{2}(3x^2 - 1)$ and $\langle \dots \rangle$ represents the ensemble average over time. The calculated reorientation rate $c_2(t)$ generally exhibits an exponential decay from 1 to 0 within a certain time t.

2.3.4 Free energy profile calculation for FAWL

As discussed in the reference, the free energy profiles can be obtained by calculating the normalized probability:⁷⁹⁻⁸¹

$$P(X) = \frac{1}{Z} \exp[-\beta G(X)] \quad (2 - 20)$$

where (X) is any set of coordinates, P(X) is the probability at ⁸², $\beta = \frac{1}{k_B T}$ where k_B is the Boltzmann's constant, and Z is equipartition function. The relative free energy can then be easily expressed as:

$$G(x_2, y_2) - G(x_1, y_1) = -k_B T \ln \left[\frac{P(x_2, y_2)}{P(x_1, y_1)} \right] \quad (2 - 21)$$

$$\Delta G((x_2, y_2) \rightarrow (x_1, y_1)) = -k_B T \ln \left[\frac{P(x_2, y_2)}{P(x_1, y_1)} \right] \quad (2 - 22)$$

where $\Delta G((x_2, y_2) \rightarrow (x_1, y_1))$ is the relative free energy at position (x₂, y₂) with respect to that at position (x₁, y₁). Therefore, in our free energy calculations, the reference state is the position where the probability $P(x_1, y_1)$ is 1, and thereby the relative free energy can be denoted as:

$$\Delta G(x, y) = -k_B T \ln P(x, y) \quad (2-23)$$

Since the distribution probability $P(x, y)$ of each water molecule in the first adsorbed water layer is smaller than 1.0, the calculated $\Delta G(x, y)$ is a positive value. The smaller the distribution probability is, the larger the free energy difference would be. A larger $\Delta G(x, y)$ value means that the distribution probability at position (x, y) is smaller, indicating that water molecules are less stable to reside there.

2.3.5 Structural order parameter analysis

The arrangement of water molecules can be probed via the tetrahedral order parameter (q) by Errington and Debenedetti:⁸³

$$q_i = 1 - \frac{3}{8} \sum_{j=1}^3 \sum_{k=j+1}^4 \left(\cos \theta_{ijk} + \frac{1}{3} \right) \quad (2 - 24)$$

where the summation is over four nearest neighbors of any water molecule i ; θ_{ijk} is the angle formed by two vectors pointing from the reference molecule i to its two nearest neighboring molecules, j and k . The calculated value of q_i varies from 0 (a random distribution) to 1 (a perfect tetrahedral network). Such order parameter has been employed to investigate structural pattern and nucleation of water at liquid/solid interfaces

2.4 Reference

1. Lee, J. G., *Computational Materials Science : An Introduction*. CRC press, London, 2012.
2. Parr, R. G.; Yang, W., *Density-Functional Theory of Atoms and Molecules*. Oxford University Press, New York, 1989.
3. Szabo, A.; Ostlund, N. S., *Modern Quantum Chemistry*. McGraw-Hill, New York, 1989.
4. Grosso, G.; Pastori Parravicini, G., *Solid State Physics*. Academic Press, San Diego, 2000.

5. Jones, R. O.; Gunnarsson, O., The Density Functional Formalism, Its Applications and Prospects. *Rev Mod Phys* **1989**, *61* (3), 689.
6. Kohn, W.; Becke, A. D.; Parr, R. G., Density Functional Theory of Electronic Structure. *J. Phys. Chem.* **1996**, *100* (31), 12974.
7. Argaman, N.; Makov, G., Density Functional Theory: An Introduction. *Am. J. Phys.* **2000**, *68* (1), 69.
8. Burke, K., Perspective on Density Functional Theory. *J. Chem. Phys.* **2012**, *136* (15), 150901.
9. Teller, E., On Stability of Molecules in Thomas-Fermi Theory. *Rev. Mod. Phys.* **1962**, *34* (4), 627.
10. Hohenberg, P.; Kohn, W., Inhomogeneous Electron Gas. *Phys. Rev. B* **1964**, *136* (3b), B864.
11. Kohn, W.; Sham, L. J., Self-Consistent Equations Including Exchange and Correlation Effects. *Phys. Rev.* **1965**, *140* (4a), 1133.
12. Gunnarsson, O.; Lundqvist, B. I., Exchange and Correlation in Atoms, Molecules, and Solids by Spin-Density Functional Formalism. *Phys. Rev. B* **1976**, *13* (10), 4274.
13. Ziegler, T., Approximate Density Functional Theory as a Practical Tool in Molecular Energetics and Dynamics. *Chem. Rev.* **1991**, *91* (5), 651.
14. Bauschlicher, C. W., A Comparison of the Accuracy of Different Functionals. *Chem. Phys. Lett.* **1995**, *246* (1-2), 40.
15. Becke, A. D., Density-Functional Exchange-Energy Approximation with Correct Asymptotic-Behavior. *Phys. Rev. A* **1988**, *38* (6), 3098.
16. Siegbahn, P. E. M.; Blomberg, M. R. A., Density Functional Theory of Biologically Relevant Metal Centers. *Annu. Rev. Phys. Chem.* **1999**, *50*, 221.

17. Kaschner, R.; Hohl, D., Density Functional Theory and Biomolecules: A Study of Glycine, Alanine, and Their Oligopeptides. *J. Phys. Chem. A* **1998**, *102* (26), 5111.
18. Ban, F. Q.; Rankin, K. N.; Gauld, J. W.; Boyd, R. J., Recent Applications of Density Functional Theory Calculations to Biomolecules. *Theor. Chem. Acc.* **2002**, *108* (1), 1-11.
19. Suhai, S., Density-Functional Studies of the Hydrogen-Bonded Network in an Infinite Water Polymer. *J. Phys. Chem.* **1995**, *99* (4), 1172.
20. Gierschner, J.; Cornil, J.; Egelhaaf, H. J., Optical Bandgaps of Pi-Conjugated Organic Materials at the Polymer Limit: Experiment and Theory. *Adv. Mater.* **2007**, *19* (2), 173.
21. Xu, X. F.; Cao, D. P.; Wu, J. Z., Density Functional Theory for Predicting Polymeric Forces against Surface Fouling. *Soft Matter* **2010**, *6* (19), 4631.
22. Buhl, M.; Kabrede, H., Geometries of Transition-Metal Complexes from Density-Functional Theory. *J. Chem. Theory Comput.* **2006**, *2* (5), 1282.
23. Vlcek, A.; Zalis, S., Modeling of Charge-Transfer Transitions and Excited States in D(6) Transition Metal Complexes by Dft Techniques. *Coord. Chem. Rev.* **2007**, *251* (3-4), 258.
24. Cramer, C. J.; Truhlar, D. G., Density Functional Theory for Transition Metals and Transition Metal Chemistry. *Phys. Chem. Chem. Phys.* **2009**, *11* (46), 10757.
25. Aarons, J.; Sarwar, M.; Thompsett, D.; Skylaris, C. K., Perspective: Methods for Large-Scale Density Functional Calculations on Metallic Systems. *J. Chem. Phys.* **2016**, *145* (22), 220901.
26. Quintal, M. M.; Karton, A.; Iron, M. A.; Boese, A. D.; Martin, J. M. L., Benchmark Study of Dft Functionals for Late-Transition-Metal Reactions. *J. Phys. Chem. A* **2006**, *110* (2), 709.
27. Fernando, A.; Dimuthu, K. L.; Weerawardene, M.; Karimova, N. V.; Aikens, C. M., Quantum Mechanical Studies of Large Metal, Metal Oxide, and Metal Chalcogenide Nanoparticles and Clusters. *Chem. Rev.* **2015**, *115* (12), 6112.

28. Gronbeck, H., First Principles Studies of Metal-Oxide Surfaces. *Top. Catal.* **2004**, 28 (1-4), 59.
29. Diebold, U.; Li, S. C.; Schmid, M., Oxide Surface Science. *Annu. Rev. Phys. Chem.* **2010**, 61, 129.
30. Nicholas, J. B., Density Functional Theory Studies of Zeolite Structure, Acidity, and Reactivity. *Top. Catal.* **1997**, 4 (1-2), 157.
31. Astala, R.; Auerbach, S. M.; Monson, P. A., Density Functional Theory Study of Silica Zeolite Structures: Stabilities and Mechanical Properties of Sod, Lta, Cha, Mor, and Mfi. *J. Phys. Chem. B* **2004**, 108 (26), 9208.
32. Polini, M.; Tomadin, A.; Asgari, R.; MacDonald, A. H., Density Functional Theory of Graphene Sheets. *Phys. Rev. B* **2008**, 78 (11), 115426.
33. Petrenko, T.; Ray, K.; Wieghardt, K. E.; Neese, F., Vibrational Markers for the Open-Shell Character of Transition Metal Bis-Dithiolenes: An Infrared, Resonance Raman, and Quantum Chemical Study. *J. Am. Chem. Soc.* **2006**, 128 (13), 4422.
34. Shanmugasundaram, M.; Puranik, M., Computational Prediction of Vibrational Spectra of Normal and Modified DNA Nucleobases. *J. Raman Spectrosc.* **2009**, 40 (12), 1726.
35. Bocquet, M. L.; Wang, B., Metal-Organic Interaction Probed by First Principles STM Simulations. *Prog. Surf. Sci.* **2010**, 85 (9-12), 435.
36. Zhang, W. H.; Li, Z. Y.; Wang, B.; Yang, J. L., Scanning Tunneling Microscopy and Density Functional Theory Combined Studies of Rutile TiO₂(110) Surface Chemistry: Watch Surface Processes at the Atomic Scale. *Int. J. Quantum. Chem.* **2013**, 113 (2), 89.
37. Bagno, A.; Rastrelli, F.; Saielli, G., Predicting C-13 NMR Spectra by DFT Calculations. *J. Phys. Chem. A* **2003**, 107 (46), 9964.

38. Laskowski, R.; Blaha, P.; Tran, F., Assessment of DFT Functionals with NMR Chemical Shifts. *Phys. Rev. B* **2013**, *87* (19), 195130.
39. Norskov, J. K.; Abild-Pedersen, F.; Studt, F.; Bligaard, T., Density Functional Theory in Surface Chemistry and Catalysis. *Proc. Natl. Acad. Sci. USA* **2011**, *108* (3), 937.
40. Santiso, E. E.; Gubbins, K. E., Multi-Scale Molecular Modeling of Chemical Reactivity. *Mol. Simul.* **2004**, *30* (11-12), 699.
41. Gong, J. L.; Mullins, C. B., Surface Science Investigations of Oxidative Chemistry on Gold. *Acc. Chem. Res.* **2009**, *42* (8), 1063.
42. van Duin, A. C. T.; Dasgupta, S.; Lorant, F.; Goddard, W. A., Reaxff: A Reactive Force Field for Hydrocarbons. *J. Phys. Chem. A* **2001**, *105* (41), 9396.
43. Senftle, T. P.; Hong, S.; Islam, M. M.; Kylasa, S. B.; Zheng, Y. X.; Shin, Y. K.; Junkermeier, C.; Engel-Herbert, R.; Janik, M. J.; Aktulga, H. M.; Verstraelen, T.; Grama, A.; van Duin, A. C. T., The Reaxff Reactive Force-Field: Development, Applications and Future Directions. *Npj Comput Mater* **2016**, *2*, 15011.
44. Zhou, G.; Liu, C.; Bumm, L. A.; Huang, L., Force Field Parameter Development for the Thiolate/Defective Au(111) Interface. *Langmuir* **2020**, DOI: 10.1021/acs.langmuir.0c00530.
45. Mercado, R.; Vlasyayjevich, B.; Lin, L. C.; Lee, K.; Lee, Y.; Mason, J. A.; Xiao, D. J.; Gonzalez, M. I.; Kapelewski, M. T.; Neaton, J. B.; Smit, B., Force Field Development from Periodic Density Functional Theory Calculations for Gas Separation Applications Using Metal-Organic Frameworks. *J. Phys. Chem. C* **2016**, *120* (23), 12590.
46. Cohen, A. J.; Mori-Sanchez, P.; Yang, W. T., Challenges for Density Functional Theory. *Chem. Rev.* **2012**, *112* (1), 289.

47. Sousa, S. F.; Fernandes, P. A.; Ramos, M. J., General Performance of Density Functionals. *J. Phys. Chem. A* **2007**, *111* (42), 10439.
48. Cohen, A. J.; Mori-Sanchez, P.; Yang, W. T., Insights into Current Limitations of Density Functional Theory. *Science* **2008**, *321* (5890), 792.
49. Aduri, R.; Psciuk, B. T.; Saro, P.; Taniga, H.; Schlegel, H. B.; SantaLucia, J., Amber Force Field Parameters for the Naturally Occurring Modified Nucleosides in RNA. *J. Chem. Theory Comput.* **2007**, *3* (4), 1464.
50. Pastor, R. W.; MacKerell, A. D., Development of the CHARMM Force Field for Lipids. *J. Phys. Chem. Lett.* **2011**, *2* (13), 1526.
51. Oostenbrink, C.; Villa, A.; Mark, A. E.; Van Gunsteren, W. F., A Biomolecular Force Field Based on the Free Enthalpy of Hydration and Solvation: The GROMACS Force-Field Parameter Sets 53a5 and 53a6. *J. Comput. Chem.* **2004**, *25* (13), 1656.
52. Sun, H., Compass: An Ab Initio Force-Field Optimized for Condensed-Phase Applications-Overview with Details on Alkane and Benzene Compounds. *J. Phys. Chem. B* **1998**, *102* (38), 7338.
53. Jorgensen, W. L.; Maxwell, D. S.; TiradoRives, J., Development and Testing of the Opls All-Atom Force Field on Conformational Energetics and Properties of Organic Liquids. *J. Am. Chem. Soc.* **1996**, *118* (45), 11225.
54. Allinger, N. L., Conformational-Analysis .130. MM2. A Hydrocarbon Force-Field Utilizing V1 and V2 Torsional Terms. *J. Am. Chem. Soc.* **1977**, *99* (25), 8127.
55. Rappe, A. K.; Casewit, C. J.; Colwell, K. S.; Goddard, W. A.; Skiff, W. M., UFF, a Full Periodic-Table Force-Field for Molecular Mechanics and Molecular-Dynamics Simulations. *J. Am. Chem. Soc.* **1992**, *114* (25), 10024.

56. Mayo, S. L.; Olafson, B. D.; Goddard, W. A., DREIDING: A Generic Force-Field for Molecular Simulations. *J. Phys. Chem.* **1990**, *94* (26), 8897.
57. Wick, C. D.; Martin, M. G.; Siepmann, J. I., Transferable Potentials for Phase Equilibria. 4. United-Atom Description of Linear and Branched Alkenes and Alkylbenzenes. *J. Phys. Chem. B* **2000**, *104* (33), 8008.
58. Cai, J.; Ye, Y. Y., Simple Analytical Embedded-Atom-Potential Model Including a Long-Range Force for FCC Metals and Their Alloys. *Phys. Rev. B* **1996**, *54* (12), 8398.
59. Buckingham, R. A., The Classical Equation of State of Gaseous Helium, Neon and Argon. *Proc. R. Soc. Lon. Ser-A* **1938**, *168* (A933), 264.
60. Tersoff, J., Chemical Order in Amorphous-Silicon Carbide. *Phys. Rev. B* **1994**, *49* (23), 16349.
61. Neyts, E. C.; van Duin, A. C. T.; Bogaerts, A., Changing Chirality During Single-Walled Carbon Nanotube Growth: A Reactive Molecular Dynamics/Monte Carlo Study. *J. Am. Chem. Soc.* **2011**, *133* (43), 17225.
62. Petit, C.; Huang, L. L.; Jagiello, J.; Kenvin, J.; Gubbins, K. E.; Bandosz, T. J., Toward Understanding Reactive Adsorption of Ammonia on Cu-MOF/Graphite Oxide Nanocomposites. *Langmuir* **2011**, *27* (21), 13043.
63. Huang, L. L.; Joshi, K. L.; van Duin, A. C. T.; Bandosz, T. J.; Gubbins, K. E., Reaxff Molecular Dynamics Simulation of Thermal Stability of a Cu-3(BTC)(2) Metal-Organic Framework. *Phys. Chem. Chem. Phys.* **2012**, *14* (32), 11327.
64. Huang, L. L.; Gubbins, K. E.; Li, L. C.; Lu, X. H., Water on Titanium Dioxide Surface: A Revisiting by Reactive Molecular Dynamics Simulations. *Langmuir* **2014**, *30* (49), 14832.

65. Shin, Y. K.; Kwak, H.; Vasenkov, A. V.; Sengupta, D.; van Duin, A. C. T., Development of a Reaxff Reactive Force Field for Fe/Cr/O/S and Application to Oxidation of Butane over a Pyrite-Covered Cr₂O₃ Catalyst. *ACS Catal.* **2015**, *5* (12), 7226.
66. Kim, S. Y.; Kumar, N.; Persson, P.; Sofo, J.; van Duin, A. C. T.; Kubicki, J. D., Development of a Reaxff Reactive Force Field for Titanium Dioxide/Water Systems. *Langmuir* **2013**, *29* (25), 7838.
67. Raymand, D.; van Duin, A. C. T.; Spangberg, D.; Goddard, W. A.; Hermansson, K., Water Adsorption on Stepped ZnO Surfaces from Md Simulation. *Surf. Sci.* **2010**, *604* (9-10), 741.
68. Fogarty, J. C.; Aktulga, H. M.; Grama, A. Y.; van Duin, A. C. T.; Pandit, S. A., A Reactive Molecular Dynamics Simulation of the Silica-Water Interface. *J. Chem. Phys.* **2010**, *132* (17), 174704.
69. Wen, J. L.; Ma, T. B.; Zhang, W. W.; van Duin, A. C. T.; Lu, X. C., Surface Orientation and Temperature Effects on the Interaction of Silicon with Water: Molecular Dynamics Simulations Using Reaxff Reactive Force Field. *J. Phys. Chem. A* **2017**, *121* (3), 587.
70. Ai, L. Q.; Zhou, Y. S.; Huang, H. S.; Lv, Y. J.; Chen, M., A Reactive Force Field Molecular Dynamics Simulation of Nickel Oxidation in Supercritical Water. *J. Supercrit. Fluids* **2018**, *133*, 421.
71. van Duin, A. C. T.; Bryantsev, V. S.; Diallo, M. S.; Goddard, W. A.; Rahaman, O.; Doren, D. J.; Raymand, D.; Hermansson, K., Development and Validation of a Reaxff Reactive Force Field for Cu Cation/Water Interactions and Copper Metal/Metal Oxide/Metal Hydroxide Condensed Phases. *J. Phys. Chem. A* **2010**, *114* (35), 9507.

72. Zhu, Z.; Guo, H. K.; Jiang, X. K.; Chen, Y. C.; Song, B.; Zhu, Y. M.; Zhuang, S. L., Reversible Hydrophobicity-Hydrophilicity Transition Modulated by Surface Curvature. *J. Phys. Chem. Lett.* **2018**, *9* (9), 2346.
73. Scocchi, G.; Sergi, D.; D'Angelo, C.; Ortona, A., Wetting and Contact-Line Effects for Spherical and Cylindrical Droplets on Graphene Layers: A Comparative Molecular-Dynamics Investigation. *Phys. Rev. E* **2011**, *84*, 061602.
74. Cheng, G.; Liao, M. R.; Zhao, D. H.; Zhou, J., Molecular Understanding on the Underwater Oleophobicity of Self Assembled Monolayers: Zwitterionic Versus Nonionic. *Langmuir* **2017**, *33* (7), 1732.
75. Zhou, G. B.; Liu, C.; Huang, L. L., Molecular Dynamics Simulation of First-Adsorbed Water Layer at Titanium Dioxide Surfaces. *J. Chem. Eng. Data* **2018**, *63* (7), 2420.
76. Luzar, A.; Chandler, D., Hydrogen-Bond Kinetics in Liquid Water. *Nature* **1996**, *379* (6560), 55.
77. Stillinger, F. H., Water Revisited. *Science* **1980**, *209* (4455), 451.
78. Zhu, C. Q.; Li, H.; Huang, Y. F.; Zeng, X. C.; Meng, S., Microscopic Insight into Surface Wetting: Relations between Interfacial Water Structure and the Underlying Lattice Constant. *Phys. Rev. Lett.* **2013**, *110* (12), 126101.
79. Ferrenberg, A. M.; Swendsen, R. H., Optimized Monte-Carlo Data-Analysis. *Phys. Rev. Lett.* **1989**, *63* (12), 1195.
80. Garcia, A. E.; Sanbonmatsu, K. Y., Exploring the Energy Landscape of a Beta Hairpin in Explicit Solvent. *Proteins* **2001**, *42* (3), 345.
81. Zhou, R. H., Trp-Cage: Folding Free Energy Landscape in Explicit Water. *Proc. Natl. Acad. Sci. USA* **2003**, *100* (23), 13280.

82. Errington, J. R.; Debenedetti, P. G., Relationship between Structural Order and the Anomalies of Liquid Water. *Nature* **2001**, *409* (6818), 318.

Chapter 3: Force Field Parameter Development for the Thiolate/Defective Au(111) Interface*

3.1 Introduction

Self-assembly of thiolates on the gold surface has received extensive attention in nanotechnology, material science, and surface science.¹⁻⁴ For those generated self-assembled monolayers (SAMs) on gold substrates, their properties are significantly influenced by the structural and chemical properties of the gold-thiolate interface.^{1, 5-7} The interfacial gold-sulfur (Au-S) interactions, comparable to the strength of gold-gold bonding,⁵ are accepted to play a critical role to stabilize the gold substrate and regulate the functionality of SAMs. Over the past decades, increasing research interest has been devoted to understanding the molecular nature of the Au-S interface to further promote their applications in nanoelectronics,⁸ biological sensings,⁹ molecular recognition,¹ heterogeneous catalysis,¹⁰ and drug delivery,¹¹ to just name a few.

On the other hand, since the discovery of alkylamines SAMs on Pt by Bigelow *et al.*¹², experimental techniques, such as scanning tunneling microscopy (STM), grazing-incidence X-ray diffraction (GIXRD), X-ray standing waves (XSW), X-ray photoelectron spectroscopy (XPS), and low-energy electron diffraction (LEED), coupled with density functional theory (DFT) calculations, have been routinely utilized to detect the structural evolution of distinct Au-S interface.^{1, 2, 4, 5, 7, 13-15} For example, Nuzzo and coworkers proposed that the Au-S interface is defect-free and S atoms of the thiolates are adsorbed via the three-fold hollow sites of the Au(111) surface.¹⁶ Later, DFT calculation results revealed that the bridge sites seem to be more energetically stable for the adsorption of alkanethiolate (AT) on the pristine Au(111) surface.¹⁷⁻²¹ With the advancement of characterization tools, it is accepted nowadays that the pristine Au(111)

* Zhou, G.; Liu, C.; Bumm, L. A.; Huang, L. Force Field Parameter Development for the Thiolate/Defective Au(111) Interface. *Langmuir* **2020**, DOI: 10.1021/acs.langmuir.0c00530.

surface could undergo a reconstruction during the thiolate adsorption, to generate vacancies and adatoms of the gold substrate and promote different binding sites for S atoms.^{2, 5-7, 15, 22} Of those defective models, the staple motif (S-Au_{ad}-S) model has been recommended, where an intermediate Au adatom is bonded with two S atoms located atop of the Au atoms in the first layer of substrate.^{5, 7} Combining GIXRD experiments and DFT calculations, Scoles and coworkers also proposed a staple motif model where S atoms of thiolates are laterally bound to two Au adatoms of the bridge sites.¹⁵ Additionally, Chaudhuri *et al.*²³ found a completely different adsorption configuration to uncover the $(2\sqrt{3} \times 3)$ rect. phase of butylthiolate SAMs on Au(111). Their LEED experiments show that S atoms of thiolates are located at the top Au adatoms of FCC and HCP hollow sites.

Extensive theoretical efforts have been also developed to the understanding of adatoms and vacancies of gold substrates and how they affect the packing configuration and stability of SAMs.^{4, 15, 24-26} DFT calculations of Wang and Selloni²⁴ showed that the packing structures of c(4×2) AT SAMs are remarkably different from the previously accepted $(\sqrt{3} \times \sqrt{3})R30^\circ$ configuration, if adatom/vacancy of the gold substrate is considered. Torres *et al.*²⁵ investigated the role of Au adatoms to high-density ethylthiolate (ET) SAMs, and their DFT calculations revealed that the number of gold adatoms can significantly influence SAM stability. By comparing the binding and surface energies, they demonstrated that the SAM is most stable where two ET-Au-ET adatom moieties are on top of surface Au atoms.²⁵ Similarly, a large number of classical molecular dynamics (MD) simulations have been also employed to understand the behavior of SAMs.²⁷⁻³¹ However, we note that with the better understanding of defective gold substrate characteristics, a re-parameterization is necessary of force fields to better describe SAM/Au systems .

In this work, we performed a series of DFT and MD simulations to develop force field parameters to accurately describe AT SAMs on the reconstructed Au(111) surface. Those bonded force field parameters were trained to reproduce key features (vibrational spectra and torsion energy profiles) of bridge and staple motif ethylthiolate (C₂S) models on the pristine Au(111) surface. In specific, the force constants of bond and angle terms were trained by matching the vibrational spectra of DFT results. The torsion parameters were optimized via fitting the torsion energy profile of MD to that of DFT calculations. The re-trained force field parameters are applied to study pristine and reconstructed Au-dodecanethiolate (C₁₀S) SAMs with a ($2\sqrt{3} \times 3$) unit cell, and agree well with ab initio molecular dynamics (AIMD) simulation results. The paper is organized as follows: In Section 2, we describe simulation methods and calculation details. Discussions of force field fitting and MD and DFT results are presented in Section 3. Force field validations will be provided in Section 4. Finally, Section 5 has general conclusions and remarks.

3.2 Methods and Simulation Details

3.2.1 Ab-initio DFT Calculation

The DFT calculations are performed by using the Vienna Ab initio Simulation Package (VASP) of the MedeA computational platform.³² The ion–electron interactions were described through the projector-augmented wave (PAW) method³³ and the electron exchange and correlation interactions were represented by the generalized gradient approximation (GGA) of Perdew–Burke–Ernzerhof (PBE) functional.³⁴ The van der Waals interactions were included through the Grimme’s DFT-D3 semi-empirical method.³⁵ A cutoff energy of 450 eV was adopted for the plane-wave basis set and all calculations were carried out using Gaussian smearing with a width of 0.2 eV. The ionic relaxation was converged until the atomic force is less than 0.01 eV Å⁻¹, and the self-consistency was subjected to the successive energy difference of 10⁻⁵ eV. The

slab method was applied to model the Au(111) surface with four atomic layers and a vacuum of 15 Å was added above the surface to avoid the interactions between periodic images. The Au(111) surface consists of a $(2\sqrt{3} \times 3)$ unit cell with 12 Au atoms per layer and the lateral simulation dimensions were $8.70 \times 10.04 \text{ Å}^2$. During the geometry optimization, the entire gold surface was fixed to represent the bulk structure, with the remaining parts being flexible. The obtained equilibrium configurations were used for subsequent calculations. It should be noted that for the vibrational frequency analysis, the entire gold substrate was fixed in both MD and DFT calculations. Among all calculations, the first Brillouin zone was sampled with $6 \times 6 \times 1$ k-points.

3.2.2 Force Field Potential

The force field used in this study to calculate the potential energy has the following functional forms:

$$\begin{aligned}
 U = & \sum_{bonds} K_b (r - r_0)^2 + \sum_{angles} K_\theta (\theta - \theta_0)^2 + \sum_{dihedrals} \sum_{n=1}^4 \frac{K_n}{2} [1 + \cos(n\phi - \gamma)] \\
 & + 4\epsilon_{ij} \left[\left(\frac{\sigma_{ij}}{r_{ij}} \right)^{12} - \left(\frac{\sigma_{ij}}{r_{ij}} \right)^6 \right] + \frac{q_i q_j}{4\pi\epsilon_0 r_{ij}} \quad (3-1)
 \end{aligned}$$

where the first three terms refer to the bonded interactions, namely, the bond, angle, and torsion interactions. K_b and K_θ are corresponding force constants for bonds and angles; r_0 and θ_0 are the equilibrium bond length and angle from DFT-based optimized configurations, respectively. K_n is the force constant for torsions. ϕ is the dihedral angle, and the phase offset γ takes values of 0° or 180° . The latter two terms represent the nonbonded interactions, i.e., van der Waals (vdW) and electrostatic interactions, which were described by the Lennard-Jones (L-J) 12–6 potential and the Coulomb's law, respectively. The Lorentz–Berthelot mixing rule was employed to calculate the vdW interactions between two different atoms. In the present study, the Au and S atoms were considered as uncharged particles and their L-J parameters are taken from the paper by Pradip and

coworkers,²⁷ while the optimized potential for liquid simulations (OPLS) all-atom force field³⁶ is used to describe interactions within the SAMs. Such force field has been widely employed to investigate the behaviors of SAMs on defect-free gold substrate,^{28, 37-41} as well as SAMs-protected gold nanocluster.⁴²⁻⁴³ The vdW and charge parameters used in this study are listed in Table 1.

Table 1. The Lennard-Jones parameters and partial atomic charges used in this work.

Atom type	σ (Å)	ϵ (kcal/mol)	q (e)
Au	2.934	0.039	0.000
S	3.550	0.250	0.000
C(CH ₂)	3.500	0.066	-0.120
C(CH ₃)	3.500	0.066	-0.180
H(CH ₂ , CH ₃)	2.500	0.030	0.060

Previous studies reported a few potential functions to describe the Au-S interface, including the Gupta potential,²² the pairwise L-J potential,⁴⁴⁻⁴⁵ the pairwise Morse potential,⁴⁶ the bond-order Morse-like potential,⁴⁷ and ReaxFF potential.⁴⁸⁻⁴⁹ In this work, we adopt the force field function form of Eqn. (1), which has been widely implemented in numerous MD simulation packages with extensively available force field parameters for molecules and structures. Therefore, developing parameters with this form would facilitate us to study thiolate SAM interactions with other molecules in the future.

3.2.3 Force Field Parameterization.

It is worth noting that despite the number of MD simulation studies of SAM systems in the literature, there is a very limited discussion of force field parameters to SAM's bonded interactions. A common practice is to either fix the Au-S bond or set relevant force constants as zero. In recent

studies, it has been reported that the Au-S interface plays a key role in determining the surface properties of SAMs.⁴ Therefore, keeping the Au-S configuration rigid during the MD simulation will significantly hinder the study of interfacial SAMs. This also justifies the use of two models in the present work. As shown in Figure 4, for the staple motif model, the Au adatom, which is bonded with two S atoms atop of the substrate, locates at the bridge site of the substrate; for the bridge model, the S atom resides at the bridge site of the substrate with the ethyl group pointing towards the hcp hollow site.

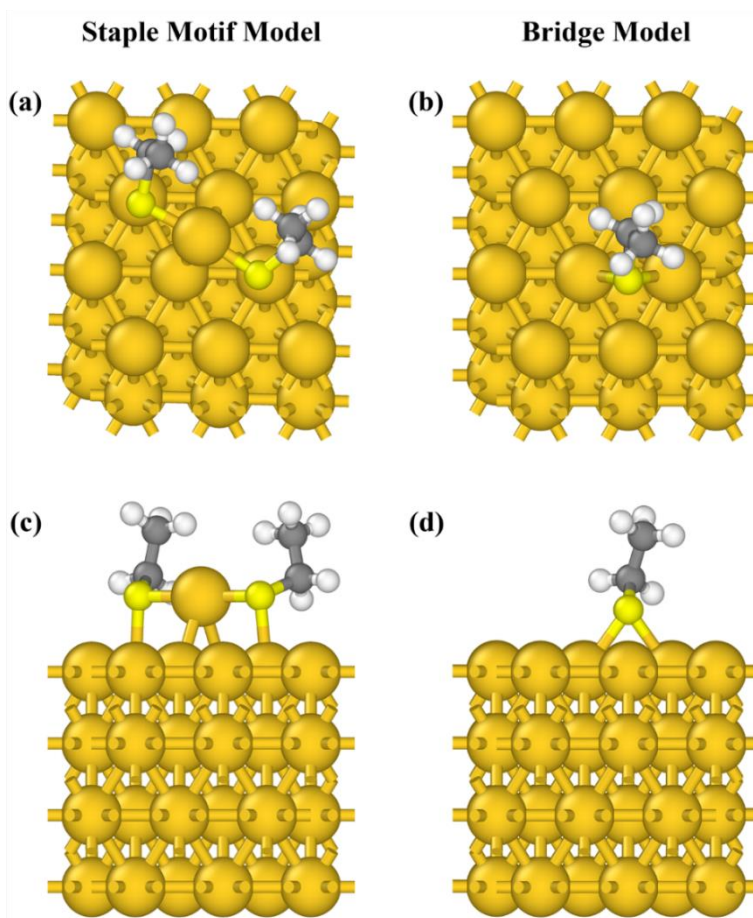


Figure 4. Top view (upper panel) and side view (lower panel) of the optimized structures for the staple motif (a, c) and the bridge (b, d) models. Color code: Au, gold; S, yellow; C, gray; H, white.

The force constants of bonds (K_b) and angles (K_θ) can be obtained by fitting the force field parameters to reproduce the characteristic vibrational frequency.⁵⁰⁻⁵² For the two Au-S interface models considered here, no experimental spectrum data is available. Therefore, we firstly carried out DFT calculations to obtain vibrational modes and frequencies. Those results are then used as the reference for the following MD fitting calculations with the Tinker package.⁵³ The MINIMIZE and VIBRATE modules of Tinker were used to analyze the vibrational modes and frequencies. The Force Field Explorer of Tinker and the Jmol⁵⁴ package are adopted to visualize the vibrational modes from MD and DFT, respectively. K_b and K_θ are fitted until the spectra obtained from MD simulations agree with the results from DFT calculations. As for the torsion terms, a different method was employed to optimize force constants: (a) firstly, DFT calculations were performed to obtain the torsion energy profile as a function of dihedral angles, which vary from 0 to 360° with an interval of 10° (unless specified differently). For each configuration, the geometry was optimized via DFT to obtain the total energy of the system, with the target dihedral angle and the substrate held rigid. (b) secondly, the optimized configuration from DFT was used to obtain the total energy of the system via MD simulation, through the ANALYZE module of the Tinker package. (c) finally, the force constant for the torsion term is obtained by tuning corresponding parameters in Eqn. (1), so that the torsion energy profile from MD agrees well with that from DFT calculations.

3.3 Results and Discussions

3.3.1 Force Field Parameters

3.3.1.1 Vibrational Frequency of Bonds and Angles

Table 2 displays the vibrational frequencies of various modes obtained from both MD and DFT calculations. Generally, the vibrational frequencies from the staple motif and bridge models

are in the range of 150-400 cm^{-1} , which is in a good agreement with other theoretical and experimental measurements.^{6, 55-57} Specifically, in the staple motif model, the Au-S stretching frequencies are 164.9 and 319.1 cm^{-1} from MD, whereas 170.2 and 315.6 cm^{-1} from DFT. The former is from the vertical Au-S stretching mode, while the latter is the horizontal Au-S stretching mode. The two calculated vibration bands (both MD and DFT) agree with the radial and tangential Au-S stretching modes of the thiolate/Au nanocluster system.^{6, 55-57} Furthermore, our results also agree with the previous studies that Au-S vibration bands are between 170 and $\sim 350 \text{ cm}^{-1}$.⁵⁵

Table 2. Typical vibrational frequency of various modes of staple motif and bridge models.

Model	Mode	DFT (cm^{-1})	MD (cm^{-1})	 Relative Difference (cm^{-1})
Staple Motif Model	Au(s)-S(m)	170.2	164.9	5.3
	Au(a)-S(m)	315.6	319.1	3.5
	Au(s)-S(m)-C	163.2	176.2	13.0
	Au(a)-S(m)-C	361.1	361.1	0.0
	Au(s)-S(m)-Au(a)	311.5	303.7	7.8
	S(m)-Au(a)-S(m)	191.4	188.5	2.9
Bridge Model	Au(s)-S(b)	168.4	167.0	1.4
	Au(s)-S(b)-C	122.9	120.5	2.4
	Au(s)-S(b)-Au(s)	335.2	339.1	3.9

In addition, DFT calculations reveal that the Au-S-C bending mode has two bands at 163.2 and 361.1 cm^{-1} . Considering the MD results of 176.2 and 361.1 cm^{-1} and the satisfactory agreement between MD and DFT, the fitted force field parameters provide a good description of the system. In addition, the lower band from MD (176.2 cm^{-1}) also agrees with the Raman spectrum of the Au-S-C bending mode, $\sim 175\text{-}210 \text{ cm}^{-1}$.⁵⁵ We note that prior studies pointed out that this band is

sensitive to the staple type,^{55, 57} indicating that the slightly higher band from the MD calculation might be attributed to the SAM model we use. For other modes of the staple motif model, there is also a satisfactory agreement between the MD and DFT calculations, as listed in Table 2.

As for the bridge model, no experimental spectrum data is available for the Au-S interface. Thus, the vibrational frequencies of various modes in the bridge model were assigned with reference to the staple motif model. The results in Table 2 show that the vibrational frequency of the Au(s)-S(b) stretching mode is 167.0 cm⁻¹(MD)/168.4 cm⁻¹ (DFT), which is close to the counterpart of the tangential Au-S stretching mode.⁶ Moreover, for both Au(s)-S(b)-C and Au(s)-S(b)-Au(s) bending modes, the MD and DFT calculation results agree quite well, with a deviation of less than 4 cm⁻¹. It is worth noting that the vibrational frequencies of that two modes are distinguishable from those of the staple motif model, which is due to the difference of their local structures. Hereto, the relative difference results in Table 2 clearly show that the MD can provide a good prediction for the vibrational motions of bonds and angles at the Au-S interface with both staple motif and bridge models. This means the proposed force field is capable of describing the interactions at the Au-S interface with distinct models. Based on aforementioned MD/DFT comparisons, the obtained force constants for bonds and angles are summarized in Tables 3 and 4.

Table 3. Bond stretching potential parameters for staple motif and bridge models.

Model	Bond	r₀ (Å)	K_b (Kcal/mol·Å²)
Staple Motif Model	Au(s)-S(m)	2.517	45.0
	Au(a)-S(m)	2.318	100.0
Bridge Model	Au(s)-S(b)	2.505	9.0

Table 4. Angle bending potential parameters for staple motif and bridge models.

	Angle	θ_0 (deg)	K_θ (Kcal/mol·rad²)
Staple Motif Model	Au(s)-S(m)-C	105.9	10.0
	Au(a)-S(m)-C	105.8	60.0
	Au(s)-S(m)-Au(a)	93.8	50.0
	S(m)-Au(a)-S(m)	174.7	90.0
Bridge Model	Au(s)-S(b)-C	111.8	37.0
	Au(s)-S(b)-Au(s)	72.7	49.0

3.3.1.2 Energy Profile of Dihedral Angles

The energy profile is constructed by a 2-step process: firstly, the structure is optimized via DFT to obtain the configuration with the lowest energy; secondly, the energy profile is calculated by manually changing the dihedral angle, and the energy difference (ΔE) is recorded with respect to the configuration with the lowest energy. From those energy profiles, we evaluate whether or not the fitted dihedral force field parameters reproduce DFT results. As shown in Figure 5(a), when the Au(a)-S(m)-C-C torsion is in the range of 30° to 100°, there is a satisfactory match between the MD and DFT calculations, with an energy difference of less than 0.08 Kcal/mol. It is worth noting that beyond the equilibrium range of the dihedral angle, the energy profile from MD starts to deviate from that of DFT calculation, with a maximum deviation of about 39 Kcal/mol. This larger deviation comes from the configuration when the terminal CH₃ group of the thiolate is significantly departing from the equilibrium position and pointing towards the substrate. We argue that such configuration could hardly exist in reality, and a careful check on the DFT dispersion interaction correction is probably also needed, if this is the configuration of interest. To the purpose of this work, we only focus on dihedral angles near their equilibrium values.

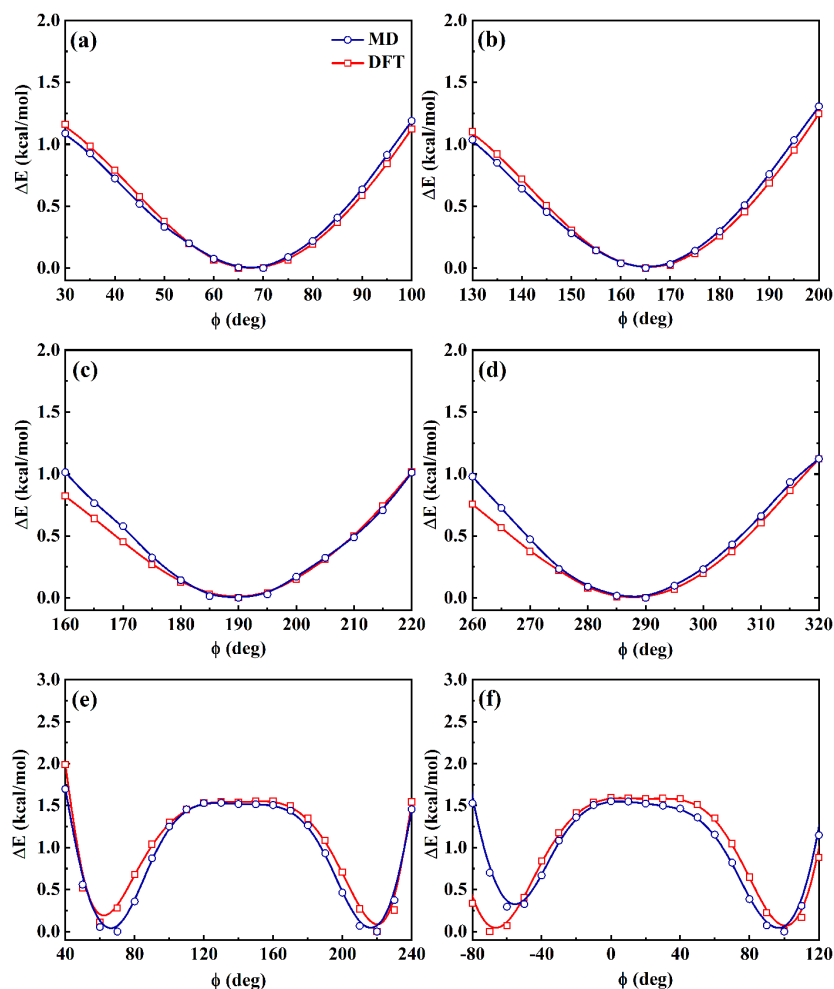


Figure 5. Torsion energy profiles from MD and DFT calculations: (a) Au(a)-S(m)-C-C, (b) Au(s)-S(m)-C-C, (c) Au(a)-S(m)-C-H, (d) Au(s)-S(m)-C-H of the staple motif model; (e) Au(s)-S(b)-C-C and (f) Au(s)-S(b)-C-H of the bridge model. Note: A small interval of 5° was used around the equilibrium dihedral value.

For the Au(s)-S(m)-C-C torsion term, it is clear from Figure 5(b) that, in the interested range of 130° to 200° , the results from MD and DFT agree well with each other, with the energy variation smaller than 0.09 kcal/mol. When it comes to Au(a)-S(m)-C-H and Au(s)-S(m)-C-H, the complete energy profiles from MD simulation exhibit a larger deviation of 7.13 and 6.26 kcal/mol, with respect to corresponding DFT calculations. Similar to aforementioned discussions, when the studied dihedral angle changes around the equilibrium value, both energy profiles provide a

satisfactory match between MD and DFT, see Figures 5(c) and 5(d). The maximal energy variation is about 0.21 and 0.24 Kcal/mol, respectively.

For the bridge model, there are totally two Au(s)-S(b)-C-C and four Au(s)-S(b)-C-H terms. One term of each dihedral angle was considered in this work. The complete energy profiles for Au(s)-S(b)-C-C and Au(s)-S(b)-C-H from DFT calculations are satisfactorily reproduced by MD simulations, with a maximal energy deviation of around 14.88 and 5.49 kcal/mol, respectively. For the dihedral angle near the equilibrium value, as displayed in Figure 5(e), for the Au(s)-S(b)-C-C dihedral angle of 40° to 240°, the energy profile from MD shows an excellent match with the DFT data, with the energy difference less than 0.35 Kcal/mol. In the case of Au(s)-S(b)-C-H dihedral angle of -60° to 120°, Figure 5(f) demonstrates that the torsion energy profiles in that range have a good match between MD and DFT calculations, with the energy difference less than 0.3 Kcal/mol.. The steric hindrance from other chains, particularly in the case of AT molecule with a long alkane chain, will prevent that tilted configuration. The fitting results are available in Table 5 for both staple motif and bridge models.

Table 5. Torsion parameters for both staple motif and bridge models.

Torsions		K₁ (Kcal/mol)	K₂ (Kcal/mol)	K₃ (Kcal/mol)	K₄ (Kcal/mol)
	Au(s)-S(m)-C-C	2.50	0.00	0.00	0.00
Staple Motif Model	Au(a)-S(m)-C-C	0.00	0.00	0.95	0.00
	Au(s)-S(m)-C-H	0.00	0.00	0.30	0.00
	Au(a)-S(m)-C-H	1.60	0.00	0.00	0.00
Bridge Model	Au(s)-S(b)-C-C	2.0	4.45	2.20	0.70
	Au(s)-S(b)-C-H	0.20	0.10	0.20*	0.10

* The phase offset γ in the third term for Au(s)-S(b)-C-H dihedral angle is 180°.

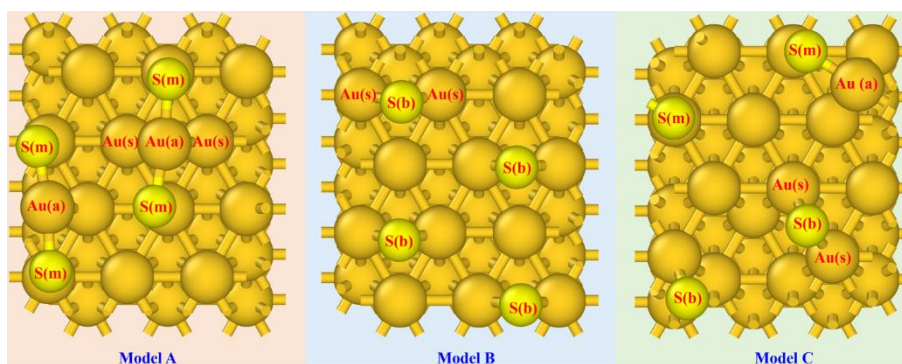


Figure 6. Atomistic structures for three Au-S interface models with a $(2\sqrt{3}\times 3)$ unit cell including four $C_{10}S$ thiolate molecules on the Au(111) surface. Note: the C and H atoms are not shown for clarity. Au(s), Au(a), S(m), and S(b) correspond to the Au atom in the substrate, Au adatom, S atom in the staple motif, and S atom in the bridge model.

3.4 Force Field Validation

3.4.1 Bonds and Angles of $C_{10}S$ Thiolate/Au(111)

To evaluate the newly fitted force field parameters, MD simulations were designed with the Tinker package⁵³ for three Au-S interface models with a $(2\sqrt{3}\times 3)$ unit cell, having four $C_{10}S$ thiolate molecules on the Au(111) surface, as illustrated in Figure 6. The periodic boundary conditions were applied in all three directions with a vacuum of 6.0 nm above the SAMs surface in the z-direction to avoid the interactions between periodic images. Each MD simulation was performed in the canonical (NVT) ensemble. The temperature was set to be 300 K, which is maintained by the Berendsen algorithm with a coupling coefficient of 0.1 ps. The velocity-Verlet algorithm was used to integrate Newton's equation of motion with a time step of 1.0 fs. A cutoff of 1.0 nm was applied for the nonbonded interactions and the long-range electrostatic interactions were treated by the particle mesh Ewald method.⁵⁸ The total simulation time for each model was 10.0 ns, where the first 5.0 ns was for equilibrium and the latter 5.0 ns was for data analysis with the trajectory being updated every 100 steps. Meanwhile, for comparison with the MD simulations,

ab-initio molecular dynamics (AIMD) calculations were also performed with the VASP package of MedeA for the three models. Similar to the MD simulations, those AIMD simulations were using NVT ensemble and the Γ -point sampling of the Brillouin zone was employed. For the AIMD calculations, the time step is 1.0 fs and a calculation of 10.0 ps was carried out for each system, with the first 5.0 ps for equilibrium and the latter 5.0 ps for data analysis at every time step.

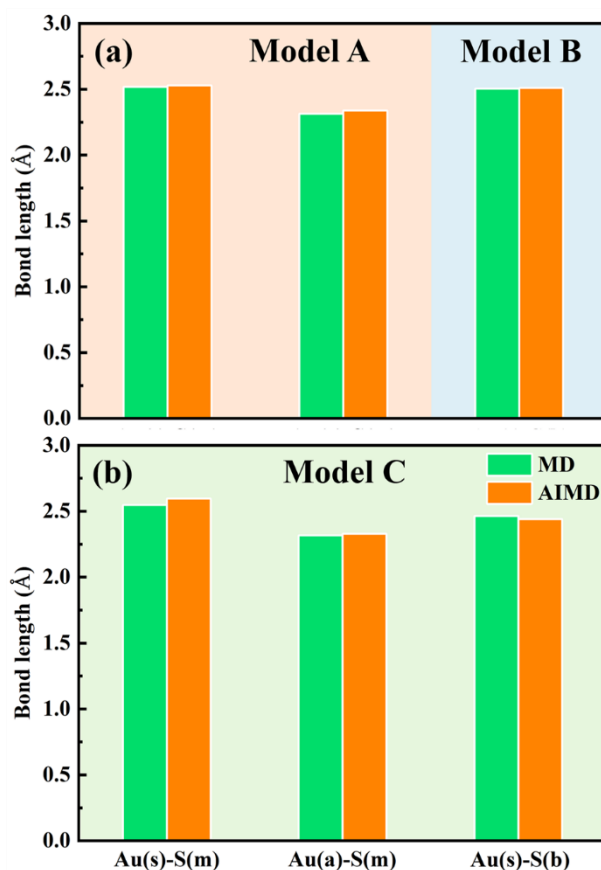


Figure 7. The average bond length for characteristic bonds in (a) model A and B and (b) model C from MD and AIMD calculations at 300 K. All standard deviations are less than ± 0.05 Å. The error bars are smaller than the symbol size, therefore not shown.

We investigated the structural features of the Au-S interface by examining the atomic distances and angles from both MD and AIMD calculations. As presented in Figures 7 and 8, in Model A,

the bond lengths of Au(s)-S(m) and Au(a)-S(m) from AIMD are 2.519 and 2.313 Å, respectively, in an excellent agreement with the MD results of 2.528 and 2.339 Å. The Au(s)-S(b) bond length in Model B is only 0.005 Å shorter than the AIMD value (2.510 Å). For Model C, the Au(s)-S(m) and Au(a)-S(m) bond lengths from MD are 2.547 and 2.318 Å, respectively, while corresponding AIMD calculations predict 2.597 and 2.328 Å. The bond length of Au(s)-S(b) from MD is 0.023 Å longer than that of the AIMD value (2.442 Å).

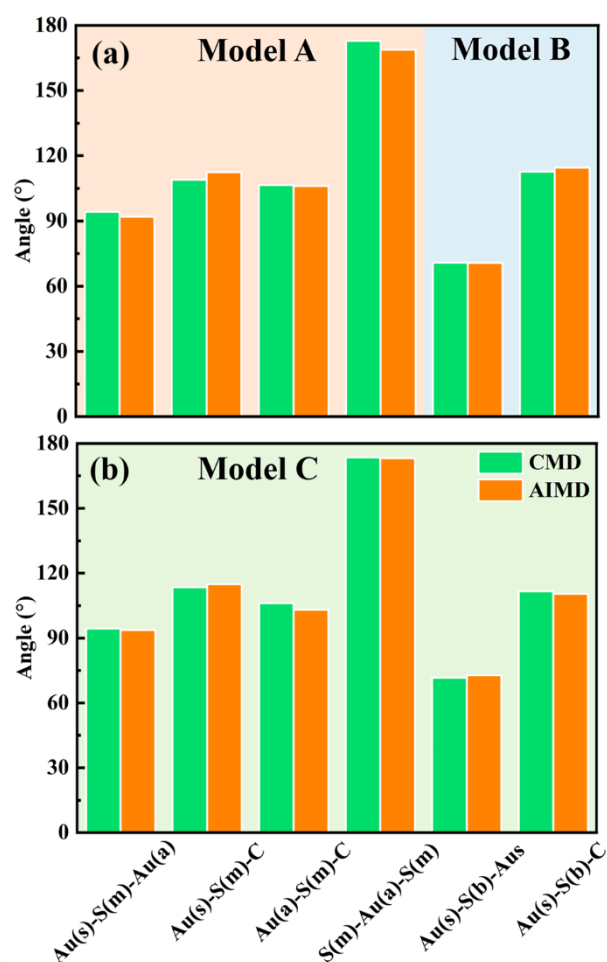


Figure 8. The average angle values for various angles in (a) model A and B and (b) model C from MD and AIMD calculations at 300 K. All standard deviations are less than $\pm 1.5^\circ$. The error bars are smaller than the symbol size, so they are not shown.

In addition, when it comes to the angle values, there is also a good agreement between MD and AIMD calculations. Specifically, in Model A, the Au(a)-S(m)-C is calculated to be 106.49° with MD, and 106.11° with AIMD. For the other three angles, namely, Au(s)-S(m)-Au(a), Au(a)-S(m)-C, and S(m)-Au(a)-S(m), the MD values are also close to the AIMD predictions, with a maximum deviation less than 4.0° . The Au(s)-S(b)-Au(s) and Au(s)-S(b)-C angles in Model B with MD are 70.88° and 112.73° , respectively, while the corresponding values of 70.76° and 114.52° with AIMD calculations. In Model C, the angles, for example, Au(s)-S(m)-Au(a) (94.41°), Au(a)-S(m)-C (106.09°), S(m)-Au(a)-S(m) (173.60°), and Au(s)-S(b)-C (111.55°) from MD are slightly larger than the AIMD results. The opposite trend, namely, DFT predicting a slightly larger value than that of MD, was observed for the other two angles of Au(s)-S(m)-C and Au(s)-S(b)-Au(s). But the absolute numerical difference between MD and AIMD is still negligible. On the other hand, it should be mentioned that the average bond length and angle measurements in Figures 7 and 8 are very close to their equilibrium values from DFT optimized configurations. We thus conclude that the newly developed force field parameters are satisfactorily predicting structural features of all three Au-S interface models in Figure 6.

3.4.2 Alkane Chain Distribution of C₁₀S Thiolate/Au(111)

The density distribution was also calculated of C atoms in the alkane chain along the z-direction, as illustrated in Figure 9. The results demonstrate that for both MD and AIMD calculations, there is a well-defined distribution for the position of the first C atom near the Au(111) surface. The density profiles also reveal the formation of doublet corresponding to pairs of C atoms, while the terminal C atom of CH₃ group shows an isolated peak distribution. In addition, the new force field seems to provide a better prediction to Model B, regarding the C atom distributions. Whereas, in model A, when C atoms are away from the Au(111) surface, for example, starting

with the 5th Carbon atom of the alkane chain, DFT predicts a larger C-surface distance than that from MD. This is probably attributed to vdW interactions from MD and AIMD calculations.⁵⁹ We also note that there is some deviation to the density intensity predicted by MD and AIMD, which is likely resulting from alkane chain flexibility at finite temperatures of AIMD calculations. For model C, the results in Figure 6(c) show that some Carbon peak positions from AIMD calculation were not satisfactorily reproduced by MD simulations. Compared with the unique staple motif in model A and the bridge unit in model B, model C has a combination of staple motif and bridge units, which makes the model a more complex one. Therefore, to have a more detailed comparison between MD and AIMD data, the integrated density distribution profiles in Figure 9(c) have been divided into four individual parts, as shown in Figure 10. For molecules 1 and 2 in the staple motif unit the density distribution profiles show a good agreement between MD and AIMD results for the first four C atoms, after which the MD results start to deviate from those from AIMD, especially in the case of molecule 1. For the two molecules in the bridge unit, the density distribution profiles of molecule 3 from MD agree well with the AIMD results. However, the distribution results of molecule 4 in Figure 10d show that the MD simulation has a good description for the positions of the odd-numbered C atoms, whereas the results of the even-numbered C atoms (except the terminal methyl group) exhibit noticeable deviations from AIMD. This is primarily due to the fact that the vacancy defect is not included in the force field fitting process. Therefore, those bonded interactions in molecule 4 might shift the locations of C atoms from what were predicted in AIMD calculations. In addition, it can be concluded that the obtained force field in this study can provide a good description for the pristine Au-S interface models with unique staple motif or bridge units. However, more force field training efforts will be required to satisfactorily describe the defective Au-S interface model with both vacancy and adatom. The exclusion of

surface vacancy defect during the force field training is responsible for the potential failure to predict vertical locations of C atoms in the bridge SAM molecules.

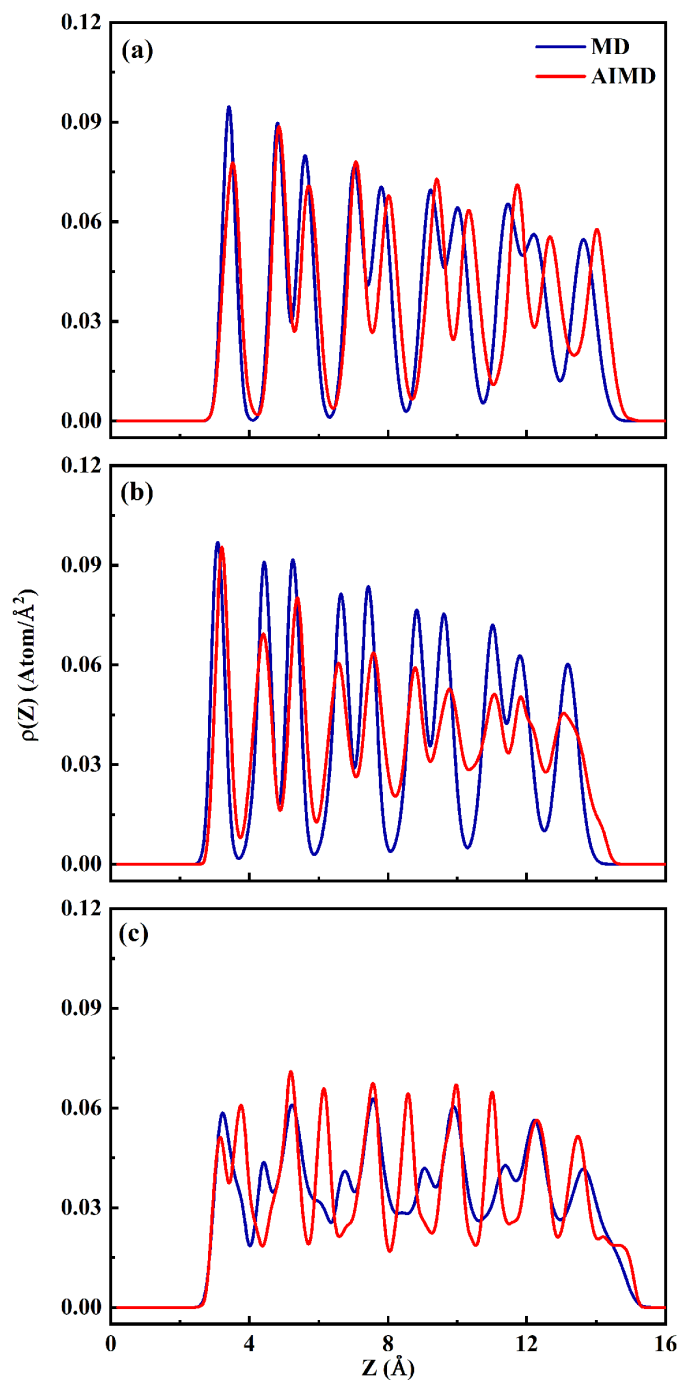


Figure 9. Density distributions of the C atoms in alkane chain along the z-direction for (a) model A, (b) model B, and (c) model C at 300.0 K.

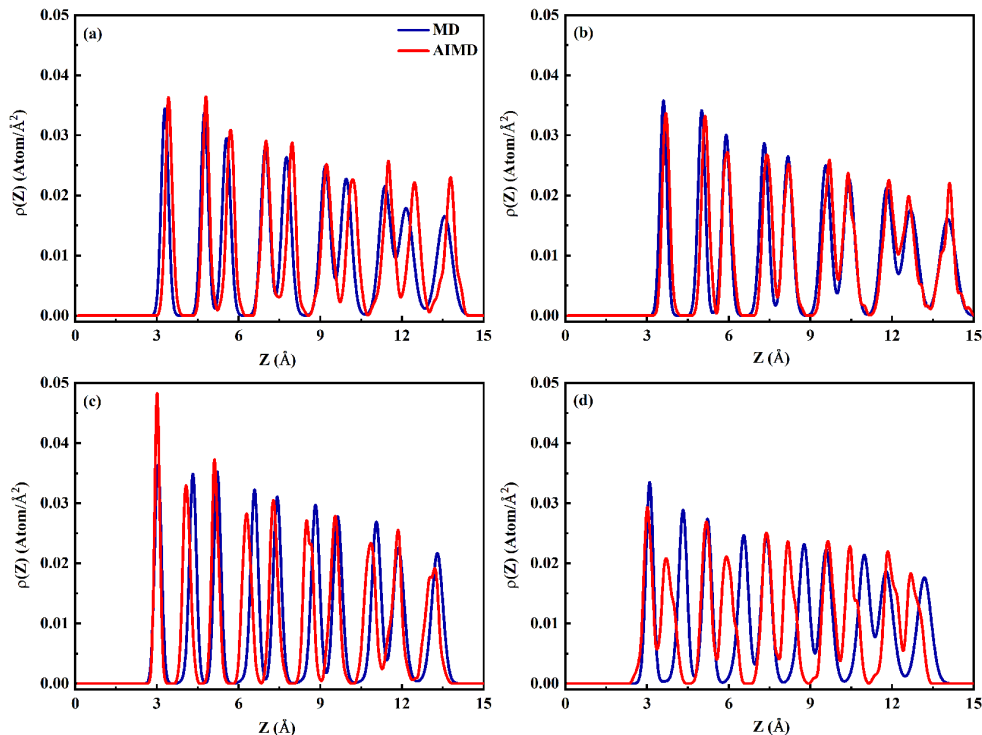


Figure 10. Density distributions of the C atoms in alkane chain along the z direction for (a) molecule 1, (b) molecule 2, (c) molecule 3, and (d) molecule 4 in model C at 200.0 K.

3.4.3 Tilt Angle, Azimuthal Angle and Film Thickness of C₁₀S Thiolate/Au(111)

Lastly, other critical properties of the C₁₀S thiolate, including the tilt angle, the azimuthal angle and the film thickness, are also explored by both MD and AIMD calculations. The tilt angle to the alkane chain was computed as the angle formed between the surface normal and the line passing through the S atom and the centroid of each chain. In Model A, the tilt angle from MD ($36.13 \pm 0.02^\circ$) is slightly larger than that predicted by AIMD calculation ($34.32 \pm 2.48^\circ$). Such a difference is likely due to the peak position difference of the terminal CH₃ group, as shown in Figure 9a. For Models B and C, MD and AIMD agree well about the tilt angle of C₁₀S, with a maximum variation of about 2° . Accordingly, the azimuthal angle is defined as the angle formed between the projection on the x-y plane of the lines passing through the S atom and the centroid of the alkane chain and the unit vector along the x-direction. The results in Table 6 show that, for

the studied three models, the azimuthal angle from MD is in a satisfactory agreement with the AIMD results, with a maximum deviation of less than 5°. Finally, the film thickness is estimated by calculating the distance from the terminal CH₃ group to the gold substrate. The calculations reveal that MD and DFT have an excellent agreement on the film thickness, with a difference within 0.3 Å for three Au-S interface models. Overall, the results in Table 6 demonstrate a good agreement between the MD and AIMD results in tilt angle, azimuthal angle, and film thickness for all three models considered in this study. A detailed comparison among these models reveals that the MD simulation has a better description for the defective model C in tilt angle and film thickness, but for the pristine model B in azimuthal angle. Based on above discussions, we conclude that the fitted force field parameters provide an good description of structural properties of C₁₀S SAMs at the Au(111) surface with different local environments at the Au-S interface.

Table 6. The average tilt angle, azimuthal angle, and film thickness for the alkane chains in model A, B, and C from MD and AIMD calculations at 300 K.

Item	Tilt angle (°)	Azimuthal angle (°)	Film thickness (Å)
Model A MD	36.13±0.02	5.44±0.41	13.55±0.01
AIMD	34.32±2.48	9.99±4.12	13.78±0.30
Relative Difference	1.81±2.46	4.55±3.71	0.23±0.29
Model B MD	35.41±0.05	116.01±0.10	13.07±0.01
AIMD	33.23±2.28	117.10±6.20	13.28±0.30
Relative Difference	2.18±2.23	1.09±6.10	0.21±0.29
Model C MD	30.72±0.07	56.11±0.19	13.81±0.01
AIMD	30.50±4.18	60.88±4.97	13.86±0.39
Relative Difference	0.22±4.11	4.77±4.18	0.07±0.38

3.5 Conclusions

In the present study, periodic ab initio DFT calculations were performed to develop force field parameters to describe AT SAMs at the reconstructed Au(111) surface. The new parameters were carefully trained to reproduce the key features, including vibrational spectra and torsion energy profiles, of C₂S in bridge and staple motif units at the Au(111) surface. The nonbonded force field parameters were directly adopted from the work of Rai *et al.*;²⁷ while the bonded parameters were obtained by reproducing DFT calculation results with iterated MD simulations. In specific, the force constants of bonds and angles were trained by matching the vibrational spectra, while the dihedral parameters were fitted according to the torsion energy profiles. For the vibrational spectra of bonds and angles, MD and DFT agree well with each other, with a maximum deviation about 12 cm⁻¹. Using the fitted parameters, MD simulations can reproduce the dihedral energy profiles from DFT calculations. The agreement is excellent around equilibrium dihedral angles.

In addition, the newly developed force field parameters have been also validated by performing MD simulations for three Au-S interface models by a (2√3×3) unit cell with four C₁₀S SAMs. Those MD results were also compared with AIMD calculation results. Structural features, including the bond length, angle measurement, alkane Carbon locations, the tilt angle, azimuthal angle, and the film thickness of the C₁₀S SAMs, have been calculated. The MD results agree well with those from DFT calculations, which demonstrates a reliability of the developed force field parameters for alkanethiolate SAMs at the reconstructed Au(111) surface.

3.6 References

1. Love, J. C.; Estroff, L. A.; Kriebel, J. K.; Nuzzo, R. G.; Whitesides, G. M., Self-Assembled Monolayers of Thiolates on Metals as a Form of Nanotechnology. *Chem. Rev.* **2005**, *105* (4), 1103.
2. Vericat, C.; Vela, M. E.; Corthey, G.; Pensa, E.; Cortes, E.; Fonticelli, M. H.; Ibanez, F.; Benitez, G. E.; Carro, P.; Salvarezza, R. C., Self-Assembled Monolayers of Thiolates on Metals: A Review Article on Sulfur-Metal Chemistry and Surface Structures. *RSC Adv.* **2014**, *4* (53), 27730.
3. Ulman, A., Formation and Structure of Self-Assembled Monolayers. *Chem. Rev.* **1996**, *96* (4), 1533.
4. Vericat, C.; Vela, M. E.; Benitez, G.; Carro, P.; Salvarezza, R. C., Self-Assembled Monolayers of Thiols and Dithiols on Gold: New Challenges for a Well-Known System. *Chem. Soc. Rev.* **2010**, *39* (5), 1805.
5. Hakkinen, H., The Gold-Sulfur Interface at the Nanoscale. *Nat. Chem.* **2012**, *4* (6), 443.
6. Burgi, T., Properties of the Gold-Sulphur Interface: From Self-Assembled Monolayers to Clusters. *Nanoscale* **2015**, *7* (38), 15553.
7. Pensa, E.; Cortés, E.; Corthey, G.; Carro, P.; Vericat, C.; Fonticelli, M. H.; Benítez, G.; Rubert, A. A.; Salvarezza, R. C., The Chemistry of the Sulfur–Gold Interface: In Search of a Unified Model. *Acc. Chem. Res.* **2012**, *45* (8), 1183.
8. Akkerman, H. B.; Blom, P. W. M.; de Leeuw, D. M.; de Boer, B., Towards Molecular Electronics with Large-Area Molecular Junctions. *Nature* **2006**, *441* (7089), 69.
9. Chaki, N. K.; Vijayamohanan, K., Self-Assembled Monolayers as a Tunable Platform for Biosensor Applications. *Biosens. Bioelectron.* **2002**, *17* (1-2), 1-12.

10. Daniel, M. C.; Astruc, D., Gold Nanoparticles: Assembly, Supramolecular Chemistry, Quantum-Size-Related Properties, and Applications toward Biology, Catalysis, and Nanotechnology. *Chem. Rev.* **2004**, *104* (1), 293.
11. Giljohann, D. A.; Seferos, D. S.; Daniel, W. L.; Massich, M. D.; Patel, P. C.; Mirkin, C. A., Gold Nanoparticles for Biology and Medicine. *Angew. Chem. Int. Edit.* **2010**, *49* (19), 3280.
12. Bigelow, W. C.; Pickett, D. L.; Zisman, W. A., Oleophobic Monolayers .1. Films Adsorbed from Solution in Non-Polar Liquids. *J. Colloid. Sci.* **1946**, *1* (6), 513.
13. Vericat, C.; Vela, M. E.; Benitez, G. A.; Gago, J. A. M.; Torrelles, X.; Salvarezza, R. C., Surface Characterization of Sulfur and Alkanethiol Self-Assembled Monolayers on Au(111). *J. Phys. Condens. Matter* **2006**, *18* (48), R867.
14. Vericat, C.; Vela, M. E.; Salvarezza, R. C., Self-Assembled Monolayers of Alkanethiols on Au(111): Surface Structures, Defects and Dynamics. *Phys. Chem. Chem. Phys.* **2005**, *7* (18), 3258.
15. Cossaro, A.; Mazzarello, R.; Rousseau, R.; Casalis, L.; Verdini, A.; Kohlmeyer, A.; Floreano, L.; Scandolo, S.; Morgante, A.; Klein, M. L.; Scoles, G., X-Ray Diffraction and Computation Yield the Structure of Alkanethiols on Gold(111). *Science* **2008**, *321* (5891), 943.
16. Nuzzo, R. G.; Zegarski, B. R.; Dubois, L. H., Fundamental-Studies of the Chemisorption of Organosulfur Compounds on Au(111). Implications for Molecular Self-Assembly on Gold Surfaces. *J. Am. Chem. Soc.* **1987**, *109* (3), 733.
17. Hayashi, T.; Morikawa, Y.; Nozoye, H., Adsorption State of Dimethyl Disulfide on Au(111): Evidence for Adsorption as Thiolate at the Bridge Site. *J. Chem. Phys.* **2001**, *114* (17), 7615.
18. Vargas, M. C.; Giannozzi, P.; Selloni, A.; Scoles, G., Coverage-Dependent Adsorption of CH₃S and (CH₃S)₂ on Au(111): A Density Functional Theory Study. *J. Phys. Chem. B* **2001**, *105* (39), 9509.

19. Gottschalck, J.; Hammer, B., A Density Functional Theory Study of the Adsorption of Sulfur, Mercapto, and Methylthiolate on Au(111). *J. Chem. Phys.* **2002**, *116* (2), 784.
20. Morikawa, Y.; Liew, C. C.; Nozoye, H., Methylthiolate Induced Vacancy Formation on Au(111): A Density Functional Theoretical Study. *Surf. Sci.* **2002**, *514* (1-3), 389.
21. Molina, L. M.; Hammer, B., Theoretical Study of Thiol-Induced Reconstructions on the Au(111) Surface. *Chem. Phys. Lett.* **2002**, *360* (3-4), 264.
22. Longo, G. S.; Bhattacharya, S. K.; Scandolo, S., A Molecular Dynamics Study of the Role of Adatoms in Sams of Methylthiolate on Au(111): A New Force Field Parameterized from Ab Initio Calculations. *J. Phys. Chem. C* **2012**, *116* (28), 14883.
23. Chaudhuri, A.; Lerotholi, T. J.; Jackson, D. C.; Woodruff, D. P.; Jones, R. G., $(2\sqrt{3} \times 3)$ Rect. Phase of Alkylthiolate Self-Assembled Monolayers on Au(111): A Symmetry-Constrained Structural Solution. *Phys. Rev. B* **2009**, *79* (19), 195439.
24. Wang, J. G.; Selloni, A., The C(4×2) Structure of Short-and Intermediate-Chain Length Alkanethiolate Monolayers on Au(111): A DFT Study. *J. Phys. Chem. C* **2007**, *111* (33), 12149.
25. Torres, E.; Biedermann, P. U.; Blumenau, A. T., The Role of Gold Adatoms in Self-Assembled Monolayers of Thiol on Au(111). *Int. J. Quantum. Chem.* **2009**, *109* (14), 3466.
26. Wang, Y.; Chi, Q. J.; Hush, N. S.; Reimers, J. R.; Zhang, J. D.; Ulstrup, J., Scanning Tunneling Microscopic Observation of Adatom-Mediated Motifs on Gold-Thiol Self-Assembled Monolayers at High Coverage. *J. Phys. Chem. C* **2009**, *113* (45), 19601.
27. Rai, B.; Sathish, P.; Malhotra, C. P.; Pradip; Ayappa, K. G., Molecular Dynamic Simulations of Self-Assembled Alkylthiolate Monolayers on an Au(111) Surface. *Langmuir* **2004**, *20* (8), 3138.
28. Devi, J. M., A Simulation Study on the Thermal and Wetting Behavior of Alkane Thiol SAM on Gold (111) Surface. *Prog. Nat. Sci.* **2014**, *24* (4), 405.

29. Xu, Z.; Song, K.; Yuan, S. L.; Liu, C. B., Microscopic Wetting of Self-Assembled Mono Layers with Different Surfaces: A Combined Molecular Dynamics and Quantum Mechanics Study. *Langmuir* **2011**, *27* (14), 8611.
30. Tobias, D. J.; Mar, W.; Blasie, J. K.; Klein, M. L., Molecular Dynamics Simulations of a Protein on Hydrophobic and Hydrophilic Surfaces. *Biophys. J.* **1996**, *71* (6), 2933.
31. Hung, S. W.; Kikugawa, G.; Shiomi, J., Mechanism of Temperature Dependent Thermal Transport across the Interface between Self-Assembled Monolayer and Water. *J. Phys. Chem. C* **2016**, *120* (47), 26678.
32. Kresse, G.; Furthmuller, J., Efficient Iterative Schemes for Ab Initio Total-Energy Calculations Using a Plane-Wave Basis Set. *Phys. Rev. B* **1996**, *54* (16), 11169.
33. Blochl, P. E., Projector Augmented-Wave Method. *Phys. Rev. B* **1994**, *50* (24), 17953.
34. Perdew, J. P.; Burke, K.; Ernzerhof, M., Generalized Gradient Approximation Made Simple. *Phys. Rev. Lett.* **1996**, *77* (18), 3865.
35. Grimme, S.; Antony, J.; Ehrlich, S.; Krieg, H., A Consistent and Accurate Ab Initio Parametrization of Density Functional Dispersion Correction (DFT-D) for the 94 Elements H-Pu. *J. Chem. Phys.* **2010**, *132* (15), 154104.
36. Jorgensen, W. L.; Maxwell, D. S.; TiradoRives, J., Development and Testing of the OPLS All-Atom Force Field on Conformational Energetics and Properties of Organic Liquids. *J. Am. Chem. Soc.* **1996**, *118* (45), 11225.
37. Goujon, F.; Bonal, C.; Limoges, B.; Malfreyt, P., Description of Ferrocenylalkylthiol SAMs on Gold by Molecular Dynamics Simulations. *Langmuir* **2009**, *25* (16), 9164.
38. Goujon, F.; Bonal, C.; Limoges, B.; Malfreyt, P., Molecular Dynamics Simulations of Ferrocene-Terminated Self-Assembled Monolayers. *J. Phys. Chem. B* **2010**, *114* (19), 6447.

39. Filippini, G.; Israeli, Y.; Goujon, F.; Limoges, B.; Bonal, C.; Malfreyt, P., Free Energy Calculations in Electroactive Self-Assembled Monolayers (SAMs): Impact of the Chain Length on the Redox Reaction. *J. Phys. Chem. B* **2011**, *115* (40), 11678.
40. Kislenko, S. A.; Nikitina, V. A.; Nazmutdinov, R. R., When Do Defectless Alkanethiol SAMs in Ionic Liquids Become Penetrable? A Molecular Dynamics Study. *Phys. Chem. Chem. Phys.* **2015**, *17* (47), 31947.
41. Filippini, G.; Bonal, C.; Malfreyt, P., Atomistic and Energetic Descriptions of Self-Assembled Monolayers of Differently Endgroup-Functionalized Alkanethiols Adsorbed on the Gold Substrate by Using Molecular Simulations. *Soft Matter* **2013**, *9* (20), 5099.
42. Milano, G.; Santangelo, G.; Ragone, F.; Cavallo, L.; Di Matteo, A., Gold Nanoparticle/Polymer Interfaces: All Atom Structures from Molecular Dynamics Simulations. *J. Phys. Chem. C* **2011**, *115* (31), 15154.
43. Munao, G.; Correa, A.; Pizzirusso, A.; Milano, G., On the Calculation of the Potential of Mean Force between Atomistic Nanoparticles. *Eur Phys J E* **2018**, *41* (3), 38.
44. Yang, Z.; Li, Y. Z.; Zhou, G. B.; Chen, X. S.; Tao, D. J.; Hu, N., Molecular Dynamics Simulations of Hydrogen Bond Dynamics and Far-Infrared Spectra of Hydration Water Molecules around the Mixed Monolayer-Protected Au Nanoparticle. *J. Phys. Chem. C* **2015**, *119* (4), 1768.
45. Li, Y. Z.; Yang, Z.; Hu, N.; Zhou, R. F.; Chen, X. S., Insights into Hydrogen Bond Dynamics at the Interface of the Charged Monolayer-Protected Au Nanoparticle from Molecular Dynamics Simulation. *J. Chem. Phys.* **2013**, *138* (18), 184703.
46. Mahaffy, R.; Bhatia, R.; Garrison, B. J., Diffusion of a Butanethiolate Molecule on a Au{111} Surface. *J. Phys. Chem. B* **1997**, *101* (5), 771.

47. Olmos-Asar, J. A.; Rapallo, A.; Mariscal, M. M., Development of a Semiempirical Potential for Simulations of Thiol-Gold Interfaces. Application to Thiol-Protected Gold Nanoparticles. *Phys. Chem. Chem. Phys.* **2011**, *13* (14), 6500.
48. Bae, G. T.; Aikens, C. M., Improved Reaxff Force Field Parameters for Au-S-C-H Systems. *J. Phys. Chem. A* **2013**, *117* (40), 10438.
49. Jarvi, T. T.; van Duin, A. C. T.; Nordlund, K.; Goddard, W. A., Development of Interatomic Reaxff Potentials for Au-S-C-H Systems. *J. Phys. Chem. A* **2011**, *115* (37), 10315.
50. Wang, Y. L.; Shah, F. U.; Glavatskih, S.; Antzutkin, O. N.; Laaksonen, A., Atomistic Insight into Orthoborate-Based Ionic Liquids: Force Field Development and Evaluation. *J. Phys. Chem. B* **2014**, *118* (29), 8711.
51. Liu, Z. P.; Huang, S. P.; Wang, W. C., A Refined Force Field for Molecular Simulation of Imidazolium-Based Ionic Liquids. *J. Phys. Chem. B* **2004**, *108* (34), 12978.
52. de Andrade, J.; Boes, E. S.; Stassen, H., Computational Study of Room Temperature Molten Salts Composed by 1-Alkyl-3-Methylimidazolium Cations-Force-Field Proposal and Validation. *J. Phys. Chem. B* **2002**, *106* (51), 13344.
53. Pappu, R. V.; Hart, R. K.; Ponder, J. W., Analysis and Application of Potential Energy Smoothing and Search Methods for Global Optimization. *J. Phys. Chem. B* **1998**, *102* (48), 9725.
54. Jmol: An Open-Source Java Viewer for Chemical Structures in 3d. <http://www.jmol.org/>.
55. Nieto-Ortega, B.; Burgi, T., Vibrational Properties of Thiolate-Protected Gold Nanoclusters. *Acc. Chem. Res.* **2018**, *51* (11), 2811.
56. Varnholt, B.; Oulevey, P.; Lubner, S.; Kumara, C.; Dass, A.; Burgi, T., Structural Information on the Au-S Interface of Thiolate-Protected Gold Clusters: A Raman Spectroscopy Study. *J. Phys. Chem. C* **2014**, *118* (18), 9604.

57. Varnholt, B.; Guberman-Pfeffer, M. J.; Oulevey, P.; Antonello, S.; Dainese, T.; Gascon, J. A.; Burgi, T.; Maran, F., Vibrational Coupling Modulation in N-Alkanethiolate Protected Au-25(Sr)(18)(0) Clusters. *J. Phys. Chem. C* **2016**, *120* (44), 25378.
58. Essmann, U.; Perera, L.; Berkowitz, M. L.; Darden, T.; Lee, H.; Pedersen, L. G., A Smooth Particle Mesh Ewald Method. *J. Chem. Phys.* **1995**, *103* (19), 8577.
59. Reimers, J. R.; Ford, M. J.; Marcuccio, S. M.; Ulstrup, J.; Hush, N. S., Competition of Van Der Waals and Chemical Forces on Gold-Sulfur Surfaces and Nanoparticles. *Nat. Rev. Chem.* **2017**, *1* (4), 17.

Chapter 4: First Adsorbed Water Layer and its Wettability

Transition under Compressive Lattice Strain*

4.1 Introduction

The water/metal interface is relevant to a broad range of scientific phenomena and technological processes, from astrophysics, electrochemistry, corrosion, heterogeneous catalysis, microelectromechanical devices, to name just a few.¹⁻⁵ When water molecules are in direct contact with the metal surface, forming the first adsorbed water layer (FAWL), a portion of water-water hydrogen bonding interactions would be substituted by stronger water-solid interactions. From the microscopic point of view, the FAWL is a collection of water molecules whose physical and chemical properties are drastically altered by the metal surface.^{3, 5} As a result of the interaction balance, various scenarios have been observed for the FAWL, including water decomposition, ice-like solid structure formation, and non-wetting behavior where water molecules from the FAWL are thermodynamically stabilized by a combination of in-plane water-water and out-plane water-metal interactions.³⁻⁵ In return, the FAWL effectively serves as a one-molecule thin boundary between liquid water and solid metal, mediating liquid properties at those surfaces. There is a pressing need to understand the structure and dynamic properties of the FAWL and comprehend their relevance to and impact on the processes occurred at water/metal interfaces.

Delicately modulating and modifying the wettability of solid surfaces have triggered tremendous research interest in the last decade.⁶⁻¹⁶ Prior studies have demonstrated that the wettability of solid surfaces is directly dominated by the formed FAWL.¹³⁻¹⁹ Low temperature experiments revealed specific in-plane interactions of water molecules of the FAWL dominate the wetting properties of the Pt(111) surface.¹⁹ Molecular dynamics simulations discussed the same

*Zhou, G.; Shoen, B. H.; Yang, Z.; Huang, L. First Adsorbed Water Layer and Its Wettability Transition under Compressive Lattice Strain. *J. Phys. Chem. C* 2020, 124, 4057.

phenomenon for Pt(100) and (111) surfaces at room temperature, where the degree of hydrophobicity of the FAWL was attributed to its passivated hydrogen bond (HB) network.¹⁸ Generally speaking, properties of the FAWL are tunable via balancing the HB interactions within the water monolayer and water-surface interactions,^{3, 5} both of which depending significantly on intrinsic chemistry and structural properties of solid surfaces.^{3, 5, 13-14}

Substantial strategies have been proposed to alter interactions at the water/solid interface which in turn allows the manipulation of interfacial wettability.^{7-18, 20-26} Successful demonstrations include coating hydrophobic graphene to reduce water-surface interactions,²⁰ and chemically adding surface terminal groups (-CH₃, -CF₃, -OH, -COOH, etc.)²¹⁻²⁴ to intentionally weaken or strengthen water-surface interactions. Promising progress has been also achieved from structural manipulations, by the engineering of roughness,^{7-10, 12, 21} curvature,¹⁴ or morphology^{13, 15, 17-18} of solid surfaces. This work presents an alternative manipulation via applying compressive lattice strains to metal surfaces. The malleability, weldability and generally large Young's modulus enable the use of metals and metal junctions under external harsh stresses, while maintaining the integrity and reversibility of metal properties. Scattered studies^{13, 27-28} indicated that lattice strain can affect water/surface interactions, but such knowledge is far from mature.

By a series of molecular dynamics (MD) simulations, we explore the effect of compressive lattice strain on the FAWL formation and its wettability. Three metal surface models have been constructed and investigated, namely, the monometallic Au(100), Pd(100) surfaces and the Pd(100)/Au(100) bimetallic junction. It is worth noting that lattice constants of Au and Pd are 4.08 Å and 3.89 Å, respectively. For the (100) facet, the atomic distance of Au-Au (2.88 Å) and Pd-Pd (2.75 Å) is close to that of water-water (2.77 Å) of an hexagonal close packed (HCP) ice structure, potentially favoring water adsorption at atop Au (or Pd) sites and assisting the formation of the

low-mobility FAWL. For the Pd(100)/Au(100) bimetallic junction, the Au(100) surface with a larger lattice constant was compressed in y direction to match the lattice of the Pd(100) surface. In particular, special attentions have been paid to the structural and dynamical properties, including density and orientation distribution, hydrogen bond dynamics, reorientation rate, and free energy profile, of FAWL on the bimetallic Pd(100)/Au(100) junction system. By comparison, we reported that the FAWL on pristine Pd(100) region is much more stable compared with that on compressed Au(100) region, therefore demonstrating a hydrophobic nature and repelling bulk water from pristine Pd(100) to compressed Au(100).

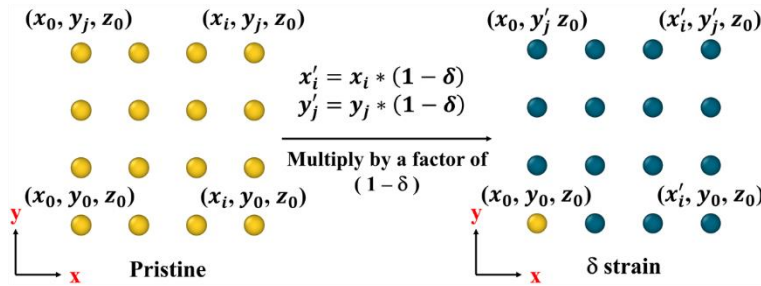


Figure 11. A schematic illustration to the compressive strain applied in the simulations.

4.2 Models and Simulation Details

4.2.1 Surface Models.

Pristine Pd(100) and Au(100) surfaces and a Pd(100)/Au(100) bimetallic junction model have been constructed to investigate properties of the first adsorbed water layer. For compressed pristine surfaces, the strain was applied biaxially along X and Y directions, varying from 0% to 5%. The strain δ , is defined as $\frac{a_0 - a}{a_0}$, where a_0 and a are respectively pristine equilibrium lattice constant and lattice under a compressive strain. The strain is applied by linearly rescaling the x and y coordinates of all the atoms of the substrate by a factor of $(1 - \delta)$, as shown in Figure 11. The

bimetallic junction is consisted of a pristine Pd(100) and a compressed Au(100). A monoaxial strain of 4.61% was applied along the Y direction to Au(100), so that the compressed lattice constant matched that of the pristine Pd(100). The surfaces were kept rigid during all MD calculations. Metal sites were regarded as uncharged and only van der Waals interactions were considered between water and the metal. Non-bonded van der Waals parameters for Pd and Au were derived from the force field developed by Heinz *et al.*,²⁹ which has been widely adopted to probe metal interfacial properties and metal interactions with water and biomolecules.^{14, 17, 30-32} Although the applied force field did not consider the polarization effect, prior studies have demonstrated that the employed force field could qualitatively reproduce both the structure and the interaction energy profile of water on face-centered cubic (FCC) metal surfaces.^{14, 17, 29} The flexible extended simple point charge (SPCE-F) model³³ was used for water, in which the O–H bond and the H–O–H angle are described by harmonic potentials, with the bond constant, k_b , 1108.57 kcal/(mol·Å²) and the angle constant, k_θ , 91.54 kcal/(mol·rad²). Toukan and Rahman³⁴ demonstrated that a flexible SPC water model can provide a good description of water dynamic properties. Furthermore, Yuet and Blankschtein³³ pointed out that the flexibility of the O-H bond plays a key role in the surface tension of water at the interface. Their MD simulation study with the flexible SPC/E water model reported a surface tension of 70.2 mN/m, which agrees well with the experimental value of 71.7 mN/m.³³ For the wettability studies of liquid water, the dynamic diffusion and surface tension are two critical parameters that influence the wetting behavior of water on solid surfaces. Therefore, the flexible SPC/E water model was employed in this work. For the simulation box, the metal surface was fully covered by a water film with a thickness of 1.0 nm. For the choice of the initial water geometry, prior studies¹⁶⁻¹⁷ reported that, when the water film was employed to explore the wettability of solid substrates, a cylindrical nanodroplet was

formed above the FAWL. Bratko and co-workers³⁵ demonstrated that the calculated contact angle from the cylindrical water droplet can minimize the deviation from what is predicted by the Young's equation. An extra vacuum of 5.0 nm was added above the water film in the Z direction to avoid the interactions between periodic images. Periodic boundary conditions were applied in all three directions. The Lennard-Jones (LJ) 12-6 potential was utilized to describe water-water and water-metal van der Waals (vdW) interactions. In addition, water-water electrostatic interactions were described by the Coulomb's law. The LJ parameters and atomic charges used in this study are available from Table S2. The L-J parameters for unlike pairs are obtained using the Lorentz-Berthelot mixing rules, that is, the arithmetic mean (Lorentz's) for size parameters, and the geometric mean (Berthelot's) for energy parameters. While Heinz and co-workers²⁹ used Berthelot's rule for both size and energy parameters, our test calculations show that the choice of the mixing rule does not change the observed phenomena.

4.2.2 Simulation Details.

All MD simulations were carried out with the NVT ensemble by the LAMMPS software package.³⁶ The Nose-Hoover thermostat was used to maintain the temperature of simulation system at 300.0 K with a coupling coefficient of 0.1 ps. Initial velocities of water molecules were assigned according to the Boltzmann distribution. Newton's equation was integrated by the velocity Verlet algorithm with a time step of 1.0 fs. The cutoff for nonbonded interactions was set to be 1.0 nm, with a skin distance of 0.2 nm to store the pairwise neighboring list which was updated every step. The long-range electrostatic interactions were calculated by the particle-particle particle-mesh (PPPM) algorithm with an accuracy of 10^{-5} .³⁷ For each system, a calculation of 30.0 ns was carried out, where the first 15.0 ns was for equilibrium, and the latter

15.0 ns was for data analysis, in which the trajectory was stored every 100.0 fs. After the 30.0 ns simulation, a successive NVT simulation was performed for HB dynamic property calculations, in which the simulation was performed for 500 ps with the trajectory being updated every 5 fs.

4.3 Results and Discussions

4.3.1 Pristine monometallic Pd(100) and Au(100) Surfaces

Figure 12 shows the equilibrium structures of water on pristine metal surfaces. Both Pd(100) and Au(100) host a layer of adsorbed water of one-molecule thickness. For the Pd(100), the formed FAWL demonstrated a hydrophobic nature, stabilizing a water droplet, and such unique phenomenon is independent of water model and initial water geometry. On the contrary, the FAWL of Au(100) is hydrophilic, witnessed by a fully wetting water film. It should be noted that the FAWL is consisted of those water molecules within a distance of 4 Å from the metal surface, which corresponds to the first solvation shell in the density distribution profiles. Such ordered FAWL induced hydrophobicity was observed previously.¹⁶⁻¹⁹ From the perspective of intermolecular interactions, the FAWL results from the competitive yet subtle Gibbs free energy balance between water-water hydrogen bonding and water-metal interactions. The water-metal interactions preferentially substitute water-water interactions of the bulk, gradually changing the interaction strength between the FAWL and surrounding bulk water, and eventually producing the phenomena that other water molecules above the FAWL accumulate to form a water droplet, as revealed at the FAWL of Pd(100). It is worth noting that the size of water droplet at the Pd(100) surface is dominated by the interaction difference between water-water and water-metal, as well as the thickness of initial water film.

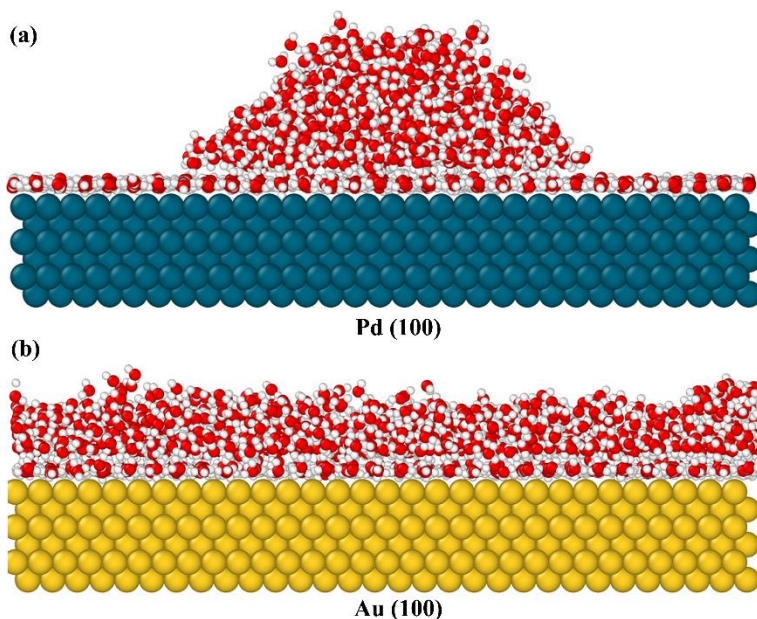


Figure 12. The equilibrium configuration of a 1.0 nm water film on (a) Pd(100); (b) Au(100). An ordered first adsorbed water layer was observed on both surfaces but with significantly different wettability properties: hydrophobic for Pd(100); hydrophilic for Au(100).

4.3.2 Monometallic Pd(100) and Au(100) Surfaces under Compressive Lattice Strain

Under operational conditions, devices are exposed to various stress, therefore yielding different elastic strains. To probe lattice strain effect on the formation of the FAWL and its wettability property, five compressive strains were applied to Pd(100) and Au(100) surfaces, biaxially along the X and Y directions. The strains studied in this work are up to 5%, corresponding to external loads of about 0.3 GPa for Au³⁸ and 5 GPa to Pd,³⁹ which are interpolated from their mechanical property diagrams. Results in Figure 3 reveal an interesting wettability transition due to the applied compressive strain. For comparison, the pristine Pd(100) and Au(100) surfaces are also shown. First of all, the FAWL was observed for both metals under studied strains. When the strain was within 4% for the Pd(100) surface, there existed a stable water droplet on the FAWL. However, when the strain was increased to 5%, a hydrophobic to hydrophilic wettability transition

happened. As demonstrated in Figure 13(a), a complete wetting water film was observed on the FAWL. Phan *et al.*⁴⁰ also reported resembled wetting transition from hydrophobic to hydrophilic for the water droplet on the MgO surface by controlling the vibration of surface atoms. In addition, a similar wettability transition, hydrophilic to hydrophobic, was also observed for the Au(100) surface under compressive strains. For the cases with strains from 2% to 5%, the FAWL of Au(100) surface repels bulk water, generating and stabilizing the formed water droplet. Furthermore, our simulation results also demonstrated that the generated water droplet is not sensitive to the surface flexibility.

To quantitatively describe the wettability transition, we analyzed the contact angle of water droplets. Similar to the work by Zhu and co-workers,¹⁴ we defined the contact angle to be 0° when the water droplet disappears from a hydrophilic FAWL. As shown in Figure 13(c), when the strain is less than 4%, contact angles to water droplets of the Pd(100) surface are 63.09±1.43°, 65.67±2.01°, 72.30±1.31°, 68.20±2.73° and 57.03±1.93°, corresponding to strains of 0%, 1%, 2%, 3% and 4%, respectively. When it comes to the Au(100) surface, the contact angle increases from 0° to 65.0° with the change of compressive strains from 0% to 5%, indicative of a hydrophilic to hydrophobic wettability transition. Upon further increasing the strain to 6% for Au(100) surface, the calculated contact angle is 69.24±0.66°, which is slightly larger than that from the 5% strain case, 65.45±1.32°. In addition, the interaction energy between the FAWL and the metal surface was also calculated. From Figure 13(d), when the formed FAWL demonstrates a distinct hydrophobic nature, there is a significant increase of both the interaction energy between the FAWL and the metal surface, and the HB strength within the FAWL. The enhanced interaction energy would result in a stronger binding strength between the FAWL and the metal surface. Meanwhile, the increased HB strength indicates that water molecules in the FAWL prefer to form

HBs within the monolayer, rather than with other water molecules above the FAWL. By combining the contributions from the two parts, we conclude that the stability of FAWL is largely determined by the interaction energy between the FAWL and metal surfaces. The HB interactions within the monolayer can in turn tune wetting properties of the FAWL. Therefore, a hydrophobic FAWL generally demonstrates a better stability. In other words, water molecules from a more hydrophobic FAWL interact much weakly with water molecules above the FAWL. This trend is also confirmed by the orientational analysis and HB distribution of the FAWL.

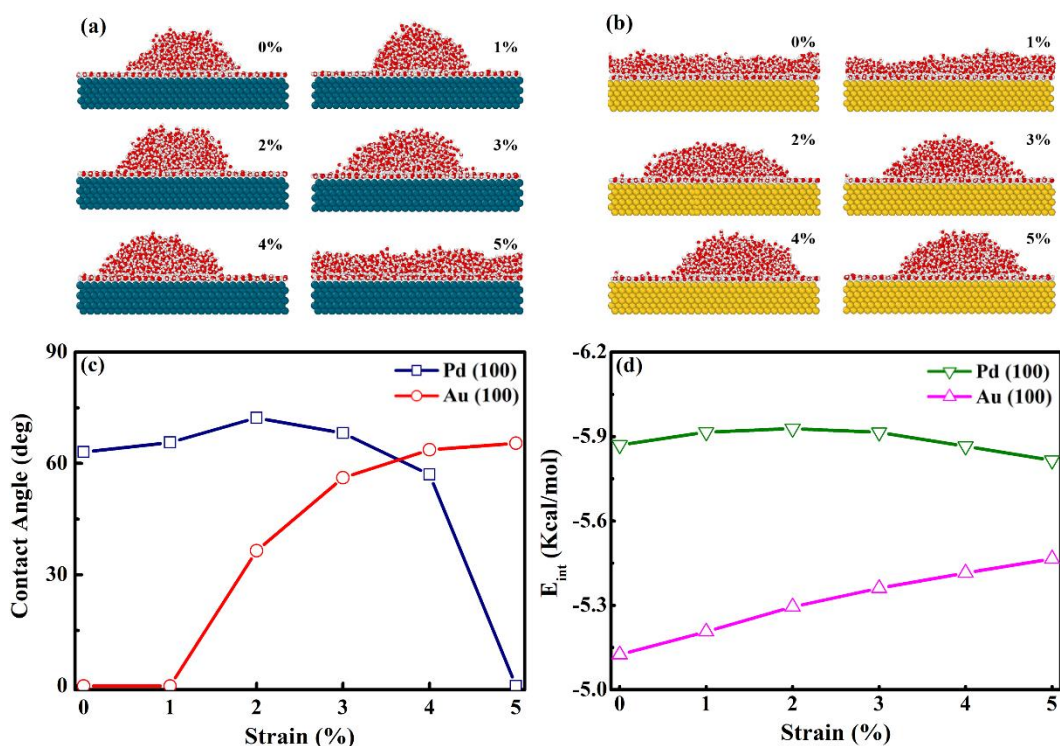


Figure 13. Equilibrium configurations of a 1.0 nm water film on metal surfaces under compressive strains: (a) Pd(100); (b) Au(100). 0% strain represents a pristine metal surface. Strains up to 5% have been studied, corresponding to ~0.3 GPa to Au and ~5.0 GPa to Pd, respectively; (c) Calculated contact angles to water droplets at Pd(100) and Au(100) surfaces; (d) Interaction energies between the FAWL and the metal surfaces. All standard deviations are less than $\pm 2.73^\circ$.

On the other hand, Wang and coworkers¹⁷ pointed out that the lattice constant of the solid substrate also has a significant influence on properties of the FAWL. Therefore, we have estimated the average distance of the adjacent oxygen-oxygen (O-O) in the FAWL. The results in the Table 7 show that, for the hydrophobic FAWL on both Pd(100) and Au(100) surfaces, there is a good match between the lattice constant and average O-O distance of FAWL, which favors the increase of average HB number within the FAWL and a more stable HB network. On the opposite, for the hydrophilic FAWL on both Pd(100) and Au(100) surfaces, the structure of the FAWL would be much more easily disturbed by water molecules above the FAWL, due to the mismatch between the O-O distance and lattice constant, and thereby it is difficult to form the droplet on the FAWL. Such results enable us to conclude that a good match between the lattice constant of substrate and adjacent O-O distance of FAWL would benefit the FAWL to show a feature of hydrophobicity.

Table 7. Lattice constant and water-water distance in FAWL on metal surfaces with various strains. Note: green and yellow refer to the FAWL with hydrophobic and hydrophilic features, respectively.

Substrate	Strain	Lattice Constant (Å)	Water-Water Distance (Å)	Relative Difference (Å)
Pd(100)	0%	2.750	2.754±0.002	0.004
	1%	2.723	2.739±0.002	0.016
	2%	2.695	2.724±0.002	0.029
	3%	2.668	2.718±0.002	0.050
	4%	2.640	2.718±0.003	0.078
	5%	2.613	2.743±0.004	0.130
Au(100)	0%	2.880	2.773±0.003	0.107
	1%	2.851	2.773±0.003	0.077
	2%	2.822	2.776±0.003	0.046
	3%	2.794	2.769±0.002	0.025
	4%	2.765	2.759±0.002	0.006
	5%	2.736	2.748±0.002	0.012

4.3.3 A Bimetallic Junction of Pd(100)/Au(100)

The compressive strain induced wettability transition, in particular, the reverse correlation with respect to Pd(100) and Au(100) surfaces, triggered another fundamental discussion: for a bimetallic junction where the metal with a larger lattice constant is usually compressed to match the lattice of the other metal, what would be the FAWL and its wettability property? In order to shed a light on this question, we constructed a bimetallic junction model consisted of Pd(100) and Au(100) surfaces and studied the wetting behavior of a thin water film on this bimetallic junction. As illustrated in Figure 14, a compressive strain of 4.61% was applied to the Au(100) surface monoaxially along the Y direction to match lattice constants. No strain was applied to the Pd(100) surface. Similar to aforementioned discussions, an initial thin water film of 1.0 nm was then placed on the bimetallic surface (see Figure 14(a)). As expected, an ordered FAWL was formed on the bimetallic junction after equilibrium, as shown in Figure 14(b). More interestingly, a water droplet was observed from the compressed Au(100) region, and there was almost no water molecule left atop of the FAWL of the pristine Pd(100). Multiple independent calculations have been carried out, all returning to the same equilibrium configuration of Figure 14(b) with an averaged contact angle of $62.27 \pm 0.81^\circ$ to the water droplet. It is worth noting that the water droplet is determined by the thickness of the initial water film, that is, the total number of water molecules. When the initial water film was reduced to 0.5 nm, a smaller water droplet was observed. But, for a thicker 1.5 nm initial water film, no water droplet but a full wetting was observed. Our simulation results revealed that, when the system is at a higher temperature of 350 K, the calculated contact angle for the water droplet is $54.60 \pm 0.86^\circ$, smaller than that of the 300 K case, $62.27 \pm 0.81^\circ$, which means the shape of the water droplet is influenced by the temperature.

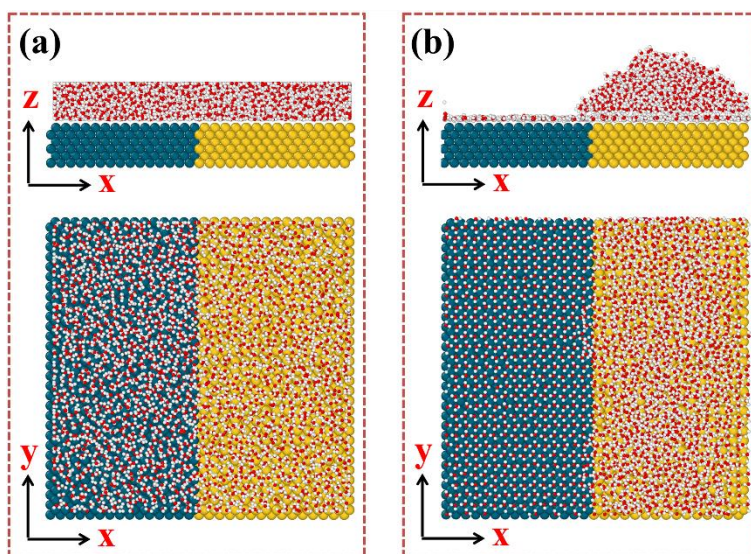


Figure 14. Schematic illustration of the simulation system in of a bimetallic junction model. First, two separate metal surfaces, Pd(100) and Au(100), were prepared and then the Au(100) surface is uniformly compressed in the Y direction (4.61% strain) to match the lattice constant of Pd(100). A water film of 1.0 nm was placed on the obtained bimetallic junction. Side and top views of (a) initial simulation box; (b) the simulation box at equilibrium where a water droplet is on the top of the compressive Au(100) region.

It has been reported that properties of the FAWL directly dominate the behavior of water molecules on top.^{13-19, 24, 28} According to the results in Figure 13, both the pristine Pd(100) and the 4.61 % strain compressed Au(100) could host a hydrophobic FAWL with a water droplet. Therefore, the observed phenomenon of Figure 14 shall originate from the two FAWLs of Pd and Au regions. Detailed analyses have been performed to probe their property difference. Firstly, as presented in Figure 15(a), the distribution of water molecules of the FAWL was revealed by the lateral density characteristic. The location of each water was labeled by the oxygen, Ow. The position of the pronounced first peak, 2.73 Å for Pd(100) and 2.71 Å for Au(100), denotes the distance between the nearest neighboring water molecules in the FAWL. Since the density at the first peak correlates to the packing order, it is obvious that the FAWL of pristine Pd(100) is more

ordered than that of compressed Au(100). As discussed in Figure 13(d), this is primarily ascribed to the interaction between the FAWL and the metal substrate. The FAWL of pristine Pd(100) has a stronger interaction with the metal substrate, -5.909 ± 0.006 Kcal/mol. For compressed Au(100), it is -5.412 ± 0.004 Kcal/mol.

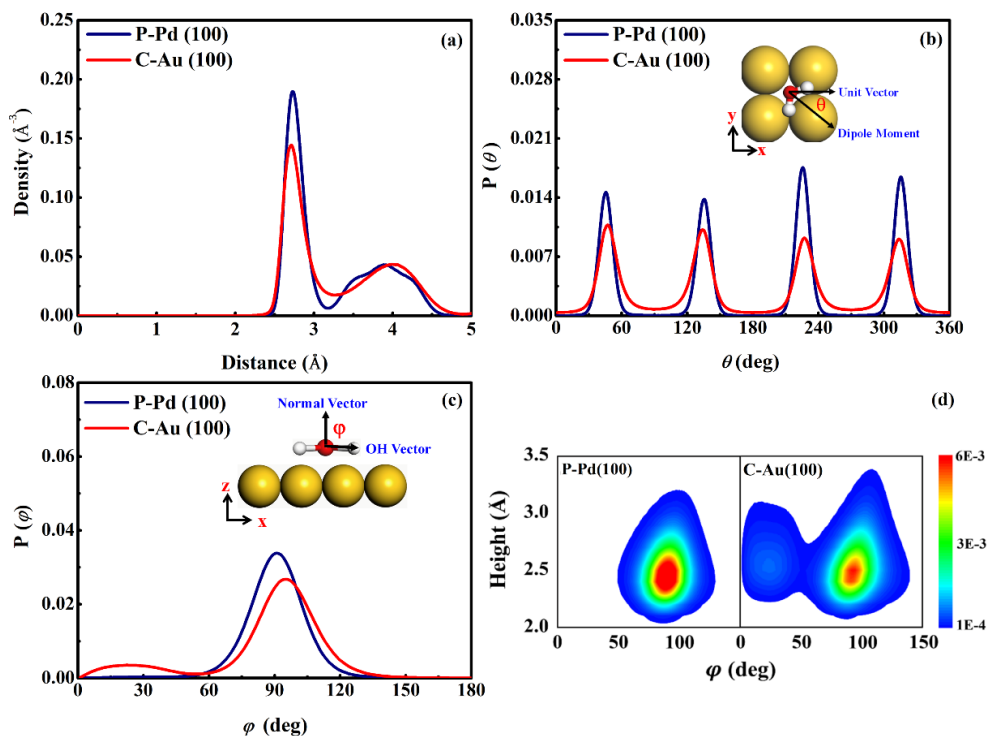


Figure 15. (a) Lateral density distribution of Ow-Ow for water molecules of the FAWL from both the pristine Pd(100) and compressed Au(100) regions; (b) Probability of dipole distribution angle θ , which is defined as the angle between the projection of dipole moment in the x–y plane and the unit vector along the x direction; (c) Probability of O-H bond distribution angle ϕ , formed by the O-H bond and the unit vector normal to the metal substrate; (d) Orientation distribution of water in the FAWL as a function of height h above the substrate and angle formed by the O-H bond and the surface normal vector. Note: the insets of (b) and (c) show schematic illustrations to θ and ϕ angles. Note: the P-Pd(100) and C-Au(100) refer to the pristine Pd(100) and compressed Au(100) surfaces, respectively.

Other static properties also support the conclusion that the pristine Pd(100) has a more stable and a more hydrophobic FAWL. Figures 15(b) and 115(c) are respectively the distribution probabilities of dipole moment and O-H bond of water molecules in the FAWL. As illustrated in the insets, the orientation of water is characterized by angles θ and φ : θ is defined as the angle between the dipole moment projection in the XY plane and the unit vector along the X direction; φ is the angle formed by the O-H bond and the unit vector normal to the metal substrate. For the dipole moment, four characteristic peaks were identified for both Pd and Au, namely, the ones at 45° , 135° , 225° , and 315° . The unanimously larger probabilities (i.e., higher peaks) reveal a more ordered FAWL of pristine Pd(100) than the counterpart of compressed Au(100). For the O-H bond distribution of the FAWL, three potential orientations have been proposed: (a) O-H bonds point towards bulk water on top (B type); (b) O-H bonds are parallel to the substrate surface (P type); (c) O-H bonds point to the substrate surface (S type).¹³ For the pristine Pd(100), water molecules in the FAWL are of the P type, $\sim 90^\circ$, suggesting that O-H bonds are uniformly parallel to the Pd substrate. Whereas on the compressed Au(100) surface, two representative O-H bond distributions were identified, one major peak around 95° and one minor peak around 25° , which correspond to P type O-H bonds parallel to the Au substrate and B type O-H bonds pointing towards bulk water on top, respectively. Those P type O-H bonds form hydrogen bonding network with in-plane neighboring water molecules. The B type O-H bonds suggest that there exists a HB network between the FAWL and the atop bulk water. A detailed HB analysis shows that for the pristine Pd(100), the average number of in-plane HB (FAWL-FAWL) is 3.69, while the number of out-plane HB (FAWL-bulk water atop) is zero. For the compressed Au(100), the values are 3.06 and 0.51, respectively. The correlation of height and O-H bond orientation of water of the FAWL in Figure 15(d) further supports the conclusion that water molecules in the FAWL of pristine Pd(100)

interact exclusively with the Pd substrate and among themselves. In contrast, for the compressed Au(100), a significant amount of water molecules of the FAWL interact with water from the bulk.

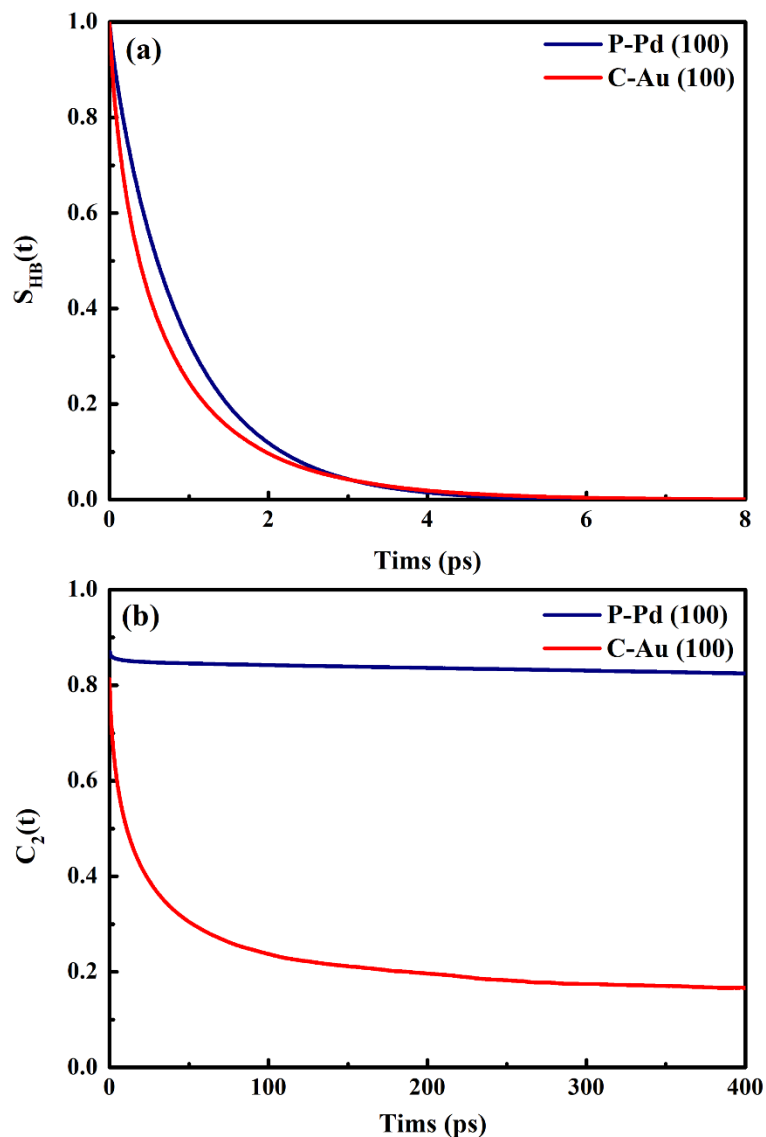


Figure 16. (a) Continuous time correlation functions (TCFs), $S_{HB}(t)$, for the HB network formed within the FAWL on pristine Pd(100) and compressed Au(100) surfaces; (b) The second-order reorientational TCF $C_2(t)$ for water molecules in the FAWL of pristine Pd(100) and compressed Au(100). Note: the P-Pd(100) and C-Au(100) refer to the pristine Pd(100) and compressed Au(100) surfaces, respectively.

The analyses so far have revealed that the formation, the preferential water-metal adsorption sites, and the wettability difference are due to the subtle structural difference of the FAWL at pristine Pd(100) and compressed Au(100). How water of the FAWL behaves dynamically at interfaces is also highly valuable. Using the continuous time correlation functions (TCFs), the HB dynamic property, $S_{HB}(t)$, was calculated and presented in Figure 16(a). As the result shows, for the FAWL of pristine Pd(100), the $S_{HB}(t)$ curve decays evidently slower than that of the compressed Au(100). This suggests a more stable HB network on the pristine Pd(100). Meng and co-workers proposed that the dynamic stability of the FAWL could be characterized by the reorientation rate,¹³ which is derived from the second order Legendre polynomial time correlation function, $C_2(t)$. Figure 16(b) displays the rate of water reorientation of the FAWL on pristine Pd(100) and compressed Au(100). It is prominent that water reorientation decays distinctly slower for the FAWL of the pristine Pd(100) region. Thus, both HB dynamics and water reorientation rate conclude that the FAWL of pristine Pd(100) region is much more stable, demonstrating a hydrophobic nature and repelling other bulk water from pristine Pd(100) to compressed Au(100) region.

Another descriptor to the dynamic stability is the self-diffusion coefficient, which is measured by calculating the mean squared displacement (MSD). The MSD profiles for water molecules on both pristine Pd(100) and compressed Au(100) surfaces increases with respect to the simulation time, particularly for the latter one, of indicative an obvious diffusion feature for liquid state. In addition, the diffusion coefficients of water molecules on pristine Pd(100) and compressed Au(100) surfaces is two and one order of magnitude lower than that of bulk water, respectively. Those results reveal that the self-diffusion of the first adsorbed water layer is generally very slow. To

elucidate the dynamic property difference of the two FAWLs, the free energy profile of water molecules in the FAWL has been calculated according to the following equation:⁴¹

$$\Delta G(x, y) = -k_B T \ln P(x, y) \quad (4 - 1)$$

where $P(x, y)$ is the two-dimensional spatial probability distribution function of the oxygen atom of a water molecule in the FAWL, with its coordinate (x, y) projected to the metal plane; k_B is the Boltzmann's constant; T is the temperature, in this work, 300 K; $\Delta G(x, y)$ is the projected free energy profile, a smaller value representing a stronger interaction and a better stability. This free energy calculation has been successfully employed for the slippage of water molecules on solid surfaces and the free energy profile of protein folding.^{28, 41-43}

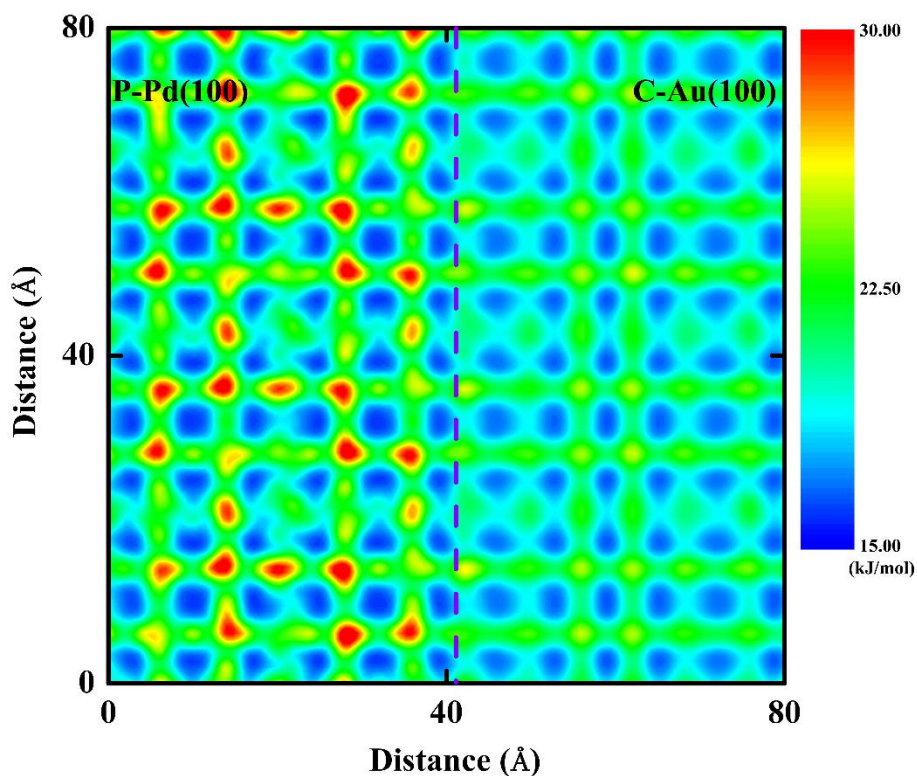


Figure 17. Free energy profile of water molecules in the FAWL of pristine Pd(100) and compressed Au(100) regions. The dash line indicates the boundary of the two regions. Note: the P-Pd(100) and C-Au(100) refer to the pristine Pd(100) and compressed Au(100) surfaces, respectively.

The free energy profile of Figure 17 clearly shows that the free energy profile of the FAWL of pristine Pd(100) is much more corrugated than that of the compressed Au(100) region. The free energy difference from the pristine Pd(100) region reaches 20.22 kJ/mol, while that for the compressed Au(100) is only about 12.72 kJ/mol. That corresponds to a nearly 60% decrease in the free energy profile to the FAWL of the compressed Au(100) region, leading to a much smaller energy barrier to water mobility. To conclude, the FAWL of the pristine Pd(100) region has a larger energy barrier for diffusion, and a higher dynamic stability, which in return favors the departure of bulk water atop, and results in the observed phenomena of Figure 14: water accumulates on top of the compressed Au(100) region while no water stays atop of the FAWL of the pristine Pd(100).

4.4 Conclusion

A rigorous molecular-level description of water at interfaces continues to be a pressing need to nanoscience and advanced manufacturing. This work reports computational studies to understand the behavior of the first adsorbed water layer (FAWL) on metal surface models, namely, Au(100), Pd(100) and a Pd(100)/Au(100) bimetallic junction. Structural and dynamic properties of the FAWL have been discussed in detail. In addition, by applying compressive strains, we reveal a handy manipulation of wettability properties of the FAWL: for pristine metal surface, applying compressive strain can induce a transition of the interfacial wettability, which is mediated by subtle packing changes of the FAWL; for a bimetallic junction, the wettability is more complex, which is balanced by competitive water-water and water-metal interactions. Considering the technology relevance and the known formation descriptor to the FAWL at interfaces, our study elucidates an exciting fundamental understanding to the next level: why a low-mobility water structure repels liquid water and how interfacial wettability could be purposely transited. Since the mobility of

water molecules on the surface is closely related to the temperature, therefore it would be quite interesting and important to explore the temperature effect on the wetting properties of FAWL in the near future.

4.5 References

1. Maier, S.; Salmeron, M., How Does Water Wet a Surface? *Acc. Chem. Res.* **2015**, *48* (10), 2783.
2. Hodgson, A.; Haq, S., Water Adsorption and the Wetting of Metal Surfaces. *Surf. Sci. Rep.* **2009**, *64* (9), 381.
3. Carrasco, J.; Hodgson, A.; Michaelides, A., A Molecular Perspective of Water at Metal Interfaces. *Nat Mater* **2012**, *11* (8), 667.
4. Shimizu, T. K.; Maier, S.; Verdaguer, A.; Velasco-Velez, J.-J.; Salmeron, M., Water at Surfaces and Interfaces: From Molecules to Ice and Bulk Liquid. *Prog. Surf. Sci.* **2018**, *93* (4), 87.
5. Bjorneholm, O.; Hansen, M. H.; Hodgson, A.; Liu, L. M.; Limmer, D. T.; Michaelides, A.; Pedevilla, P.; Rossmeisl, J.; Shen, H.; Tocci, G.; Tyrode, E.; Walz, M. M.; Werner, J.; Bluhm, H., Water at Interfaces. *Chem. Rev.* **2016**, *116* (13), 7698.
6. Tian, Y.; Su, B.; Jiang, L., Interfacial Material System Exhibiting Superwettability. *Adv. Mater.* **2014**, *26* (40), 6872.
7. Liu, K.; Jiang, L., Metallic Surfaces with Special Wettability. *Nanoscale* **2011**, *3* (3), 825.
8. Yao, X.; Song, Y.; Jiang, L., Applications of Bio-Inspired Special Wettable Surfaces. *Adv. Mater.* **2011**, *23* (6), 719.
9. Zhang, S.; Huang, J.; Chen, Z.; Lai, Y., Bioinspired Special Wettability Surfaces: From Fundamental Research to Water Harvesting Applications. *Small* **2017**, *13* (3), 1602992.

10. Wang, Z.; Elimelech, M.; Lin, S., Environmental Applications of Interfacial Materials with Special Wettability. *Environ. Sci. Technol.* **2016**, *50* (5), 2132.
11. Su, B.; Tian, Y.; Jiang, L., Bioinspired Interfaces with Superwettability: From Materials to Chemistry. *J. Am. Chem. Soc.* **2016**, *138* (6), 1727.
12. Xin, B.; Hao, J., Reversibly Switchable Wettability. *Chem. Soc. Rev.* **2010**, *39* (2), 769.
13. Zhu, C.; Li, H.; Huang, Y.; Zeng, X. C.; Meng, S., Microscopic Insight into Surface Wetting: Relations between Interfacial Water Structure and the Underlying Lattice Constant. *Phys. Rev. Lett.* **2013**, *110* (12), 126101.
14. Zhu, Z.; Guo, H.; Jiang, X.; Chen, Y.; Song, B.; Zhu, Y.; Zhuang, S., Reversible Hydrophobicity-Hydrophilicity Transition Modulated by Surface Curvature. *J Phys Chem Lett* **2018**, *9* (9), 2346.
15. van der Niet, M. J.; den Dunnen, A.; Koper, M. T.; Juurlink, L. B., Tuning Hydrophobicity of Platinum by Small Changes in Surface Morphology. *Phys. Rev. Lett.* **2011**, *107* (14), 146103.
16. Wang, C.; Lu, H.; Wang, Z.; Xiu, P.; Zhou, B.; Zuo, G.; Wan, R.; Hu, J.; Fang, H., Stable Liquid Water Droplet on a Water Monolayer Formed at Room Temperature on Ionic Model Substrates. *Phys. Rev. Lett.* **2009**, *103* (13), 137801.
17. Xu, Z.; Gao, Y.; Wang, C.; Fang, H., Nanoscale Hydrophilicity on Metal Surfaces at Room Temperature: Coupling Lattice Constants and Crystal Faces. *J. Phys. Chem. C* **2015**, *119* (35), 20409.
18. Limmer, D. T.; Willard, A. P.; Madden, P.; Chandler, D., Hydration of Metal Surfaces Can Be Dynamically Heterogeneous and Hydrophobic. *Proc. Natl. Acad. Sci. USA* **2013**, *110* (11), 4200.
19. Kimmel, G. A.; Petrik, N. G.; Dohnalek, Z.; Kay, B. D., Crystalline Ice Growth on Pt(111): Observation of a Hydrophobic Water Monolayer. *Phys. Rev. Lett.* **2005**, *95* (16), 166102.

20. Rafiee, J.; Mi, X.; Gullapalli, H.; Thomas, A. V.; Yavari, F.; Shi, Y.; Ajayan, P. M.; Koratkar, N. A., Wetting Transparency of Graphene. *Nat Mater* **2012**, *11* (3), 217-.
21. Dai, X. M.; Sun, N.; Nielsen, S. O.; Stogin, B. B.; Wang, J.; Yang, S. K.; Wong, T. S., Hydrophilic Directional Slippery Rough Surfaces for Water Harvesting. *Sci. Adv.* **2018**, *4* (3), No. eaaq0919.
22. Granick, S.; Bae, S. C., Chemistry: A Curious Antipathy for Water. *Science* **2008**, *322* (5907), 1477.
23. Poynor, A.; Hong, L.; Robinson, I. K.; Granick, S.; Zhang, Z.; Fenter, P. A., How Water Meets a Hydrophobic Surface. *Phys. Rev. Lett.* **2006**, *97* (26), 266101.
24. Guo, P.; Tu, Y.; Yang, J.; Wang, C.; Sheng, N.; Fang, H., Water-CooH Composite Structure with Enhanced Hydrophobicity Formed by Water Molecules Embedded into Carboxyl-Terminated Self-Assembled Monolayers. *Phys. Rev. Lett.* **2015**, *115* (18), 186101.
25. Giovambattista, N. D., P. G.; Rossky, P., Effect of Surface Polarity on Water Contact Angle and Interfacial Hydration Structure. *J. Phys. Chem. B* **2007**, *111*, 9581.
26. Argyris, D. C., D. R.; Striolo, A. , Dynamic Behavior of Interfacial Water at the Silica Surface. *J. Phys. Chem. C* **2009**, *113*, 19591.
27. Chialvo, A. A.; Vlcek, L.; Cummings, P. T., Surface Strain Effects on the Water–Graphene Interfacial and Confinement Behavior. *J. Phys. Chem. C* **2014**, *118* (34), 19701.
28. Zhang, W.; Ye, C.; Hong, L. B.; Yang, Z. X.; Zhou, R. H., Molecular Structure and Dynamics of Water on Pristine and Strained Phosphorene: Wetting and Diffusion at Nanoscale. *Sci. Rep.* **2016**, *6*, 38327.

29. Heinz, H.; Vaia, R. A.; Farmer, B. L.; Naik, R. R., Accurate Simulation of Surfaces and Interfaces of Face-Centered Cubic Metals Using 12-6 and 9-6 Lennard-Jones Potentials. *J. Phys. Chem. C* **2008**, *112* (44), 17281.
30. Fang, G.; Li, W.; Shen, X.; Perez-Aguilar, J. M.; Chong, Y.; Gao, X.; Chai, Z.; Chen, C.; Ge, C.; Zhou, R., Differential Pd-Nanocrystal Facets Demonstrate Distinct Antibacterial Activity against Gram-Positive and Gram-Negative Bacteria. *Nat Commun* **2018**, *9* (1), 129.
31. Heinz, H.; Farmer, B. L.; Pandey, R. B.; Slocik, J. M.; Patnaik, S. S.; Pachter, R.; Naik, R. R., Nature of Molecular Interactions of Peptides with Gold, Palladium, and Pd-Au Bimetal Surfaces in Aqueous Solution. *J. Am. Chem. Soc.* **2009**, *131* (28), 9704.
32. Riccardi, L.; Gabrielli, L.; Sun, X.; De Biasi, F.; Rastrelli, F.; Mancin, F.; De Vivo, M., Nanoparticle-Based Receptors Mimic Protein-Ligand Recognition. *Chem* **2017**, *3* (1), 92.
33. Yuet, P. K.; Blankschein, D., Molecular Dynamics Simulation Study of Water Surfaces: Comparison of Flexible Water Models. *J. Phys. Chem. B* **2010**, *114* (43), 13786.
34. Toukan, K.; Rahman, A., Molecular-Dynamics Study of Atomic Motions in Water. *Phys. Rev. B* **1985**, *31* (5), 2643.
35. Driskill, J.; Vanzo, D.; Bratko, D.; Luzar, A., Wetting Transparency of Graphene in Water. *J. Chem. Phys.* **2014**, *141* (18), 18C517.
36. Lammmps; [Http://Lammmps.Sandia.Gov](http://Lammmps.Sandia.Gov).
37. Hockney, R. W.; Eastwood, J. W. Computer Simulation Using Particles, 2nd Ed.; Iop: Bristol, U.K., 1988.
38. Kim, J.-Y.; Greer, J. R., Tensile and Compressive Behavior of Gold and Molybdenum Single Crystals at the Nano-Scale. *Acta Mater.* **2009**, *57* (17), 5245.

39. Bachurin, D. V.; Gumbsch, P., Atomistic Simulation of the Deformation of Nanocrystalline Palladium: The Effect of Voids. *Modell. Simul. Mater. Sci. Eng.* **2014**, *22* (2), 025011.
40. Phan, A.; Ho, T. A.; Cole, D. R.; Striolo, A., Molecular Structure and Dynamics in Thin Water Films at Metal Oxide Surfaces: Magnesium, Aluminum, and Silicon Oxide Surfaces. *J. Phys. Chem. C* **2012**, *116* (30), 15962.
41. Tocci, G.; Joly, L.; Michaelides, A., Friction of Water on Graphene and Hexagonal Boron Nitride from Ab Initio Methods: Very Different Slippage Despite Very Similar Interface Structures. *Nano Lett.* **2014**, *14* (12), 6872.
42. Ho, T. A.; Papavassiliou, D. V.; Lee, L. L.; Striolo, A., Liquid Water Can Slip on a Hydrophilic Surface. *Proc. Natl. Acad. Sci. USA* **2011**, *108* (39), 16170.
43. Zhou, R. H., Trp-Cage: Folding Free Energy Landscape in Explicit Water. *Proc. Natl. Acad. Sci. USA* **2003**, *100* (23), 13280.

Chapter 5: Molecular Dynamics Simulation of First Adsorbed Water Layer at Titanium Dioxide Surfaces*

5.1 Introduction

The behavior of molecules at titanium dioxide (TiO₂) surfaces is the key to successful applications, from electronic device, catalysis, energy and biomedicine related fields.¹⁻⁵ For most applications at ambient or in the liquid phase, the adsorbed water molecules at TiO₂ surfaces, as well as their structural and dynamics properties, require a fundamental understanding to achieve optimized processes and improved manufactures. From the structural point of view, the topmost TiO₂ surface is composed of under-coordinated titanium (Ti) and oxygen (O) sites, which in turn interacts strongly with interfacial water molecules, and affects significantly the configuration, distribution, and other structural and dynamic properties of those water molecules at TiO₂ surfaces.^{2, 6-8} A number of experiments⁹⁻¹⁴ and theoretical studies^{6, 7, 15-20} have explored the interaction between water and TiO₂ surfaces. Among reported properties, the hydrogen bond (HB) network, both the static network and the dynamic properties, is a sensitive probe to the water/TiO₂ interfacial interactions.²¹⁻²⁷

On the other hand, despite the fundamental importance and the critical role of HB in catalytic reactions,^{28, 29} protein folding,^{30, 31} molecular self-assembly,^{32, 33} and proton transfer,³⁴ the direct measurement of interfacial HB remains as a challenge.^{35, 36} Previously, water adsorption on TiO₂ surfaces has been studied by scanning tunneling microscope (STM)³⁷ and infrared reflection-absorption spectroscopy (IRAS)³⁸ experiments. The adsorbed water molecules atop the five-coordinated titanium (Ti_{5c}) sites form one-dimensional water chain via two types of HBs, namely, the weak HB between adjacent water molecules, and the strong HB between water molecules and

*Zhou, G.; Liu, C.; Huang, L. Molecular Dynamics Simulation of First-Adsorbed Water Layer at Titanium Dioxide Surfaces. *J. Chem. Eng. Data* **2018**, 63, 7, 2420.

bridge-bonded two-coordinated (O_{2c}) sites. For rutile (110) surface covered by two monolayer water, quasi-elastic neutron scattering (QENS) results showed that the first adsorbed water layer (FAWL) is stabilized by HB interactions between the two water layers at the interface.³⁹ In addition, Goletto and co-workers¹⁴ reported high-resolution *in situ* STM images of rutile (110) surface exposed to bulk water. Their results revealed that there is an ordered superstructure of water molecules at the interface. The HB interaction between the FAWL and other water molecules is attributed to such ordered structure, which is in accordance with the QENS experiments.³⁹ More recently, a phase-sensitive sum frequency generation (SFG) spectroscopy study reported that chemisorbed and physisorbed water layers exist simultaneously at the irradiated anatase TiO_2 surfaces.²⁶ The spectroscopic data revealed that there is a strong HB interaction between the two water layers, which contributes to the super-hydrophilic nature of anatase surfaces. It is worth noting that, to the best of our knowledge, no experimental study has been reported on dynamic properties of interfacial HB, which in turn are essential to understand the chemical and physical processes occurring at TiO_2 surfaces.

Molecular dynamics (MD) simulations, including *ab initio* MD (AIMD), reactive MD (RxMD), and non-reactive classical MD, can directly provide an electronic or atomistic level insight of the structural and dynamic properties of HB at the liquid/solid interfaces. For instance, comparing the FAWL at anatase (101) and rutile (110) surfaces, a higher HB was reported for the anatase (101) surface.²⁴ Further HB dynamics analysis demonstrated that the adsorbed water molecules of anatase (101) surface exhibits a longer HB lifetime.²² Moreover, a recent study²⁵ of water wetting on rutile (110) surface illustrated that the HB lifetime for the second water layer is shorter than that of the first water layer. As a result, water molecules from the second layer are relatively easier to escape from the HB network and exchange with water molecules from other

layers. It is also worth noting that for the HB structural and dynamic properties of water at TiO₂ surface, classical force fields provide a satisfying description and can reproduce results from high level AIMD calculations.^{6,7,12,17,19,22–25} In addition, it has been reported that the HB dynamics at water/TiO₂ interface do not depend strongly on polarizable models of water and TiO₂ surfaces.⁴⁰

In a previous work,¹⁵ we examined the interactions between water and TiO₂ surfaces. The RxMD results demonstrated that water interacts strongly with rutile (011), rutile (001) and TiO₂-B (100) surfaces, but weakly with the TiO₂-B (001) surface. Despite the density distribution analysis and the discussions on near-surface water dissociation, no result was reported for the HB properties. In this work, we perform a series of MD calculations to revisit the interfacial HB properties of water on aforementioned four TiO₂ surfaces. A special focus has been paid to the structural and dynamic properties of HBs of the FAWL at surfaces. In particular, the correlation between the HB interactions and the vibrational spectra of water has been discussed in details. The article is organized as follows. Section II presents a brief discussion of the simulation methods and the calculation setup. In Results and Discussion section, we have a discussion about the interfacial HB for water molecules at the surface, the relevant vibrational modes and the relationship between them. Conclusions are summarized in the end.

5.2 Simulation Methods and Details

5.2.1 Surface Models.

In this work, four titanium dioxide surfaces are studied, namely, rutile (110), rutile (011), TiO₂-B (100), and TiO₂-B (001). All surfaces were cleaved from bulk rutile with lattice parameters $a=b=4.593 \text{ \AA}$, $c=2.959 \text{ \AA}$ (symmetry group $P42/MNM$) and bulk TiO₂(B) with lattice parameters $a=12.164 \text{ \AA}$, $b=3.735 \text{ \AA}$, and $c=6.513 \text{ \AA}$ (symmetry group $C2/M$). The surface structures were optimized and kept fixed during the simulation.^{41, 42} The flexible extended simple point charge

(SPC/E) model⁴³ was used for water, in which the O-H bond and the H-O-H angle are described by harmonic potentials: bond constant, k_b , 1108.57 kcal/(mol·Å²); angle constant, k_θ , 91.54 kcal/(mol·rad²). For each calculation setup, the surface was fully covered by a water film with a thickness of 2.0 nm. Periodic boundary conditions were applied in all three directions. The box dimension along the z direction was fixed to be 10.0 nm, which contains the thickness of the surface, the water layer and a vacuum to avoid the interactions between periodic images. The Lennard-Jones (LJ) 12-6 potential was used to describe the van der Waals (vdW) interactions of O_w-O_w and O_w-O (O_w and O correspond respectively to oxygen atoms of water and TiO₂ surface). Meanwhile, the vdW interactions of Ti-O_w and Ti-O were described via the Buckingham potential:

$$E_{ij} = A_{ij} \times \exp\left(-\frac{r_{ij}}{\rho_{ij}}\right) - \frac{C_{ij}}{r_{ij}^6} \quad (5 - 1)$$

Where r_{ij} is the distance between atoms i and j . The first term in the right side represents the repulsive interactions and the second term represents the attractive interactions. When it comes to the force field, the one adopted in this work is from previous work by Bandura and Kubicki,⁴⁴ who have compared the optimized structures of liquid water at rutile (110) surface from both classical and ab initio DFT calculations. Their results demonstrated that the optimized structure of water molecules at the rutile (110) surface using the classical force field is in good agreement with the DFT-based results. Therefore, we think that the force field parameters used here can provide reliable predictions to the water molecules on the TiO₂ surfaces. In addition, the Coulombic interactions between interaction sites is described by the Coulomb's law:

$$E_{ij} = \sum_{i=1}^{N_A} \sum_{j=1}^{N_B} \frac{q_i q_j}{4\pi\epsilon_0 r_{ij}} \quad (5 - 2)$$

In which q_i and q_j are the charges for atoms i and j , and ϵ_0 is the dielectric constant.

5.2.2 Simulation Details.

All simulations were performed using large-scale atomic/molecular massively parallel simulator (LAMMPS) software package.⁴⁵ The canonical ensemble was applied where the number of molecules (N), the volume (V), and the temperature (T) were fixed during the simulation. The temperature (300 K) was maintained by the Nose-Hoover method with the coupling coefficient of 0.1 ps. The initial velocities of water molecules were assigned based on the Boltzmann distribution. The Newton's equation was integrated by the velocity Verlet algorithm with a timestep of 1.0 fs. A cutoff of 1.0 nm was applied for the non-bonded interactions, while the long-range electrostatic interactions were calculated by the particle-particle particle-mesh (PPPM) method.⁴⁶ For each system, a calculation of 20.0 ns was performed, where the first 10.0 ns was for equilibrium and the latter 10.0 ns was used for data analysis, in which the trajectory was analyzed every 100.0 fs. After the 20.0 ns simulation, two successive NVT simulations were also performed: one for the vibrational spectra analysis and the other one for the HB dynamic property calculation. For the vibrational spectra analysis, the simulation was performed for 200 ps with a smaller timestep of 0.5 fs, and the velocity trajectory was updated every 0.5 fs. For the HB property calculation, we ran the simulation for 500 ps and collected the coordinate trajectory every 5 fs. Accordingly, two separate NVT simulations have been carried out for bulk water to obtain the corresponding vibrational spectra and HB properties to be compared with those of the first adsorbed water.

5.2.3 Vibrational Spectra Analysis.

Vibrational spectroscopy is one of the most efficient and effective experimental approaches to probe the structural and dynamic properties of adsorbates at surfaces and interfaces, especially for systems involving hydrogen-bonded interactions.⁴⁷⁻⁵⁰ This is mainly because the vibrational

signals have a sensitive response to the change of local structure environments. For example, first principles MD calculations⁵¹ of water adsorption on TiO₂ (110) surface revealed that the dissociative water adsorption at Ti_{5c} sites results in the terminal and the bridging hydroxyl groups. The stretching frequency was observed for the terminal hydroxyls but not for the bridging ones. This is due to the fact that hydroxyl groups have broadening vibrational bands from the strong HB interactions. Kumar and co-workers⁵² also reported similar broadening phenomena in their AIMD calculations of adsorbed water at TiO₂ surfaces. They discussed that the strong HBs formed between adsorbed water and surface oxygen atoms can produce a noticeable broadening effect in the vibrational band. The dynamic properties of adsorbed water on partially hydroxylated rutile (110) surface has been investigated by Born-Oppenheimer MD simulations.⁵³ The results showed that for adsorbed water, the protons preferentially point to the bridging oxygen atoms, and the resulted stable HB network can lengthen the O-H bonds, leading to a significant red shift of the OH stretching frequency. In this work, we use the vibrational spectra analysis to understand the structure of adsorbed water and the correlation between its configuration and the interfacial HB at TiO₂ surfaces.

5.3 Results and Discussions

5.3.1 Adsorbed Water Structure at TiO₂ Surfaces

To reveal the configuration of adsorbed water at various TiO₂ surfaces, we firstly analyzed water density distribution along the z direction. The position of oxygen atom of water (O_w) is used to represent the center of mass of water molecules. For TiO₂ surfaces, the topmost layer is defined as the reference position, i.e., $z = 0.0$.

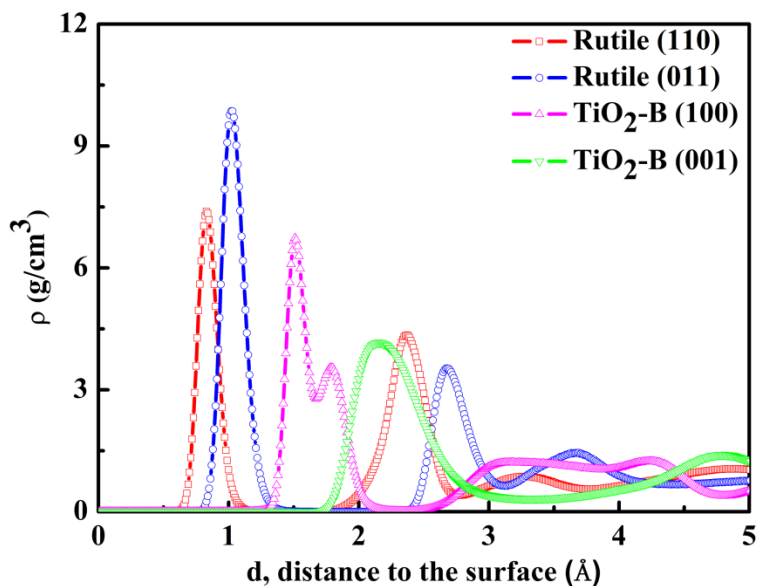


Figure 18. Density distribution of water molecules at different TiO_2 surfaces along the z direction. The surfaces are placed at $d = 0.0 \text{ \AA}$.

5.3.1.1 Rutile (110) Surface

As one of the most stable TiO_2 surfaces, rutile (110) has been extensively studied for the past decades.^{2, 6-8, 54} On this surface, there are four types of atoms that directly interact with water, namely, Ti_{5c} , Ti_{6c} , O_{2c} , and O_{3c} , where the subscript denotes the coordination number. Each under-coordinated Ti_{5c} atom has a dangling bond perpendicular to the surface, making those Ti_{5c} active sites for water adsorption. On the other hand, the O_{2c} atoms are the outmost from the rutile (110) surface, and are potential sites to form HB with water molecules when they are moving close to the surface. As illustrated in Figure 18, for water molecules on the rutile (110) surface, there are two pronounced peaks, 0.83 \AA and 2.37 \AA away from the surface, corresponding to a density value of 7.39 and 4.34 g/cm^3 , respectively. It is worth noting that the two densities are much larger than that of bulk water, 1.0 g/cm^3 . Such high density near the surface implies that interfacial water molecules are packed differently from that of bulk water. The first peak at 0.83 \AA is mainly contributed to the electrostatic interactions between water molecules and the substrate. This is

evidenced that O_w atoms of water molecules locate atop the positively charged Ti_{5c} sites, with two H atoms pointing away from the surface. It is also obvious that water molecules from the FAWL form a well-defined one-dimensional chain, which is also reported in prior studies of the water/rutile (110) system.^{7, 37, 55-57} The second peak at 2.37 Å is from the water molecules that form HBs with surface O_{2c} atoms and other water molecules.

5.3.1.2 Rutile (011) Surface

For the rutile (011) surface, previous studies have demonstrated that water can interact strongly with the surface.^{2, 6-8, 54} At the interface, O_{2c} atoms reside at the apexes and Ti_{5c} atoms are located at lower positions. Both of them are exposed to water molecules, which results in two distinct peaks at 1.03 and 2.68 Å with a density value of 9.86 and 3.53 g/cm³, respectively. For the first peak here, it is primarily from the electrostatic and HB interactions between the FAWL and the surface: water molecules are distributed above the Ti_{5c} sites, which favors electrostatic interactions between O_w and Ti_{5c} . In addition, each water molecule of the FAWL has one H atom pointing towards one surface O_{2c} atom. It is worth noting that *ab initio* DFT calculations and STM experiments^{58, 59} reveal that at room temperature, water can dissociate on the rutile (011) surface. After the dissociation, the H atoms are bonded with the O_{2c} atoms and the hydroxyl groups are bonded with the Ti_{5c} atoms. Due to the use of the non-reactive force field, we did not observe any water dissociation, but the strong HB interaction between water and surface O_{2c} atoms reveals a similar trend and agrees with the literatures. The second smaller peak at 2.68 Å is due to HB interactions of water molecules from adjacent layers.

5.3.1.3 TiO₂-B (100) Surface

For the TiO₂-B (100) surface, previous calculations,^{15, 60, 61} revealed that compared with rutile (110) and (011) surfaces, it has a modest interaction with water. On the surface, there are also four types of atoms directly interacting with the FAWL, namely, Ti_{5c}, Ti_{6c}, O_{2c}, and O_{3c} sites. Similar to the distribution on the rutile (011) surface, the O_{2c} atoms are at the edges and the Ti_{5c} sites are at lower positions. For the density distribution in Figure 18, there is one well-developed peak at 1.51 Å and one less pronounced adjacent peak at 1.79 Å. Such result indicates that at the TiO₂-B (100) surface, there are two configurations for the water molecules of the FAWL. We denote the two configurations as “H-down” and “H-up”, respectively. For the “H-up” configuration, H atoms point away from the surface, with O_w atoms at the top of the Ti_{5c} sites through electrostatic interactions. But for the “H-down” configuration, H atoms point to the surface, which facilitates the HB formation with the interface O_{2c} atoms. By comparing their relative distance to the surface, we conclude that the first peak is from “H-up” water molecules while the second peak is due to the “H-down” ones.

5.3.1.4 TiO₂-B (001) Surface

Lastly, for the TiO₂-B (001) surface, there are Ti_{5c}, O_{2c}, and O_{3c} sites at the interface, and our previous study observed a weak interaction of water at this surface.¹⁵ The density profile of Figure 18 shows that there is only one distinct peak at 2.15 Å for the TiO₂-B (001) surface. Comparing the four studied surfaces, the peak from the TiO₂-B (001) surface is much lower and broader. The peak position is also the furthest from the surface. This suggests that water interacts weakly with the TiO₂-B (001) surface, and the FAWL is less ordered. Water molecules on the other three surfaces form one- or two-dimensional structures, but the distribution of water molecules on the

TiO₂-B (001) surface is random. Nevertheless, as shown in Figure 19, because of the weak interaction between water and the substrate, at the TiO₂-B (001) surface, water molecules of the FAWL can easily reorganize and form small clusters via HB interactions. In particular, the C(2×2) and P(3×2) patterns appear to be quite stable at the studied room temperature. Similar HB assisted water clusters have been also reported on other metal oxide surfaces.⁶²

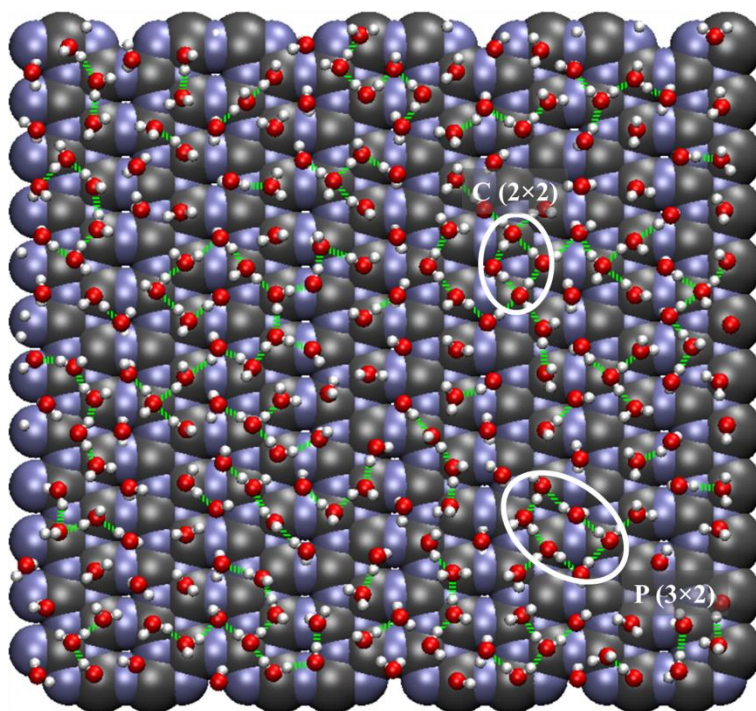


Figure 19. Top view of the FAWL on the TiO₂-B (001) surface at $t = 20.0$ ns: HB assisted water clusters. The HBs are in green, while the Ti and O atoms are colored by gray and blue, respectively.

5.3.2 Orientation Analysis of Adsorbed Water

To further understand the structure details of adsorbed water molecules, we analyzed the orientational distributions of water molecules from the first density profile peak. As illustrated in the inset of Figure 20, the orientational angle θ is defined as the angle between the OH vector and the unit vector normal to the surface in the z direction. For the FAWL on rutile (110) surface, the

orientation angle analysis in the Figure 20 shows that there is only one sharp peak at about 55° , indicating that each water molecule in the FAWL has two H atoms pointing away from the surface. While for the rutile (011) surface, two orientational angles were identified at 107° and 35° . This suggests that water molecules have one H atom pointing to the surface and the other H atom pointing to bulk water. Such orientation facilitates the HB formation for both FAWL/surface and FAWL/other water molecules. Moreover, for water molecules at the $\text{TiO}_2\text{-B}$ (100) surface, there are two pronounced peaks at 54 and 128° . We can deduce that the two peaks correspond to the “H-up” and “H-down” configurations. When it comes to the $\text{TiO}_2\text{-B}$ (001) surface, the orientation distribution is different. One broad peak around 90° was observed, which agrees with our previous RxMD results.¹⁵ Such orientation suggests that the O-H bonds are parallel to the $\text{TiO}_2\text{-B}$ (001) surface, and water molecules from the FAWL can form HBs easily with each other.

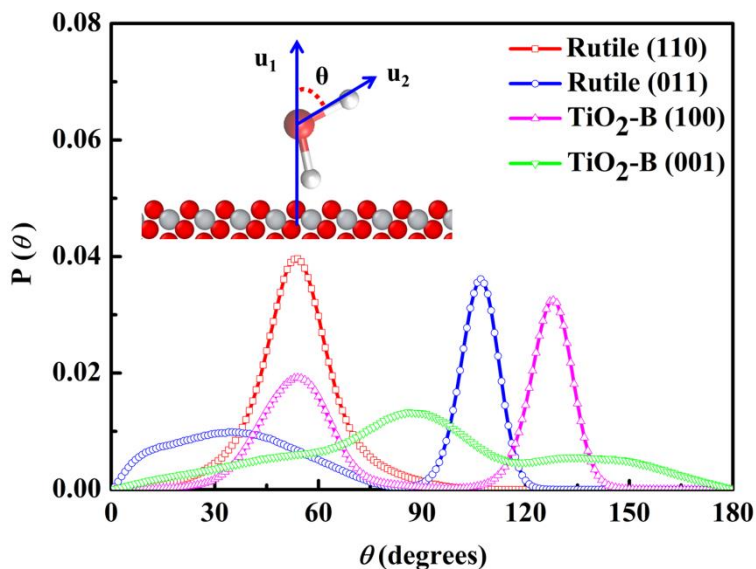


Figure 20. Angular distribution of the FAWL at TiO_2 surfaces: \mathbf{u}_1 is the unit vector normal to the surface; \mathbf{u}_2 is the vector pointing from O atom to H atom; θ is the angle defining the two vectors.

5.3.3 Vibrational Spectra Analysis of Adsorbed Water

Vibrational spectra analysis is a very useful tool to characterize the structures of water molecules at interfaces. It can be also calculated from MD simulations by employing the Fourier transformation of the velocity autocorrelation function (VACF). In this study, we calculated the vibrational spectra of water molecules from the FAWL at the four TiO₂ surfaces, to explore the correlation between the spectra information and the HB network of water. The normalization of VACF is defined by^{63, 64}

$$C_v(t) = \frac{\langle \vec{v}_i(0)\vec{v}_i(t) \rangle}{\langle \vec{v}_i(0)\vec{v}_i(0) \rangle} \quad (5-3)$$

where $\vec{v}_i(t)$ represents the velocity of atom of type i (H or O_w atoms) in the defined interfacial region at time t . The angular brackets denote the ensemble average, which is evaluated at different initial reference times. The vibrational density of states (VDOS) can be calculated from the Fourier cosine transformation of VACF:^{64, 65}

$$S(\omega) = \int_0^\alpha C_v(t) \cos(\omega t) dt \quad (5-4)$$

In this work, we mainly focus on the stretching mode of O-H bonds in the high-frequency region. For the water molecules at TiO₂ surface, such as, the water/rutile (110) system, the intensity of $S(\omega)$ for H atoms is much higher than that of O atoms, suggesting that the dominant contribution to the O-H stretching vibration results from the $S(\omega)$ of H atoms. Therefore, here the normalized VACF is calculated only for the H atoms in the FAWL, so the calculated VDOS contains only the characteristic peaks of H atoms.

5.3.3.1 Rutile (110) Surface

As shown in Figure 21, the peaks around 3690 and 3750 cm^{-1} are characteristic of the stretching mode of the O-H bonds in bulk water, which agrees with the experiments and other calculation.⁴⁴ For the interfacial water, the results show that there are two characteristic peaks for O-H bond stretching mode of the FAWL at rutile (110), rutile (011), $\text{TiO}_2\text{-B}$ (001) but not the $\text{TiO}_2\text{-B}$ (100) surface, where three characteristic peaks were identified in the same region for the interfacial water. In detail, Figure 21(a) shows that the peaks for OH vibration modes at the rutile (110) surface are located around 3700 and 3770 cm^{-1} . Compared with the bulk water vibration modes, there is a blue shift of 10 and 20 cm^{-1} , respectively. It is worth noting that similar results have been observed by Xantheas and Dunning⁶⁶ and their DFT calculations demonstrated that the vibrational modes of hydrogen-bonded O-H bonds in water dimer has a characteristic peak at 3712 cm^{-1} (aug-cc-pVDZ) or 3748 cm^{-1} (aug-cc-pVTZ), quite close to the experimental value of 3718 cm^{-1} .⁶⁷ We performed an analysis to use the HB assignment to do the vibrational analysis based on the type of HB that involves the H atoms. That is, the assignment for the O-H bonds at the rutile (110) surface should be the donor bridge H stretch according to the normal modes definition stated in previous studies.⁶⁶ The results (3690 and 3750 cm^{-1}) here agree well with those reference values. While for the same water/rutile (110) system, experimental inelastic neutron scattering (INS) spectra results show that the OH vibration modes have two peaks at 412 (3322 cm^{-1}) and 416 meV (3354 cm^{-1}).^{68, 69} The difference between the experimental values and the calculation results is probably from the different temperatures: in this work, the MD simulations are performed at 300.0 K, while the temperature of the INS spectra experiments is at 4 K. As for the calculated frequency values, when one compares the calculation with the experiments, it is important to consider the following factors: (a) the temperature. For example, the ab initio MD (AIMD) simulations by

Mattioli *et al.*,¹⁷ have performed AIMD calculations to investigate the structural and vibrational properties of a water bilayer adsorbed on anatase (101) surface at different temperatures. Their calculated results demonstrated that at 50 K, the stretching mode of O-H bonds of water has three distinguishable vibrational frequencies at 2530, 2970, and 3290 cm^{-1} . On the other hand, when the temperature is 300 K, the spectra show an unresolved broad band at around 3400 cm^{-1} for the O-H stretching modes. Such observation demonstrates that the increase in temperature will result in a higher O-H vibrational frequency. (b) the nature of the surface. One other factor that affects the vibrational spectra is the structural and chemical properties of the pristine surface. As discussed, the four studied TiO_2 surfaces have their unique configurations. The anatase (101) surface is different from the rutile (110) surface, which results in different interactions with near surface water molecules. Therefore, the vibrational spectra of water on that two surfaces shall be different from each other. (c) the computational model and force fields. Kavathekar and co-workers⁷⁰ applied a flexible simple point charge (SPC) water model and calculated the vibrational spectra of water at different TiO_2 surfaces. They found that the O-H vibration modes at rutile (110) surface have a broad band at 3453 cm^{-1} . While for other TiO_2 surfaces, the corresponding modes generally have two characteristic peaks: rutile (101), 3571 and 3663 cm^{-1} ; rutile (001), 3538 and 3656 cm^{-1} ; anatase (101), 3600 and 3669 cm^{-1} ; anatase (001), 3584 and 3674 cm^{-1} . Considering the results from our flexible SPC/E model, it is obvious that the choice of computational model and force field can influence the calculated vibrational spectra results. It is also worth noting that calculated vibrational frequencies are typically larger than those from experiments.⁷¹ Very often, a scaling factor is applied to account for the offset when one directly compares the vibrational spectra between simulation and experiment.⁷²⁻⁷⁷

5.3.1.2 Rutile (011), TiO₂-B (100), and TiO₂-B (001) surfaces

For the FAWL at the rutile (011) surface, the result in Figure 21(b) demonstrates that the O-H bonds have two peaks at about 3660 and 3760 cm⁻¹. Compared with bulk water, the two modes have a red shift of 30 cm⁻¹ and a blue shift of 10 cm⁻¹, respectively. When it comes to the TiO₂-B (100) surface, two peaks around 3635 and 3710 cm⁻¹ are the characteristic O-H vibration modes, displaying significant red shifts of 55 cm⁻¹ and 40 cm⁻¹, respectively. It is worth noting that the splitting peak at 3760 cm⁻¹ is from the dangling O-H bonds of water. Lastly, for the FAWL at the TiO₂-B (001) surface, the O-H bond vibration modes are close to that of bulk water except for a small red shift around the 3680 cm⁻¹ mode.

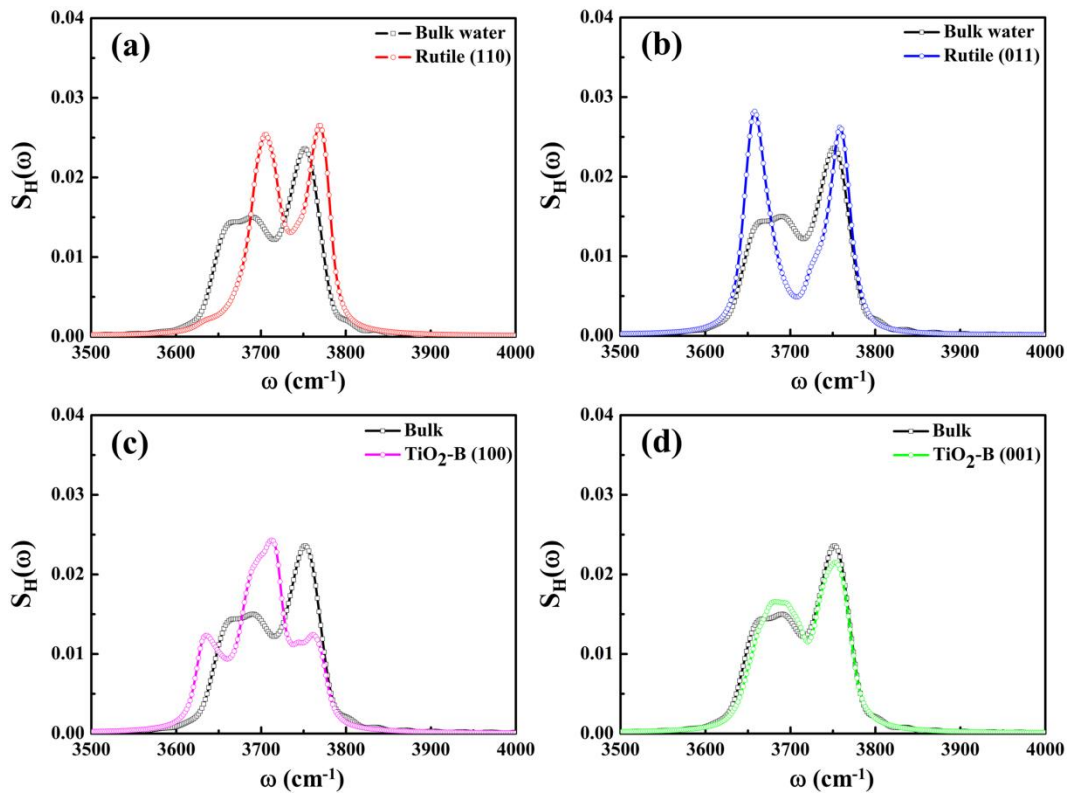


Figure 21. Fourier transformation vibrational spectra analysis of the hydrogen atoms of FAWL at (a) Rutile (110), (b) Rutile (011), (c) TiO₂-B (100), and (d) TiO₂-B (001) surfaces. For comparison, the result from pure water is also shown.

5.3.4 Hydrogen Bond Network of Adsorbed Water

It has been reported that the vibrational spectra modes of water are correlated with the HB network and its dynamic properties.^{64, 78-80} In this work, the HB of water from the FAWL is calculated based on the geometry criteria:^{81, 82}

$$R^{OO} < R_c^{OO} \quad \text{and} \quad \theta^{OOH} < \theta_c^{OOH} \quad (5-5)$$

where R^{OO} is the distance between two O atoms, one of which serves as the HB acceptor and the other one is regarded as HB donor, while θ^{OOH} represents the angle O...O-H. Similarly, R_c^{OO} and θ_c^{OOH} correspond the upper limit distance and angle for the HB formation, respectively. The two thresholds are 3.5 Å and 30°, respectively.⁸²

5.3.4.1 Rutile (110) Surface

For water molecules from the FAWL, they can form HBs from three groups of acceptor-donor: (A) FAWL-substrate, (B) FAWL-FAWL, and (C) FAWL-other water. The calculated average HB number for each type is listed in Table 8. For example, the results show that for the FAWL at the rutile (110) surface, the average HB number is negligible for type A (0.07) and type B (0.02), but it is 1.62 for type C. The percentage analysis in Figure 22 shows that for the FAWL at the rutile (110) surface, less than 7% of water molecules can form HBs with the substrate. Meanwhile, only about 2% of water molecules from the FAWL can form HBs each other. For type C HB, around 32% and 64% water molecules in the FAWL can form 1.0 HB or 2.0 HBs with other water molecules beyond the FAWL, which returns an averaged number of 1.62 for type C HB.

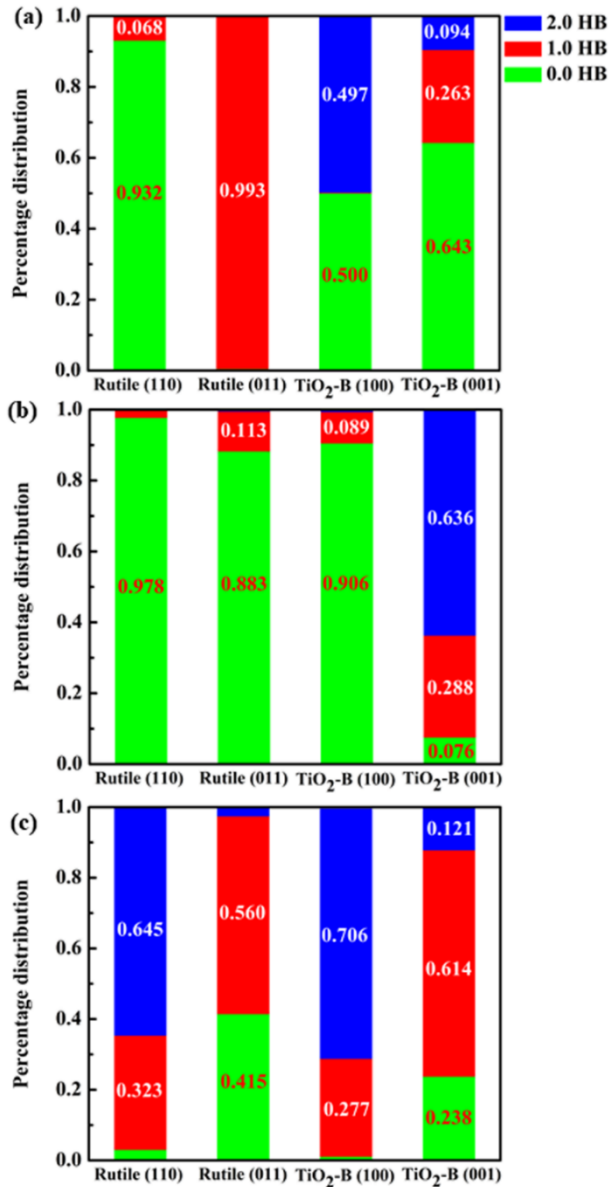


Figure 22. The analysis of averaged HBs between: (a) FAWL-substrate; (b) FAWL-FAWL; (c) FAWL-other water. Note: in the system of TiO₂-B (001), the percentage of more than 2.0 HB is included in the percentage of 2.0 HB for clarity.

Table 8. Average number of HBs of the FAWL with: (A) substrate, (B) FAWL, and (C) other water. The calculated HB number for bulk water is 3.58.

Surfaces	HB with Substrate (A)	HB within FAWL (B)	HB with other water (C)	Total HBs (A+B+C)
Rutile (110)	0.07	0.02	1.62	1.71
Rutile (011)	1.00	0.12	0.61	1.73
TiO ₂ -B (100)	1.00	0.10	1.70	2.80
TiO ₂ -B (001)	0.45	1.82	0.89	3.17
Bulk Water	3.58			

5.3.4.2 Rutile (011) Surface

For the average HB number at the rutile (011) surface, the results in Table 8 show that the values for type A, B, and C HB are 1.0, 0.12, and 0.61, respectively. Together with the distribution analysis in Figure 22, nearly all water molecules from the FAWL form 1.0 HB with the substrate surface. This result confirms the aforementioned water structure analysis, that is, each water molecule has one H atom pointing to the surface O_{2c} atoms, and the other H atoms are located away from the substrate. Furthermore, about 88% water molecules from the FAWL don't form any HB interaction with each other, and about 11.3% water molecules form 1.0 HB within the layer. For water molecules from different layers, about 41.5% water molecules from the FAWL cannot form any HB with other water molecules, and the other 56.0% water molecules form 1.0 HB with water molecules from outside of the FAWL.

5.3.4.3 TiO₂-B (100) Surface

For the average HB number on TiO₂-B (100) surface, it is 1.0 and 0.10 for type A and type B, respectively, which is similar to the result of the rutile (011) surface. As plotted in Figure 22(a),

for the FAWL at TiO₂-B (100) surface, 50% of water molecules cannot form HB with the substrate, but all the other 50% molecules form 2.0 HB with the surface O_{2c} atoms. Therefore, the averaged HB value for type A is 1.0. Together with the aforementioned configuration analysis, we conclude that the “H-up” water molecules do not form any HB with the surface, but the “H-down” water molecules can form exactly two HB with the O_{2c} atoms of the surface. In addition, according to Figure 22(b), we can see that over 90% water molecules of the FAWL cannot form any HB with each other, resulting in a negligible HB value for type B. For the HB between the FAWL and other water molecules, the results in Figure 22(c) show that 27.7% of water molecules of the FAWL can form 1.0 HB, while the other around 70.0 % will form 2.0 HBs. This suggests that over 27% of water molecules with the “H-up” configuration have dangling O-H bonds, resulting in the O-H vibration modes with a higher frequency around 3760 cm⁻¹.

5.3.4.4 TiO₂-B (001) Surface

Finally, for water at the TiO₂-B (001) surface, the average HBs are 0.45, 1.82 and 0.89 for type A, B, and C, respectively. This indicates that each water molecule has 3.17 HBs by average. This averaged HB is close to that of bulk water and is much higher than what are observed at other three surfaces. In particular, while the other three surfaces show a negligible type B HB, for the TiO₂-B (001) surface, the averaged type B HB is 1.82. Such a large value also explains the formation of HB clusters at the surface. To summarize, the dominating HBs are: type C for the rutile (110) surface; type A and C for both rutile (011) and TiO₂-B (100) surfaces, and type B and C for the TiO₂-B (001) surface.

5.3.5 Hydrogen Bond Dynamics of Adsorbed Water

The HB strength is also calculated by the continuous time correlation functions (TCFs) $S_{HB}(t)$, defined as^{81, 83, 84}

$$S_{HB}(t) = \frac{\langle h(0)h(t) \rangle}{\langle h(t) \rangle} \quad (5 - 6)$$

where the population variable of $h(t)$ is unity when a tagged HB pair is maintained for the time period from 0 to t , otherwise zero. Figure 23 shows the calculated $S_{HB}(t)$ variations for type A and C HBs, with the result for type B of the $\text{TiO}_2\text{-B}$ (001) shown as the inset in Figure 23(a). For the type C HBs of the rutile (110) surface, the $S_{HB}(t)$ curve decays slightly faster than that of bulk water, indicating a relatively weaker HB strength. This agrees with the blue shift of OH stretching modes shown in Figure 21(a). For the type A HB of the rutile (011) surface, as illustrated in Figure 23(a), the $S_{HB}(t)$ curve decay significantly slower than that of bulk water, suggesting a stronger and more stable HB network. Regarding the type C HB of the rutile (011) surface, the $S_{HB}(t)$ curve decays quickly, suggesting a weak interaction between the FAWL and other water molecules. It is also worth noting that for the red and blue shifts of O-H stretching modes at the rutile (011) surface illustrated in Figure 21(b), the former is from the enhanced interaction of type A HB, and the latter is due to the decreased strength of type C HBs.

Similarly, for type A and C HBs of the $\text{TiO}_2\text{-B}$ (100) surface, the $S_{HB}(t)$ decays slower than the bulk water, which further confirms that both types A and C HB strengths are enhanced. This enhanced HB strength results in the red shift of the OH stretching modes as shown in Figure 21(c). Additionally, for the type C HB on $\text{TiO}_2\text{-B}$ (001) surface, the $S_{HB}(t)$ curve decays faster than that of the bulk water, demonstrating a slight strength decrease of the type C HBs. For the type B HB on this surface, the $S_{HB}(t)$ curve, as shown in the inset of Figure 23(a), decays significantly slower with respect to the bulk water, suggesting a greatly enhanced strength of the type B HBs. Overall,

the HB strength for the FAWL on TiO₂-B (001) surface is enhanced and this is why a blue shift of the OH stretching modes is observed, see Figure 21(d).

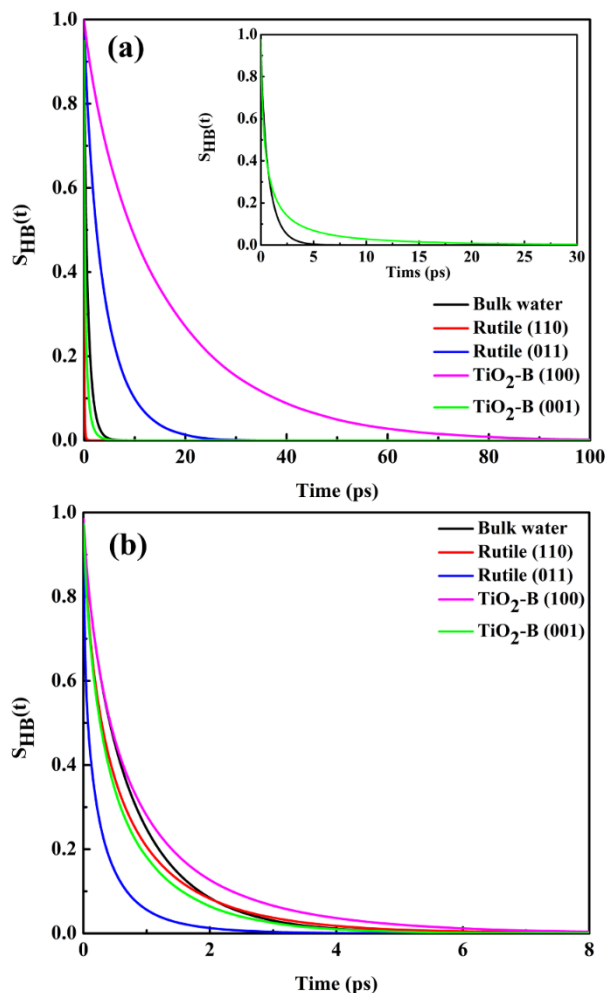


Figure 23. Continuous time correlation function $S_{HB}(t)$ for HB network between (a) FAWL-substrate and (b) FAWL-other water on different TiO₂ surfaces. The inset in (a) is the $S_{HB}(t)$ for HB network between FAWL-FAWL on TiO₂-B (001) surface. For comparison, the result from bulk water is also shown.

5.4 Conclusions

In this work, classical MD simulations have been carried out to systematically investigate the properties of FAWL at four TiO₂ surfaces. Water density profile, water angular orientation

distribution, the HB structural and dynamic properties and the vibrational spectra have been calculated and discussed. Our calculation results show that different water structures can be formed near the TiO₂ surfaces: (a) rutile (110), O_w atoms atop the Ti_{5c} sites and two H atoms facing away from the surface; (b) rutile (011), water molecules lean on the surface with one H atoms directing to the surface O_{2c} atoms and the other one pointing towards to bulk water; (c) TiO₂-B (100), water forms two configurations, “H-up” and “H-down”. The “H-up” configuration has the O_w atoms atop the Ti_{5c} sites with two H atoms pointing to bulk water. The “H-down” configuration has both H atoms point to the surface O_{2c} sites; (d) TiO₂-B (001), water has a random distribution, yet, the in-layer HBs promote the formation of small water clusters near the surface.

Based on the structural and orientational information of the FAWL, the vibrational spectra, the HB network and lifetime are also analyzed. Both blue and red shifts of OH vibration modes have been observed for the rutile (011) surface. The blue and red shifts have been identified for the rutile (110) and TiO₂-B (100) surfaces, respectively. The slightly red shift from the TiO₂-B (001) surface is probably due to the HB assisted clusters formed in the FAWL. The HBs are classified as three types: type A, the ones from the FAWL-substrate interaction; type B, the ones from the FAWL-FAWL interactions; type C, the ones from the FAWL-other water interactions. The calculations reveal the dominating HBs for the studied TiO₂ surfaces: rutile (110), type C; rutile (011), type A and C; TiO₂-B (100), type A and C; TiO₂-B (001), type B and C. The vibrational spectra, the HB network strength and the HB lifetime are correlated; a significant red shift of the vibrational spectra suggests an enhanced HB network, which also results in a much longer HB lifetime. For the studied surfaces, the TiO₂-B (100) has a most stable HB network and the HB lifetime is also the longest. The relationship between the vibrational spectra and interfacial

structures and dynamics provides a new perspective of using vibrational spectra experiments to qualitatively characterize the HB properties at the water/TiO₂ interface.

5.5 References

1. Bai, J.; Zhou, B. X. Titanium Dioxide Nanomaterials for Sensor Applications. *Chem. Rev.* **2014**, *114*, 10131.
2. Bourikas, K.; Kordulis, C.; Lycourghiotis, A. Titanium Dioxide (Anatase and Rutile): Surface Chemistry, Liquid-Solid Interface Chemistry, and Scientific Synthesis of Supported Catalysts. *Chem. Rev.* **2014**, *114*, 9754.
3. Kapilashrami, M.; Zhang, Y. F.; Liu, Y. S.; Hagfeldt, A.; Guo, J. Probing the Optical Property and Electronic Structure of TiO₂ Nanomaterials for Renewable Energy Applications. *Chem. Rev.* **2014**, *114*, 9662.
4. Rajh, T.; Dimitrijevic, N. M.; Bissonnette, M.; Koritarov, T.; Konda, V. Titanium Dioxide in the Service of the Biomedical Revolution. *Chem. Rev.* **2014**, *114*, 10177.
5. Fujishima, A.; Honda, K. Electrochemical Photolysis of Water at a Semiconductor Electrode. *Nature* **1972**, *238*, 37.
6. Sun, C.; Liu, L.M.; Selloni, A.; Lu, G. Q.; Smith, S. C. Titania-Water Interactions: A Review of Theoretical Studies. *J. Mater. Chem.* **2010**, *20*, 10319.
7. Mu, R.; Zhao, Z. J.; Dohnalek, Z.; Gong, J. Structural Motifs of Water on Metal Oxide Surfaces. *Chem. Soc. Rev.* **2017**, *46*, 1785.
8. De Angelis, F.; Di Valentin, C.; Fantacci, S.; Vittadini, A.; Selloni, A. Theoretical Studies on Anatase and Less Common TiO₂ Phases: Bulk, Surfaces, and Nanomaterials. *Chem. Rev.* **2014**, *114*, 9708.

9. Hugenschmidt, M. B.; Gamble, L.; Campbell, C. T. The Interaction of H₂O with a TiO₂ (110) Surface. *Surf. Sci.* **1994**, *302*, 329.
10. Wang, Z. T.; Wang, Y. G.; Mu, R.; Yoon, Y.; Dahal, A.; Schenter, G. K.; Glezakou, V. A.; Rousseau, R.; Lyubinetsky, I.; Dohnalek, Z. Probing Equilibrium of Molecular and Deprotonated Water on TiO₂(110). *Proc. Natl. Acad. Sci. U. S. A.* **2017**, *114*, 1801.
11. Geng, Z.; Chen, X.; Yang, W.; Guo, Q.; Xu, C.; Dai, D.; Yang, X. Highly Efficient Water Dissociation on Anatase TiO₂(101). *J. Phys. Chem. C* **2016**, *120*, 26807.
12. Matthiesen, J.; Hansen, J. O.; Wendt, S.; Lira, E.; Schaub, R.; Laegsgaard, E.; Besenbacher, F.; Hammer, B. Formation and Diffusion of Water Dimers on Rutile TiO₂(110). *Phys. Rev. Lett.* **2009**, *102*, 226101.
13. Hussain, H.; Tocci, G.; Woolcot, T.; Torrelles, X.; Pang, C. L.; Humphrey, D. S.; Yim, C. M.; Grinter, D. C.; Cabailh, G.; Bikondoa, O.; Lindsay, R.; Zegenhagen, J.; Michaelides, A.; Thornton, G. Structure of a Model TiO₂ Photocatalytic Interface. *Nat. Mater.* **2017**, *16*, 461.
14. Serrano, G.; Bonanni, B.; Di Giovannantonio, M.; Kosmala, T.; Schmid, M.; Diebold, U.; Di Carlo, A.; Cheng, J.; VandeVondele, J.; Wandelt, K.; Goletti, C. Molecular Ordering at the Interface Between Liquid Water and Rutile TiO₂(110). *Adv. Mater. Interfaces* **2015**, *2*, 1500246.
15. Huang, L. L.; Gubbins, K. E.; Li, L. C.; Lu, X. H. Water on Titanium Dioxide Surface: A Revisiting by Reactive Molecular Dynamics Simulations. *Langmuir* **2014**, *30*, 14832.
16. Zhao, Z.; Li, Z.; Zou, Z. Structure and Properties of Water on the Anatase TiO₂(101) Surface: From Single-Molecule Adsorption to Interface Formation. *J. Phys. Chem. C* **2012**, *116*, 11054.
17. Mattioli, G.; Filippone, F.; Caminiti, R.; Bonapasta, A. A. Short Hydrogen Bonds at the Water-TiO₂ (Anatase) Interface. *J. Phys. Chem. C* **2008**, *112*, 13579.

18. Skelton, A. A.; Walsh, T. R. Interaction of Liquid Water with the Rutile TiO₂(110) Surface. *Mol. Simulat.* **2007**, *33*, 379.
19. Kavathekar, R. S.; Dev, P.; English, N. J.; MacElroy, J. M. D. Molecular Dynamics Study of Water in Contact with the TiO₂ rutile-110, 100, 101, 001 and anatase-101, 001 surface. *Mol. Phys.* **2011**, *109*, 1649.
20. Hammer, B.; Wendt, S.; Besenbacher, F. Water Adsorption on TiO₂. *Top. Catal.* **2010**, *53*, 423.
21. Sebbari, K.; Domain, C.; Roques, J.; Perron, H.; Simoni, E.; Catalette, H. Investigation of Hydrogen Bonds and Temperature Effects on the Water Monolayer Adsorption on Rutile TiO₂ (110) by First-Principles Molecular Dynamics Simulations. *Surf. Sci.* **2011**, *605*, 1275.
22. English, N. J.; Kavathekar, R. S.; MacElroy, J. M. D. Hydrogen Bond Dynamical Properties of Adsorbed Liquid Water Monolayers with Various TiO₂ Interfaces. *Mol. Phys.* **2012**, *110*, 2919.
23. Bahramian, A. Molecular Interactions Insights underlying Temperature-Dependent Structure of Water Molecules on TiO₂ Nanostructured Film: A Computational Study using Reactive and Non-reactive Force Fields. *Fluid Phase Equilib.* **2017**, *438*, 53.
24. Kavathekar, R. S.; English, N. J.; MacElroy, J. M. D. Spatial Distribution of Adsorbed Water Layers at the TiO₂ Rutile and Anatase Interfaces. *Chem. Phys. Lett.* **2012**, *554*, 102.
25. Hamideh Babazadeh, K.; Foroutan, M. Water Distribution in Layers of an Aqueous Film on the Titanium Dioxide Surface: A Molecular Dynamic Simulation Approach. *J. Mol. Liq.* **2017**, *244*, 291.
26. Hosseinpour, S.; Tang, F.; Wang, F.; Livingstone, R. A.; Schlegel, S. J.; Ohto, T.; Bonn, M.; Nagata, Y.; Backus, E. H. G. Chemisorbed and Physisorbed Water at the TiO₂/Water Interface. *J. Phys. Chem. Lett.* **2017**, *8*, 2195.

27. Yang, W.; Wei, D.; Jin, X.; Xu, C.; Geng, Z.; Guo, Q.; Ma, Z.; Dai, D.; Fan, H.; Yang, X. Effect of the Hydrogen Bond in Photoinduced Water Dissociation: A Double-Edged Sword. *J. Phys. Chem. Lett.* **2016**, *7*, 603.
28. Ferst, A. R.; Shi, J. P.; Knill-Jones, J.; Low, D. M.; Wilkinson, A. J.; Blow, D. M.; Brick, P. Carter, P.; Waye, M. M. Y.; Winter, G. Hydrogen Bonding and Biological Specificity Analysed by Protein Engineering. *Nature*, **1985**, *314*, 235.
29. Shan, S.; Loh, S.; Herschlag, D. The Energetics of Hydrogen Bonds in Model Systems: Implications for Enzymatic Catalysis. *Science* **1996**, *272*, 97.
30. Briggs, M. S.; Roder, H. Early Hydrogen-Bonding Events in the Folding Reaction of Ubiquitin. *Proc. Natl. Acad. Sci. U. S. A.* **1992**, *89*, 2017.
31. Kim, P. S.; Baldwin, R. L. Intermediates in the Folding Reactions of Small Proteins. *Annu. Rev. Biochem.* **1990**, *59*, 631.
32. Liu, Y.; Hu, C.; Comotti, A.; Ward, M. D. Supramolecular Archimedean Cages Assembled with 72 Hydrogen Bonds. *Science* **2011**, *333*, 436.
33. MacGillivray, L. R.; Atwood, J. L. A Chiral Spherical Molecular Assembly Held Together by 60 Hydrogen Bonds. *Nature* **1997**, *389*, 469.
34. Tuckerman, M. E.; Marx, D.; Klein, M. L.; Parrinello, M. On the Quantum Nature of the Shared Proton in Hydrogen Bonds. *Science* **1997**, *275*, 817.
35. Muller-Dethlefs, K.; Hobza, P. Noncovalent Interactions: A Challenge for Experiment and Theory. *Chem. Rev.* **2000**, *100*, 143.
36. Steiner, T. The Hydrogen Bond in the Solid State. *Angew. Chem. Int. Ed.* **2002**, *41*, 48–76.
37. Lee, J.; Sorescu, D. C.; Deng, X.; Jordan, K. D. Water Chain Formation on TiO₂(110). *J. Phys. Chem. Lett.* **2013**, *4*, 53.

38. Kimmel, G. A.; Baer, M.; Petrik, N. G.; VandeVondele, J.; Rousseau, R.; Mundy, C. J. Polarization- and Azimuth-Resolved Infrared Spectroscopy of Water on TiO₂(110): Anisotropy and the Hydrogen-Bonding Network. *J. Phys. Chem. Lett.* **2012**, *3*, 778.
39. Mamontov, E.; Vlcek, L.; Wesolowski, D. J.; Cummings, P. T.; Wang, W.; Anovitz, L. M. Rosenqvist, J.; Brown, C. M.; Sakai, V. G. Dynamics and Structure of Hydration Water on Rutile and Cassiterite Nanopowders Studied by Quasielastic Neutron Scattering and Molecular Dynamics Simulations. *J. Phys. Chem. C* **2007**, *111*, 4328.
40. Ohto, T.; Mishra, A.; Yoshimune, S.; Nakamura, H.; Bonn, M.; Nagata, Y. Influence of Surface Polarity on Water Dynamics at the Water/Rutile TiO₂(110) Interface. *J. Phys. Condens. Matter.* **2014**, *26*, 244102.
41. Cromer, D. T.; Herrington, K. The Structure of Anatase and Rutile. *J. Am. Chem. Soc.* 1955, *77*, 4708.
42. Marchand, R.; Borhan, L.; Tournoux, M. TiO₂(B) a New Form of Titanium Dioxide and the Potassium Octatitanate K₂Ti₈O₁₇. *Mat. Res. Bull.* 1980, *15*, 1129.
43. Yuet, P. K.; Blankshtein, D. Molecular Dynamics Simulation Study of Water Surfaces: Comparison of Flexible Water Models. *J. Phys. Chem. B* **2010**, *114*, 13786.
44. Bandura, A. V.; Kubicki, J. D. Derivation of Force Field Parameters for TiO₂-H₂O Systems from Ab Initio Calculations. *J. Phys. Chem. B* **2003**, *107*, 11072.
45. LAMMPS; <http://lammps.sandia.gov>.
46. Hockney, R. W.; Eastwood, J. W. Computer Simulation Using Particles, 2nd ed.; IOP: Bristol, U.K., 1988.
47. Henderson, M. A. The Interaction of Water with Solid Surfaces: Fundamental Aspects Revisited. *Surf. Sci. Rep.* **2002**, *46*, 1.

48. Hodgson, A.; Haq, S. Water Adsorption and the Wetting of Metal Surfaces. *Surf. Sci. Rep.* **2009**, *64*, 381.
49. Chabal, Y. J. Surface Infrared-Spectroscopy. *Surf. Sci. Rep.* **1988**, *8*, 211.
50. Feibelman, P. J.; Kimmel, G. A.; Smith, R. S.; Petrik, N. G.; Zubkov, T.; Kay, B. D. A Unique Vibrational Signature of Rotated Water Monolayers on Pt(111): Predicted and Observed. *J. Chem. Phys.* **2011**, *134*, 204702.
51. Lindan, P. J. D.; Harrison, N. M.; Holender, J. M.; Gillan, M. J. First-Principles Molecular Dynamics Simulation of Water Dissociation on TiO₂(110). *Chem. Phys. Lett.* **1996**, *261*, 246–252.
52. Kumar, N.; Neogi, S.; Kent, P. R. C.; Bandura, A. V.; Kubicki, J. D.; Wesolowski, D. J.; Cole, D.; Sofo, J. O. Hydrogen Bonds and Vibrations of Water on (110) Rutile. *J. Phys. Chem. C* **2009**, *113*, 13732.
53. English, N. J., Dynamical Properties of Physically Adsorbed Water Molecules at the TiO₂ Rutile-(110) Surface. *Chem. Phys. Lett.* **2013**, *583*, 125.
54. Lun Pang, C.; Lindsay, R.; Thornton, G. Chemical Reactions on Rutile TiO₂(110). *Chem. Soc. Rev.* **2008**, *37*, 2328.
55. Dahal, A.; Dohnálek, Z. Formation of Metastable Water Chains on Anatase TiO₂(101). *J. Phys. Chem. C* **2017**, *121*, 20413.
56. Brookes, I. M.; Muryn, C. A.; Thornton, G., Imaging Water Dissociation on TiO₂(110). *Phys. Rev. Lett.* **2001**, *87*, 266103.
57. Tilocca, A.; Selloni, A. Vertical and Lateral Order in Adsorbed Water Layers on Anatase TiO₂(101). *Langmuir* **2004**, *20*, 8379.

58. Beck, T. J.; Klust, A.; Batzill, M.; Diebold, U.; Di Valentin, C.; Tilocca, A.; Selloni, A. Mixed Dissociated/Molecular Monolayer of Water on the TiO₂(011)-(2×1) Surface. *Surf. Sci.* **2005**, *591*, L267.
59. Di Valentin, C.; Tilocca, A.; Selloni, A.; Beck, T. J.; Klust, A.; Batzill, M.; Losovyj, Y.; Diebold, U. Adsorption of Water on Reconstructed Rutile TiO₂(011)-(2×1):Ti=O Double Bonds and Surface Reactivity. *J. Am. Chem. Soc.* **2005**, *127*, 9895.
60. Vittadini, A.; Casarin, M.; Selloni, A. Structure and Stability of TiO₂-B Surfaces: A Density Functional Study. *J. Phys. Chem. C* **2009**, *113*, 18973.
61. Vittadini, A.; Casarin, M.; Selloni, A. Hydroxylation of TiO₂-B: Insights from Density Functional Calculations. *J. Mater. Chem.* **2010**, *20*, 5871.
62. Deshmukh, S. A.; Sankaranarayanan, S. K., Atomic Scale Characterization of Interfacial Water near an Oxide Surface using Molecular Dynamics Simulations. *Phys. Chem. Chem. Phys.* **2012**, *14*, 15593.
63. Martí, J.; Padro, J. A.; Guàrdia, E. Molecular Dynamics Simulation of Liquid Water along the Coexistence Curve: Hydrogen Bonds and Vibrational spectra. *J. Chem. Phys.* **1996**, *105*, 639.
64. Yang, Z.; Li, Y.; Zhou, G.; Chen, X.; Tao, D.; Hu, N. Molecular Dynamics Simulations of Hydrogen Bond Dynamics and Far-Infrared Spectra of Hydration Water Molecules around the Mixed Monolayer-Protected Au Nanoparticle. *J. Phys. Chem. C* **2015**, *119*, 1768.
65. Tay, K.; Bresme, F. Hydrogen Bond Structure and Vibrational Spectrum of Water at a Passivated Metal Nanoparticle. *J. Mater. Chem.* **2006**, *16*, 1956.
66. Xantheas, S. S.; Dunning, T. H. Ab Initio Studies of Cyclic Water Clusters (H₂O)_n, n=1-6. I. Optimal Structures and Vibrational Spectra. *J. Chem. Phys.* **1993**, *99*, 8774.

67. Fredin, L.; Nelander, B.; Ribbegård, G. Infrared Spectrum of the Water Dimer in Solid Nitrogen. I. Assignment and Force Constant Calculations. *J. Chem. Phys.* **1977**, *66*, 4065.
68. Levchenko, A. A.; Kolesnikov, A. I.; Ross, N. L.; Woodfield, B. F.; Li, G.; Navrotsky, A.; Boerio-Goates, J. Dynamics of Water Confined on a TiO₂ (Anatase) Surface. *J. Phys. Chem. A* **2007**, *111*, 12584.
69. Spencer, E. R.; Levchenko, A. A.; Ross, N. L.; Kolesnikov, A. I.; Boerio-Goates, J.; Woodfield, B. F.; Navrotsky, A.; Li, G. Inelastic Neutron Scattering Study of Confined Surface Water on Rutile Nanoparticles. *J. Phys. Chem. A* **2009**, *113*, 2796.
70. Kavathekar, R. S.; English, N. J.; MacElroy, J. M. D. Study of Translational, Librational and Intra-Molecular Motion of Adsorbed Liquid Water Monolayers at Various TiO₂ Interfaces. *Mol. Phys.* **2011**, *109*, 2645.
71. Hehre, W. J.; Radom, L.; Schleyer, P. V. R.; Pople, J. A. *Ab Initio Molecular Orbital Theory*; Wiley: New York, 1986.
72. Alecu, I. M.; Zheng, J. J.; Zhao, Y.; Truhlar, D. G. Computational Thermochemistry: Scale Factor Database and Scale Factors for Vibrational Frequencies Obtained from Electronic Model Chemistries. *J. Chem. Theory Comput.* **2010**, *6*, 2872.
73. Merrick, J. P.; Moran, D.; Radom, L. An Evaluation of Harmonic Vibrational Frequency Scale Factors. *J. Phys. Chem. A* **2007**, *111*, 11683.
74. Andersson, M. P.; Uvdal, P. New Scale Factors for Harmonic Vibrational Frequencies Using the B3LYP Density Functional Method with the Triple- ζ Basis Set 6-311+G(d,p). *J. Phys. Chem. A* **2005**, *109*, 2937.
75. Rauhut, G.; Pulay, P. Transferable Scaling Factors for Density Functional Derived Vibrational Force Fields. *J. Phys. Chem.* **1995**, *99*, 3093.

76. El-Azhary, A. A.; Suter, H. U. Comparison between Optimized Geometries and Vibrational Frequencies Calculated by the DFT Methods. *J. Phys. Chem.* **1996**, *100*, 15056.
77. Scott, A. P.; Radom, L. Harmonic Vibrational Frequencies: An Evaluation of Hartree-Fock, Møller-Plesset, Quadratic Configuration Interaction, Density Functional Theory, and Semiempirical Scale Factors. *J. Phys. Chem.* **1996**, *100*, 16502.
78. Zhou, G. B.; Li, Y. Z.; Yang, Z.; Fu, F. J.; Huang, Y. P.; Wan, Z.; Li, L.; Chen, X. S.; Hu, N.; Huang, L. L. Structural Properties and Vibrational Spectra of Ethylammonium Nitrate Ionic Liquid Confined in Single-Walled Carbon Nanotubes. *J. Phys. Chem. C* **2016**, *120*, 5033.
79. Byl, O.; Liu, J. C.; Wang, Y.; Yim, W. L.; Johnson, J. K.; Yates, J. T., Jr. Unusual Hydrogen Bonding in Water-Filled Carbon Nanotubes. *J. Am. Chem. Soc.* **2006** *128*, 12090.
80. Weinwurm, M.; Dellago, C., Vibrational Spectroscopy of Water in Narrow Nanopores. *J. Phys. Chem. B* **2011**, *115*, 5268.
81. Luzar, A.; Chandler, D. Hydrogen-Bond Kinetics in Liquid Water. *Nature*, **1996**, *379*, 55.
82. Stillinger, F. H. Water Revisited. *Science* **1980**, *209*, 451.
83. Zhao, W.; Leroy, F.; Heggen, B.; Zahn, S.; Kirchner, B.; Balasubramanian, S.; Müller-Plathe, F. Are There Stable Ion-Pairs in Room-Temperature Ionic Liquids? Molecular Dynamics Simulations of 1-n-Butyl-3-Methylimidazolium Hexafluorophosphate. *J. Am. Chem. Soc.* **2009**, *131*, 15825.
84. Karimi-Varzaneh, H. A.; Carbone, P.; Muller-Plathe, F. Hydrogen Bonding and Dynamic Crossover in Polyamide-66: A Molecular Dynamics Simulation Study. *Macromolecules* **2008**, *41*, 7211.

Chapter 6: Interfacial Potassium Induced Enhanced Raman

Spectroscopy for Single-Crystal TiO₂ Nanowhisker*

6.1 Introduction

Surface-enhanced Raman spectroscopy (SERS) is one of the most sensitive spectroscopic techniques to detect molecules that have a strong Raman response at a single-molecule resolution.¹ In recent years, TiO₂ semiconductor-based SERS has attracted much attention due to the advantages of low cost, good stability and excellent reproducibility.²⁻⁴ TiO₂ SERS performance is mainly tuned via the preparation protocol where element doping (hydrogen and oxygen), morphology manipulation and band structure engineering are beneficial. Compared with traditional coinage metal substrates such as gold, silver and copper, TiO₂ photocatalytic properties enable an environment-friendly removal of adsorbed molecules and a reuse of the SERS substrate.⁵

Despite the promise, semiconductor-based SERS substrates are generally limited by the inferior enhancement factor (EF), an index of how sensitive the detection is. The theoretical maximum EF for semiconductor-based SERS,⁴ based on charge-transfer (CT) mechanism, has been estimated to be around 10^6 . However, reported experimental EF values for TiO₂ substrates are only in the range of $10\sim 10^3$. Generally, there are two options to improve the SERS performance. The first one is to change the semiconductor morphology and thus enhance the interactions between the laser and the substrate. Under this guideline, Alessandri synthesized TiO₂ shell-based spherical resonators and reported a remarkable Raman scattering enhancement.⁶ The improvement is ascribed to the synergistic effects of high refractive index of TiO₂ shell layer and multiple light scattering through spherical geometries. Similarly, Zhang and co-workers used a sol-gel method and prepared TiO₂ inverse opal photonic microarrays.⁷ They reported that the morphology change

*Pan, F.; Zhou, G.; Huang, L.; Li, W.; Lin, M.; Liu, C. Interfacial Potassium Induced Enhanced Raman Spectroscopy 133 for Single-Crystal TiO₂ Nanowhisker. *Chin. J. Chem. Eng.* 2020, DOI: 10.1016/j.cjche.2019.10.003

results in the photonic band gap change, which in return promotes multiple light scattering and the resulted EF is about 10^4 . Recently, we adopted a two-step anodic oxidation process and prepared TiO₂ nanofoam–nanotube array,⁸ which shows a remarkable Raman scattering enhancement for methylene blue (EF = 2.3×10^5). The second option is to manipulate interactions between the substrate and adsorbed molecules. For example, Cong and co-workers engineered oxygen vacancy at tungsten oxide nanowire surfaces.⁹ It was observed that the new interfacial oxygen vacancies can enrich tungsten oxide surface states, strengthen adsorbent-adsorbate interactions, and eventually produce an improved EF value of 3.4×10^5 . Inspired by Cong's work, hydrogen or oxygen doping has been adopted to treat other semiconductors.⁵ It is generally accepted that quasi-amorphous interfacial thin layers and hydrogen or oxygen doping effectively facilitate charge transfer, enhance vibrational scattering of adsorbed molecules and improve the SERS performance.

It is worth pointing out that defect engineering is a double-edged sword. A poorly designed defective interface can severely degrade SERS performance. For example, it was reported that the excess amorphous structure at interface can decrease the refractive index, which could weaken the interactions between the SERS substrate and the laser.⁴ Also, interfacial defects can induce the transformation and re-combination of electron/hole pairs, which will degrade SERS performance.¹⁰ For instance, Zhao and co-workers investigated the crystallinity effect of anatase TiO₂ nanoparticles on SERS performance.¹¹ They concluded that both high degree of crystallinity and high concentration of surface defects are critical for a superior SERS performance. However, the challenge is that the two factors do not come together very easily for TiO₂ materials: using a high-temperature treatment (normally above 600 °C) to improve anatase TiO₂ crystallinity, one can easily witness the intrinsic phase transformation from anatase to rutile TiO₂. The as-synthesized TiO₂ substrate has an inferior SERS performance.

In this work, we report a new semiconductor SERS substrate-TiO₂ nanowhisker with high crystallinity and high thermal stability. The single anatase crystal phase remains intact up to 900 °C, which is mainly due to the interfacial potassium. In addition, potassium binds strongly with TiO₂ substrate, producing a negatively charged interface for Raman scattering, as well as altering the band gap of anatase TiO₂. All three factors, namely, the single-phase crystallinity, the negatively charged interface and the reduced band gap, synergistically enable the synthesized anatase TiO₂ nanowhisker to be a supreme SERS substrate, with a maximum EF 4.96×10^6 . The significance of this work is two-fold: the report of a new SERS performance record from TiO₂ semiconductor, and the exploration of interfacial potassium doping effect. We anticipate other alkali elements can also assist engineering TiO₂ materials to achieve high crystallinity, high thermo stability and high interaction selectivity.

6.2 Experimental

6.2.1 Materials

Metatitanic acid (TiO₂·nH₂O) was from Nanjing oil chemicals Co., Ltd., China. Potassium carbonate (K₂CO₃) was from Shanghai chemical reagent factory. Methylene blue (MB) was purchased from Tianjin Chemical Reagent Research Institute Co., Ltd. All chemicals were of analytical grade and used as received. Deionized water was used in all experiments.

6.2.2 TiO₂ nanowhisker synthesis

TiO₂ nanowhisker was synthesized by a two-step calcination and ion exchange process, as illustrated in Figure 24.¹² Briefly, metatitanic acid (TiO₂·nH₂O) and potassium carbonate were mixed with a 1.9 molar ratio. The mixture was then calcined in the muffle furnace at 820 °C for 6 hrs. After that, the as-obtained potassium dititanate was washed with 0.1 M HCl and deionized

water, repeating for three times. Finally, the TiO₂ nanowhiskers were obtained by calcining the powders at different temperatures for 2 hrs. According to the temperature used in the final calcination step, obtained TiO₂ samples were named as Z700, Z800, Z900 and Z1000, respectively.

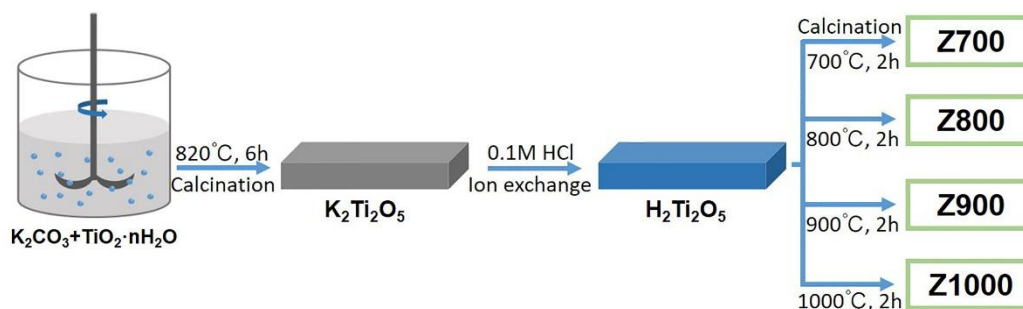


Figure 24. Schematic diagram of TiO₂ nanowhisker preparation.

6.2.3 Characterizations

The crystal structures of those samples were characterized by X-ray diffraction (XRD, Bruker, Model D8 with Cu K α excitation). In addition, the element composition and chemical states of studied samples were analysed by X-ray photoelectron spectrometer (XPS, Physical Electronics 5600). The UV-vis diffuse reflectance spectra (UV-vis DRS) was obtained by a UV-vis spectrometer (Perkin-Elmer Lambda 950) over a wavelength range of 300~800 nm. Surface morphologies were studied by using field-emission scanning electron microscope (FESEM, Hitachi S-4800) at 5 kV, 10 μ A. Surface charge of the samples were detected on the Zeta potential analyser (Malvern, ZS90). TEM images were obtained employing JEM-2010 UHR at 200 kV.

6.2.4 SERS measurement

The Raman signal of MB molecules adsorbed on TiO₂ nanowhiskers were obtained using the 514.5 nm laser excitation. Specifically, we obtain the 10⁻⁵ M MB ethanol solution by successively diluting a 10⁻³ M MB solution. Then 20 μ L of the 10⁻⁵ M MB ethanol solution was added to TiO₂

substrate, keeping the sample in the dark for 4 hrs to reach the adsorption equilibrium. Subsequently, the Raman spectra were collected via the high-resolution confocal Raman spectrometer (LabRAM HR-800) using a 50 × LWD objective lens for 10 s and 0.3 mW powers in all acquisitions. Each sample was collected at least 5 times from different locations of the sample.

6.3 Results and discussion

6.3.1 The characterization of TiO₂ nanowhisker

As shown in Figure 25a, scanning electron microscopy (SEM) images demonstrate that the four samples possess one-dimensional morphology. For the Z700 sample, the diameter is about 300 nm and the length is a few microns. When the temperature increases from 700 °C to 1000 °C, all studied samples shrink a little bit and their diameters increase slightly. This indicates that TiO₂ nanowhisker could melt partially at high temperatures. According to XRD characterizations in Figure 25b, Z700 and Z800 are pure anatase crystalline phase, while Z900 and Z1000 have a small portion of rutile crystalline phase. The content of rutile phase was estimated to be 2 mol % and 10 mol % for Z900 and Z1000, respectively.¹³

6.3.2 SERS properties of TiO₂ nanowhisker samples

Methylene blue (MB) was used as the probe molecule to examine the SERS performance of TiO₂ nanowhiskers. As shown in Figure 25c, the SERS enhancement factor (EF) is calculated at the characteristic peak of 1630 cm⁻¹, which is the aromatic C-C stretching vibration mode:⁹

$$EF = (I_{SERS}/N_{SERS})/(I_{bulk}/N_{bulk}) \quad (6-1)$$

where I_{SERS} and I_{bulk} refer to peak intensities of the SERS and non-SERS spectra, respectively. N_{SERS} and N_{bulk} correspond to the number of probe molecules in the laser area for the SERS and non-SERS measurements.

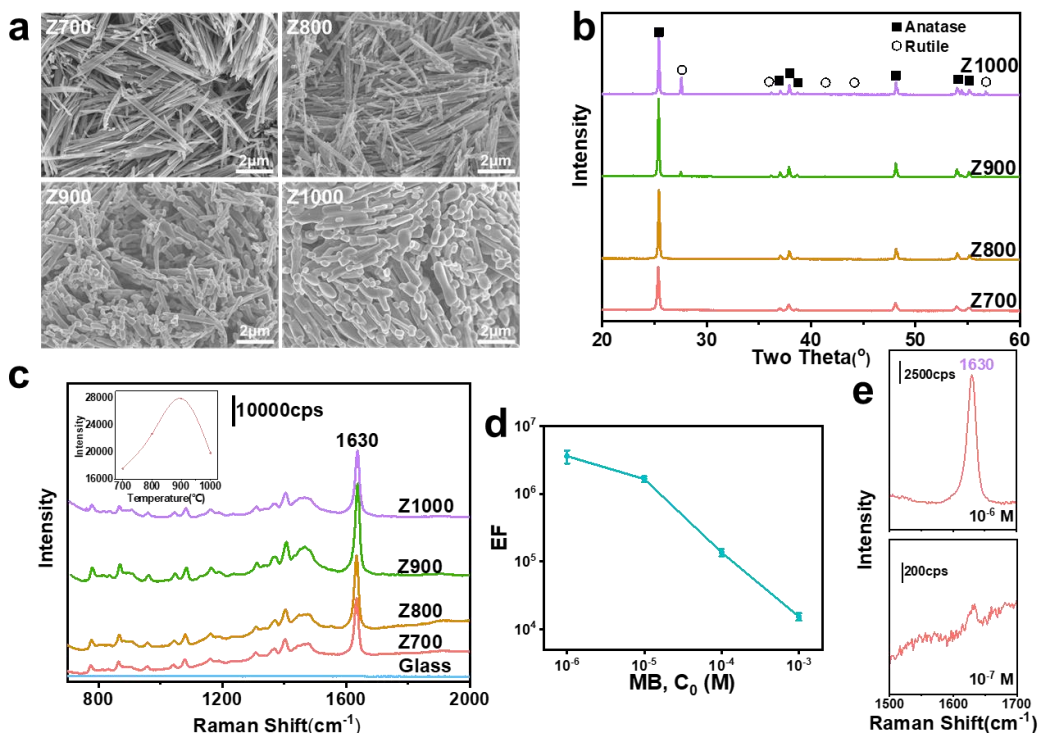


Figure 25. Morphology, crystal structure and SERS properties of four TiO₂ nanowhiser samples. (a) SEM images of Z700, Z800, Z900 and Z1000. (b) XRD pattern of four TiO₂ nanowhisers. (c) Raman spectra of the 10⁻⁵ M MB ethanol solution on four TiO₂ nanowhisers and bare glass (inset: the 1630 cm⁻¹ intensity of four nanowhisers). (d) Raman EFs obtained for MB on the Z900 sample, as a function of MB concentrations at the 1630 cm⁻¹ peak. (e) The detection limitation test of MB on the Z900 sample.

Significant SERS enhancements are observed for all four samples but there is almost no enhancement from the bare glass substrate. The Z900 sample shows the best SERS performance compared with other samples. It is probably because Z900 has a high crystallinity. It is worth pointing out that when the calcination temperature increases to 1000 °C, a significant phase

transformation will occur, from the anatase to rutile phase, which will result in a decrease of Raman detecting signal of MB molecules. The trend of anatase phase has a better SERS performance than the rutile phase is also reported by Zhao *et al.*¹⁴ As illustrated in Figure 25d, the calculated EF from the Z900 sample is 4.96×10^6 at the 10^{-6} M MB concentration, which is the best performance reported so far for TiO₂-based SERS substrates. In addition, the Z900 sample has an applicable detection of MB molecules even at a very dilute concentration of 10^{-7} M, see Figure 25e. Such detecting sensitivity is better than most reported results from semiconductor SERS substrates.

6.3.3 TiO₂ morphology and SERS performance

TiO₂ SERS substrates are traditionally polycrystalline materials, with the morphology of nanoparticles or mesoporous membranes. The TiO₂ nanowhisker synthesized in this work is a one-dimensional single crystal. A high crystallinity could improve the SERS performance. For example, Sun and co-workers reported that one-dimensional semiconductor materials with single crystal structures (such as nanowire and nanobelt), are excellent plasmonic waveguides to transfer Raman signals and realize remote SERS properties.¹⁵ Such signal transfer and remote Raman scattering are promising for Raman scattering enhancement. For the Z700 sample, as shown in Figures 26d and 26e, remote Raman scattering was also observed. In order to further validate the dominating contribution of the single crystal morphology, a new set of three samples has been prepared: Z700 nanowhisker with the one-dimensional morphology (Figure 26a); ZB700, a sample from ball-milling Z700, where the single crystallinity was destroyed (Figure 26b); T700, a mesoporous TiO₂ nanowhisker sample prepared with additional water vapor treatment during the Z700 sample preparation (Figure 26c). The key differences between three samples: ZB700 sample is composed of TiO₂ nanoparticles with irregular morphologies; T700 has the one-dimensional morphology,

similar to that of Z700. But T700 has a significant number of cavities at the surface. SERS performances of the three samples are compared in Figure 26f. First of all, the Raman scattering at low wavenumbers ($200\sim 800\text{ cm}^{-1}$) supports that all three samples are generally composed of TiO_2 anatase phase. However, the SERS performance from the three samples is obviously different: at the characteristic 1630 cm^{-1} peak, the EF has the order of $\text{T700} < \text{ZB700} < \text{Z700}$. It is important to point out that despite the one-dimensional morphology, the cavities of T700 significantly degrade the SERS performance. In summary, both the single crystallinity and the one-dimensional morphology are important for excellent SERS performance.

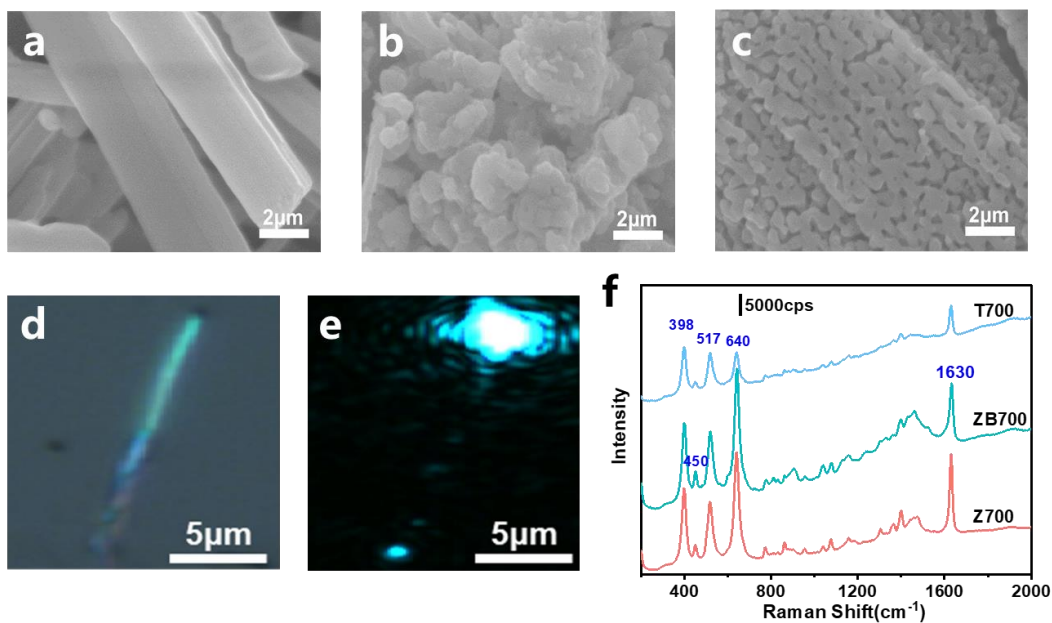


Figure 26. Morphology, Remote SERS and SERS performance of TiO_2 samples. SEM images of Z700 (a), ZB700 (b) and T700(c). The propagation of light along TiO_2 nanowhisker (Z700) under visible light (d) and laser (e). (f) Raman spectra of MB (10^{-5} M) adsorbed on T700, ZB 700 and Z700 samples.

6.3.4 Interfacial potassium and significant SERS improvement

Despite the performance degradation with respect to Z700 and ZB700, the T700 sample still has an EF of 4.13×10^5 , higher than other reported TiO₂ semiconductors. Since T700 possesses no single crystallinity nor perfect interfacial morphology, the excellent SERS performance is attributed by other factors. In literature, Zhao *et al.* reported that the photo absorption threshold to the 4-Mercaptobenzoic acid (4-MBA) adsorbed TiO₂ shows a blue-shift, compared with that of unmodified TiO₂. It is interpreted due to the interaction between adsorbed molecules and TiO₂ substrate.¹⁶ Similarly, Cong *et al.* reported their X-ray photoelectron spectroscopy (XPS) results that hydrogen treated W₁₈O₄₉ sample has an increased percentage of W⁵⁺, from 30.4 mol % (untreated, pristine W₁₈O₄₉) to 47.5 mol %.⁹ Obviously, there are more surface oxygen vacancies of the modified sample. Moreover, they determined UV-vis diffuse reflectance spectroscopy (DRS) spectra of R6G molecules deposited on W₁₈O₄₉ and reported a new band from the hybrid sample, an evidence of the charge transfer between R6G and W₁₈O₄₉.

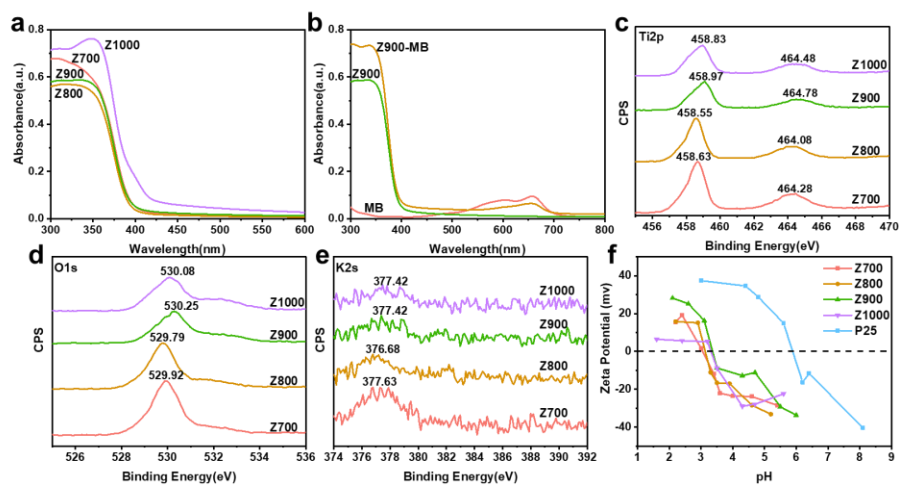


Figure 27. UV-vis DRS spectra of (a) TiO₂ nanowhiskers and (b) Z900 compared with pristine Z900 and MB. XPS spectra and binding energies of (c) titanium, (d) oxygen and (e) potassium. (f) Zeta potential as a function of pH: the comparison between four studied TiO₂ nanowhiskers and the commercial P25 sample.

Inspired by those studies, UV-vis DRS and XPS were performed in this work to further explore the enhancement mechanism of Raman scattering. As shown in Figure 27a, the photo absorption spectra for Z700, Z800 and Z900 samples are very similar to each other, with a same onset around 400 nm. Such result is in accordance with the photo absorption onset of TiO₂ anatase phase. A red shift of the absorption edge for Z1000 was observed, which is mainly due to the phase transformation and the resulted rutile phase. Ti2p and O1s peak positions of XPS spectra in Fig. 27c and 27d further confirmed that Z700 and Z800 are in the anatase phase, while Z900 and Z1000 have co-existing anatase and rutile phases.¹⁷ Moreover, as shown in Figure 27b, we compared UV-vis DRS spectra of MB molecule adsorbed on Z900 with that of pristine MB and Z900. No new band was observed from the spectra of MB modified Z900. In addition, the absorption edge of MB modified Z900 was same as that of pristine Z900 sample. Those results suggested that the excellent SERS performance of TiO₂ nanowhisker is not from defect states near TiO₂ conduction band.

The Zeta potential measurement in Figure 27f reveals that the point of zero charge (PZC) for studied TiO₂ nanowhiskers is in the range of pH 3.0 to 3.5, which is remarkably lower than that of the commercial P25 TiO₂ nanoparticles (~pH 6). Such PZC change indicates that the surface of TiO₂ nanowhisker is negatively charged, consequently interacting strongly with MB molecules through positive charged sites. The enhancement of electrostatic interactions is beneficial for SERS performance. We note that similar phenomenon has been reported on a Cu₂O SERS substrate.¹⁸ In order to validate the effect of electrostatic interactions, two molecules with opposite charges, namely, crystal violet (CV) (+) and methyl orange (MO) (-), were used to study their SERS performances on Z700 sample. As shown in Figure 28, the positively charged CV molecule shows a better SERS performance than the negatively charged MO molecule. In conclusion, we contributed Raman scattering enhancement observed in this work to synergistic effects: the

interfacial potassium induced charge transfer effect and the electrostatic adsorption effect due to surface negative charges of TiO₂ nanowhiskers.

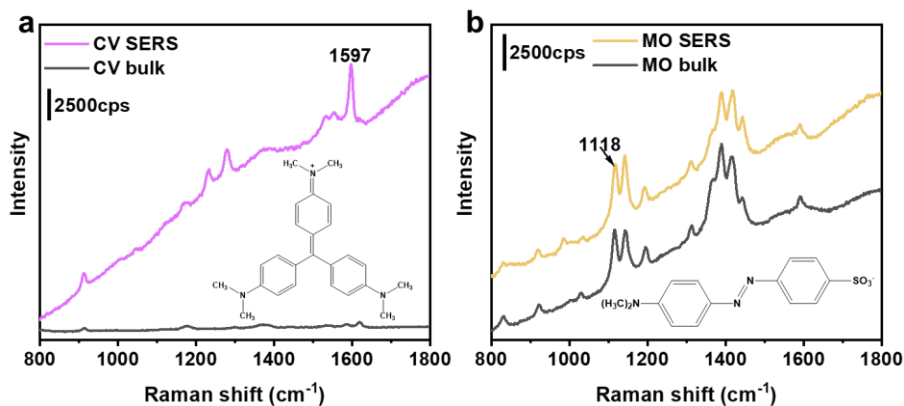


Figure 28. Comparing Raman spectra of bulk dye and SERS spectra of 10^{-5} M dye solution adsorbed on Z700. (a Crystal violet, insert: CV structure; b Methyl orange, insert: MO structure.)

To further verify the effect of interfacial potassium, we design a third set of experiments: use commercially available TiO₂ anatase particles (TP) with high purity (99.9%) and mix it with K₂CO₃ (purity 99%). The mixture was heated at 800°C for 2 hrs to dope different concentrations of potassium. For the studied samples, “TP-0.14” denotes the TP sample with a content of 0.14 wt % potassium. As shown in Figure 29, the TP-0.50 sample has the SERS performance of MB molecules. When the potassium content was increased to 2.45 wt %, new Raman peaks appear at 231, 285, 460 and 859 cm⁻¹ of the TP-2.45 sample, see Figure 6a. Interestingly, If there is a phase transformation from anatase to rutile¹³ (235, 445 and 612 cm⁻¹) shall appear. Judging from the results in Figure 29a, we conclude there is no rutile phase in the studied four samples. Therefore, the new Raman peaks at 231, 285, 460 and 859 cm⁻¹ are attributed to the possible formation of a new potassium titanate compound. Such hypothesis is supported by the literature where similar peaks have been identified from K₂Ti₂O₅ and K₂Ti₆O₁₃.¹⁹ The DFT calculations in Figure 30 also support the formation of a potassium titanate structure. We also note

that while a trace of potassium oxide was applied to TiO₂ samples, it took a longer time (~ 10 s) to detect new Raman peaks. Meanwhile, the prolonged collecting time resulted in very strong intensities of characteristic anatase Raman peaks at 141, 393, 514, 635 cm⁻¹, as shown in Figure 29a. Those peak intensities were beyond the detecting limit of the equipment, therefore were interpreted as plateaus. We note that it is challenging to distinguish details of possible new crystal phases. This is because there are many potassium titanates and each has complex Raman spectra. Also, results in Figure 29b reveal that the Raman signal (1630 cm⁻¹) of MB molecules decreases with the increase of potassium. It suggests that a higher content of potassium would downgrade the Raman scattering performance.

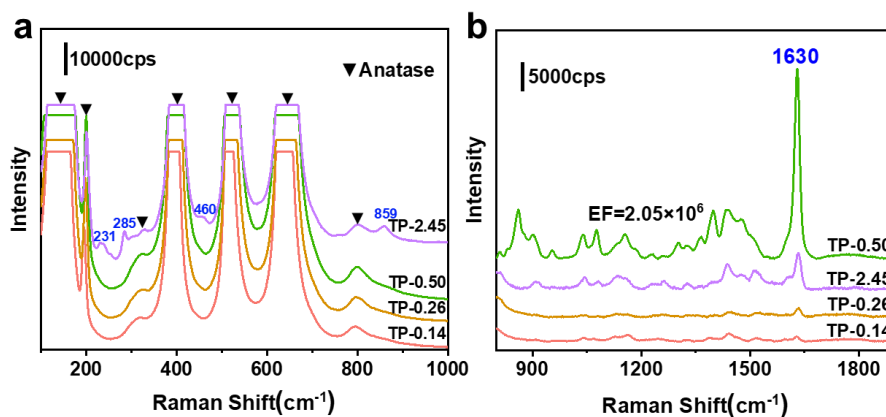


Figure 29. Potassium treated TiO₂ particles and their SERS performance. (a) Raman spectra of commercial TiO₂ particles doped with different content of potassium (0.14, 0.26, 0.50 and 2.45 wt %) and (b) SERS spectra of MB (10⁻⁵ M) on TiO₂ particles.

The content and existence of interfacial trace potassium have been studied in other systems. Xie *et al.* reported that at high temperatures trace salts could disperse on oxide surfaces, spontaneously forming a monolayer.²⁰⁻²¹ In this work, it is hypothesized that trace potassium (0.5 wt %) disperses and stays at the surface of TiO₂ samples. By a simple sphere model, we estimated the coverage of 0.5 wt % potassium on TiO₂ particles with different diameters. The analysis shows

that when the diameter of TiO₂ particle is around 100 nm, which is similar to the size of TiO₂ nanowhiskers in this work, the atomic ratio of potassium/titanium at TiO₂ surface is around 1. Such analysis suggests that the 0.5 wt % of potassium might form a thin layer at the surface of TiO₂ samples and show the best SERS performance.

In order to further understand the interaction between potassium and TiO₂ surface, as well as the potassium/TiO₂ structural information at elevated temperatures, a series of *ab initio* density functional theory (DFT) calculations and *ab initio* molecular dynamics (AIMD) simulations have been performed via Vienna Ab initio Simulation Package (VASP) of the MedeA computational platform.²² The ion-electron interactions were described through the projector-augmented wave (PAW) method,²³ with the electrons from Ti-pv (3p⁶3d²4s²), O (2s²2p⁴) and K-pv (3p⁶4s¹). The electron exchange and correlation interactions were represented by generalized gradient approximation (GGA) of Perdew-Burke-Ernzerhof (PBE) functionals.²⁴ Van der Waals interactions were described through Grimme's DFT-D3 semi-empirical method.²⁵ A cutoff energy of 450 eV was adopted for the planewave basis set and all calculations were performed using a Gaussian smearing with a width of 0.2 eV. The ionic relaxation is considered converged when the atomic force is smaller than 0.02 eV Å⁻¹. Self-consistent field (SCF) cycles would stop when successive energy difference is less than 10⁻⁵ eV.

As shown in Figure 30a, we generated a K-coated TiO₂ model via K₂O dissociative adsorption at the anatase (001) surface. The initial configuration was constructed by placing a 2 × 2 K₂O (001) supercell on top of a 4-layer anatase (001) surface. The anatase (001) surface model had the size of a = b = 11.45 Å, c = 9.50 Å, and a vacuum of 15 Å was added to avoid the interactions between periodic images. During the calculations, the bottom 2 layers were fixed to mimic the bulk behaviour, and all other parts were allowed to relax. It is worth noting that the size of the 2 × 2

K_2O (001) supercell was chosen based on the experimental K/Ti ratio of about 1.0. With our $\text{K}_2\text{O}/\text{TiO}_2$ model, the interfacial K/Ti is 8/9. Figure 30b shows the equilibrium structure at 300 K, where eight potassium distribute nicely at the interface and each form two bonds with neighbouring oxygen sites. For the interfacial oxygens, 4 were from the K_2O supercell and a few Ti-O bonds would break during the structural optimization to form interfacial K-O bonds. Other than that, there is a negligible TiO_2 structural change due to K_2O adsorption, which confirms the XRD results shown in Figure 25b. Thermal stability of the K-coated TiO_2 model has been also tested, as illustrated in Figure 30c, the structure remains stable even at 1000 K. No structural transition was observed for the anatase (001) surface, which is likely due to the stable K/O structure formed at the interface. The excellent thermo stability also explains why the synthesized TiO_2 nanowhisker has a good crystallinity under elevated temperatures up to 900 °C.

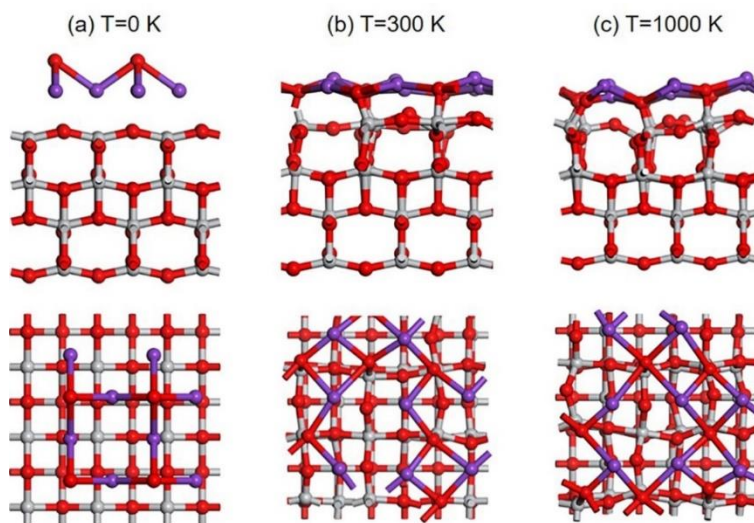


Figure 30. The K-coated TiO_2 model via K_2O dissociative adsorption at the anatase (001) surface. (a) side and top views of the initial configuration, where a 2×2 K_2O (001) supercell is placed on top of a 4-layer anatase (001) surface; (b) side and top views of the equilibrium K-coated TiO_2 model at 300 K; (c) side and top views of the equilibrium K-coated TiO_2 model at 1000 K. Color code: purple, potassium; red, oxygen; gray, titanium.

The surface charge information was also studied via the Bader charge analysis method.²⁶ As illustrated in Figure 31, the interfacial K and O sites were labelled with respective atomic charges. Our calculation agrees with previous DFT results that interfacial potassium would transfer about one electron to neighbouring oxygen sites, therefore carries a positive charge.²⁷ The summation of all interfacial K and O sites produces an overall negative charge of ~ 1.3046 e. The Bader charge analysis explains the Zeta potential measurements in Figure 27f, and also supports the experimental hypothesis that the K-coated TiO₂ nanowhisker has a negative surface charge, therefore favours specific adsorptions of MB and CV molecules via their positively charged groups.

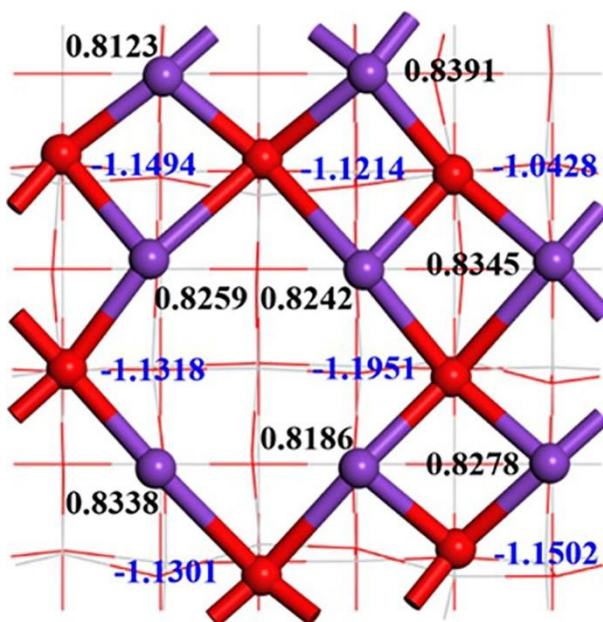


Figure 31. Bader charge analysis for the interfacial potassium and oxygen sites: potassium carries a positive while the oxygen sites have negative charges. For clarity, only the interfacial charge information is displayed. The bottom TiO₂ structure is shown by a line model and the charge information is not shown. Colour code: purple, potassium; red, oxygen.

6.4 Conclusions

In summary, TiO₂ nanowhiskers have been synthesized with excellent surface enhanced Raman spectroscopy properties towards molecules with positive charge groups such as methylene blue and crystal violet. By a combination of experimental characterizations and computational studies, we reveal that the single-layer coated potassium at the TiO₂ nanowhisiker helps to achieve a high thermo stability, which in return enables a high crystallinity at elevated temperatures up to 900 °C. In addition, Zeta potential measurements and theoretical Bader charge analysis show that the K-coated nanowhisiker carries negative surface charges, which favors specific adsorptions of methylene blue molecules, and promotes the SERS enhancement factor, an index of SERS performance, to be about 4.96×10^6 and a detection limit around 10^{-7} M.

6.5 References

1. Zong, C.; Xu, M. X.; Xu, L. J.; Wei, T.; Ma, X.; Zheng, X. S.; Hu, R.; Ren, B., Surface-Enhanced Raman Spectroscopy for Bioanalysis: Reliability and Challenges. *Chem. Rev.* **2018**, *118* (10), 4946.
2. Yan, X. F.; Xu, Y.; Tian, B. Z.; Lei, J. Y.; Zhang, J. L.; Wang, L. Z., Operando Sers Self-Monitoring Photocatalytic Oxidation of Aminophenol on Tio2 Semiconductor. *Appl Catal B-Environ* **2018**, *224*, 305.
3. Yu, J.; Lei, J. Y.; Wang, L. Z.; Zhang, J. L.; Liu, Y. D., Tio2 Inverse Opal Photonic Crystals: Synthesis, Modification, and Applications - a Review. *J. Alloys Compd.* **2018**, *769*, 740.
4. Alessandri, I.; Lombardi, J. R., Enhanced Raman Scattering with Dielectrics. *Chem. Rev.* **2016**, *116* (24), 14921.
5. Yang, L. L.; Peng, Y. S.; Yang, Y.; Liu, J. J.; Li, Z. Y.; Ma, Y. F.; Zhang, Z.; Wei, Y. Q.; Li, S.; Huang, Z. R.; Long, N. V., Green and Sensitive Flexible Semiconductor Sers Substrates: Hydrogenated Black Tio2 Nanowires. *ACS Appl. Nano Mater.* **2018**, *1* (9), 4516.

6. Alessandri, I., Enhancing Raman Scattering without Plasmons: Unprecedented Sensitivity Achieved by TiO₂ Shell-Based Resonators. *J. Am. Chem. Soc.* **2013**, *135* (15), 5541.
7. Qi, D. Y.; Lu, L. J.; Wang, L. Z.; Zhang, J. L., Improved SERS Sensitivity on Plasmon-Free TiO₂ Photonic Microarray by Enhancing Light-Matter Coupling. *J. Am. Chem. Soc.* **2014**, *136* (28), 9886.
8. Liu, L.; Pan, F.; Liu, C.; Huang, L. L.; Li, W.; Lu, X. H., TiO₂ Nanofoam-Nanotube Array for Surface-Enhanced Raman Scattering. *Acs Appl Nano Mater* **2018**, *1* (12), 6563.
9. Cong, S.; Yuan, Y. Y.; Chen, Z. G.; Hou, J. Y.; Yang, M.; Su, Y. L.; Zhang, Y. Y.; Li, L.; Li, Q. W.; Geng, F. X.; Zhao, Z. G., Noble Metal-Comparable SERS Enhancement from Semiconducting Metal Oxides by Making Oxygen Vacancies. *Nat. Commun.* **2015**, *6*.
10. Schneider, J.; Matsuoka, M.; Takeuchi, M.; Zhang, J. L.; Horiuchi, Y.; Anpo, M.; Bahnemann, D. W., Understanding TiO₂ Photocatalysis: Mechanisms and Materials. *Chem. Rev.* **2014**, *114* (19), 9919.
11. Gong, M. D.; Jiang, X.; Du, J.; Li, X. L.; Han, X. X.; Yang, L. B.; Zhao, B., Anatase TiO₂ Nanoparticles with Controllable Crystallinity as a Substrate for SERS: Improved Charge-Transfer Contribution. *RSC Adv.* **2015**, *5* (98), 80269.
12. Li, W.; Bai, Y.; Liu, C.; Yang, Z. H.; Feng, X.; Lu, X. H.; van der Laak, N. K.; Chan, K. Y., Highly Thermal Stable and Highly Crystalline Anatase TiO₂ for Photocatalysis. *Environ. Sci. Technol.* **2009**, *43* (14), 5423.
13. Zhang, J.; Li, M. J.; Feng, Z. C.; Chen, J.; Li, C., Uv Raman Spectroscopic Study on TiO₂. I. Phase Transformation at the Surface and in the Bulk. *J. Phys. Chem. B* **2006**, *110* (2), 927.
14. Yang, L. B.; Gong, M. D.; Jiang, X.; Yin, D.; Qin, X. Y.; Zhao, B.; Ruan, W. D., Investigation on SERS of Different Phase Structure TiO₂ Nanoparticles. *J. Raman Spectrosc.* **2015**, *46* (3), 287.

15. Dong, B.; Huang, Y. Z.; Yu, N. S.; Fang, Y. R.; Cao, B. S.; Li, Y. Z.; Xu, H. X.; Sun, M. T., Local and Remote Charge-Transfer-Enhanced Raman Scattering on One-Dimensional Transition-Metal Oxides. *Chem.-Asian J.* **2010**, *5* (8), 1824.
16. Yang, L. B.; Jiang, X.; Ruan, W. D.; Zhao, B.; Xu, W. Q.; Lombardi, J. R., Observation of Enhanced Raman Scattering for Molecules Adsorbed on TiO₂ Nanoparticles: Charge-Transfer Contribution. *J. Phys. Chem. C* **2008**, *112* (50), 20095.
17. Hussain, H.; Tocci, G.; Woolcot, T.; Torrelles, X.; Pang, C. L.; Humphrey, D. S.; Yim, C. M.; Grinter, D. C.; Cabailh, G.; Bikondoa, O.; Lindsay, R.; Zegenhagen, J.; Michaelides, A.; Thornton, G., Structure of a Model TiO₂ Photocatalytic Interface. *Nat. Mater.* **2017**, *16* (4), 461.
18. Lin, J.; Shang, Y.; Li, X. X.; Yu, J.; Wang, X. T.; Guo, L., Ultrasensitive Sers Detection by Defect Engineering on Single Cu₂O Superstructure Particle. *Adv. Mater.* **2017**, *29* (5), 1604797.
19. Bamberger, C. E.; Begun, G. M.; Macdougall, C. S., Raman-Spectroscopy of Potassium Titanates - Their Synthesis, Hydrolytic Reactions, and Thermal-Stability. *Appl. Spectrosc.* **1990**, *44* (1), 30-37.
20. Yu, X. F.; Wu, N. Z.; Xie, Y. C.; Tang, Y. Q., A Monolayer Dispersion Study of Titania-Supported Copper Oxide. *J. Mater. Chem.* **2000**, *10* (7), 1629.
21. Lin, C. Z.; Cai, X. H.; Xie, Y. C., Study of Dispersion State of CCl₂ onto the Surface of NaY Zeolite. *Acta Phys-Chim Sin* **1996**, *12* (6), 523.
22. Kresse, G.; Furthmuller, J., Efficient Iterative Schemes for Ab Initio Total-Energy Calculations Using a Plane-Wave Basis Set. *Phys. Rev. B* **1996**, *54* (16), 11169.
23. Blochl, P. E., Projector Augmented-Wave Method. *Phys. Rev. B* **1994**, *50* (24), 17953.
24. Perdew, J. P.; Burke, K.; Ernzerhof, M., Generalized Gradient Approximation Made Simple. *Phys. Rev. Lett.* **1996**, *77* (18), 3865.

25. Grimme, S.; Antony, J.; Ehrlich, S.; Krieg, H., A Consistent and Accurate Ab Initio Parametrization of Density Functional Dispersion Correction (DFT-D) for the 94 Elements H-Pu. *J. Chem. Phys.* **2010**, *132* (15), 154104.
26. Bader, R. F. W., Atoms in Molecules. *Acc. Chem. Res.* **1985**, *18* (1), 9.
27. Calatayud, M.; Minot, C., Effect of Alkali Doping on a V₂O₅/TiO₂ Catalyst from Periodic DFT Calculations. *J. Phys. Chem. C* **2007**, *111* (17), 6411.

Chapter 7: Friction of Ionic Liquid–Glycol Ether Mixtures at Titanium Interfaces: Negative Load Dependence*

7.1 Introduction

Friction, as one of the oldest phenomena, is one of the major causes that result in energy and material losses in mechanical processes,¹ and plays an important role in the history of mankind and in particular of natural science. The milestone of friction mechanism was established in the 17th century² that friction force is linearly proportional to the normal load. This theorem, also known as Amontons' Law, in which the monotonic increase of friction with load has been observed across a range of length scales.³ Amontons' law remains good at describing the friction behavior in the majority of rubbing surfaces, involving both dry and lubricated contacts, both rough and smooth surfaces, both ductile and brittle, and both macroscopic and microscopic contacts.³

Despite the successfulness of Amontons's Law at macro- and micro- scales, one has to pay special attention to friction-relevant quantities at micro- and nano- level. Especially, the frictional phenomena are more complex, when it comes to soft contact interfaces, such as those composed of liquid/liquid or liquid/solid interfaces, because interfacial structural transitions at higher normal load might occur. For example, recent friction studies of lamellar graphite surface revealed a negative friction coefficient during the atomic force microscopy (AFM) tip retraction process, i.e., the friction force increases as the normal load decreases.⁴ Such negative correlation between friction force and normal load is not inherent in the Amontons's Law. Yet, it has been observed from various systems (e.g., graphite, graphene, polymers, or other two-dimensional materials,) and under different conditions (such as vacuum).⁵⁻¹⁰

*An, R.; Zhou, G.; Zhu, Y.; Zhu, W.; Huang, L.; Shah, F. U. Friction of Ionic Liquid–Glycol Ether Mixtures at Titanium Interfaces: Negative Load Dependence. *Adv. Mater. Interfaces* 2018. 5, 1800263

In the graphene system, the negative friction coefficient is attributed to the partial delamination (exfoliation) of topmost graphene layers. When the AFM tip retracts, the tip-surface adhesion force can overcome graphite exfoliation energy. Thus, the tip will lift the upper graphene layer(s), and separate them locally from the bulk. Therefore, during the friction force measurement, a ripple is formed around the AFM tip. In addition, both the ripple height and width will change dynamically in response to the tip retraction and the resulted exfoliation of topmost graphene layers. Such nanoscale dynamic change of the sliding interface leads to a fundamentally different friction coefficient, which, on the other hand, is not incorporated in the Amontons's Law. This lack explains why both positive and negative friction-load dependence were observed on the same suspended graphene in different load regimes, from AFM experimental⁷ and atomistic simulation⁸ studies.

In this work, by a combination of AFM experiments and molecular dynamics simulations, we report another type of negative friction-load dependence from ionic liquid (IL) systems: the phosphonium based IL/glycol ether base oil mixture was added onto titanium substrate as lubricant. We employed IL/oil mixtures in our experiments, because of the ILs' high viscosity, which would result in a high friction force.¹¹ More importantly, the main cause of friction in hydrodynamic and elastohydrodynamic regimes is hydrodynamic drag, which consumes 10-15% of the total energy and is proportional to the lubricant viscosity.¹² Also, the neat ILs as lubricants are more expensive compared with conventional base oils.¹³⁻¹⁵ One method to improve ILs lubricating efficiency and reduce the cost, is to use less viscous lubricants by employing ILs as additives in base oils,⁷ and we therefore investigate in this study the friction behavior of IL/oil mixtures at Ti interfaces.

Non-equilibrium molecular dynamics (NEMD) simulations in our work revealed a similar negative load-dependent friction behavior as observed in our AFM experiment, and exhibited the

IL structural reorientation during tip sliding. When the normal load increases, the cation alkyl chains change their orientation, generating a new interface for tip sliding with smaller friction force. This structural transition was further supported by calculating self-diffusion properties of the studied IL. With a slit-pore model, mimicking the confinement environment near the tip, we observed a faster self-diffusion of IL, implying that at larger normal loads, the IL will diffuse faster to facilitate the structural reorientation and the new sliding interface formation.

7.2 Experiments and Simulations

7.2.1 Samples Preparation.

Four ionic liquids were synthesized using methods as reported previously,¹⁶⁻¹⁸ i.e., tributyloctylphosphonium bis(salicylato)borate ([P_{4,4,4,8}][BScB]), trihexylte-tradecylphosphonium bis(salicylato)borate ([P_{6,6,6,14}][BScB]), trihexyltetradecylphosphonium bis-(mandelato)borate ([P_{6,6,6,14}][BMB]), and trihexyltetradecylphosphonium bis(oxalato)borate ([P_{6,6,6,14}][BOB]). We also compared the behavior of the commercial IL trihexyltetradecylphosphonium dicyanamide ([P_{6,6,6,14}][DCA]) purchased from Cytec and used as received. The experimental samples were prepared by mixing 75wt% ionic liquids in the base oil of diethylene glycol dibutyl ether (DEGDBE, ACROS organics, purity \geq 99%). The IL/oil lubricating film was deposited onto Ti substrate (Sigma-Aldrich, Titanium, foil, thickness 0.25 mm, 99.7% trace metals basis, Product No. 267503) by the spin-coating method at the speed of 5000 rpm for 60 s. It is important to note that the Ti surfaces we used here are α -Ti. Based on our X-ray diffraction (XRD) patterns, the α -Ti phase has an hcp crystal structure with lattice parameters of $a=2.95$ Å, $b=2.95$ Å, $c=4.68$ Å, and structure angles of $\alpha=90^\circ$, $\beta=90^\circ$, $\gamma=120^\circ$ (reference code: 00-044-1294).

7.2.2 Friction Measurements.

Friction force measurements ($5\ \mu\text{m} \times 5\ \mu\text{m}$) were performed on a Multimode 8 atomic force microscopy (AFM, Bruker) using Si_3N_4 cantilever tips (DNP-10, A tip, nominal tip radius=20 nm, tip height=6 μm) with a nominal spring constant of 0.35 N/m in contact mode at ambient conditions, and the scan rate was 2 Hz. The normal spring constant of each AFM tip was calibrated using normal deflection sensitivity of the supported cantilever to transform the normal load signals (in V) into true normal load (in N). The calibration procedure was performed whenever a different cantilever was used. The average lateral force, given in terms of an output voltage signal (half-difference of the average lateral deflection signal on the photodetector of the forward and reverse traces, in V), was transformed into the friction force (in N) from the torsion of the cantilever.¹⁹ Friction force data presented in this work are the average of five measurements at multiple sample positions.

7.2.3 X-ray Photoelectron Spectroscopy (XPS).

XPS (Thermal Scientific, USA) analysis was performed on samples before and after AFM friction measurements to detect possible changes in interfacial compositions due to AFM tip sliding. The analysis was conducted on an Escalab 250Xi Imaging X-ray photoelectron spectrometer with a monochromatic Al K α X-ray small spot source (1486.6 eV).

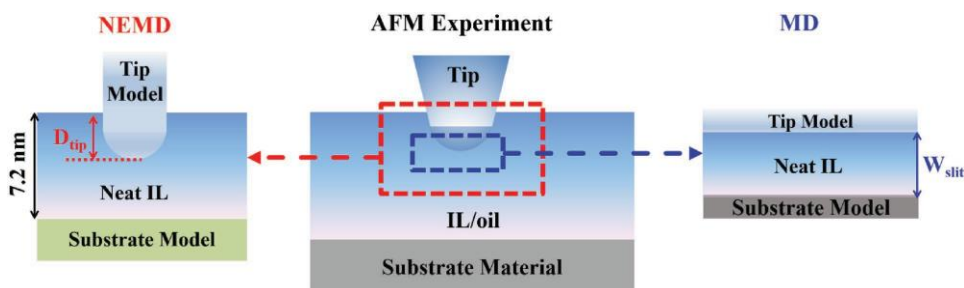


Figure 32. Illustration and connection map of AFM experiments and theoretical simulations.

7.2.4 Molecular Simulations.

As illustrated in Figure 32, two types of molecular dynamics calculations were performed to interpret AFM measurements and reveal the molecular level fundamental mechanisms: (a) non-equilibrium simulations (NEMD) of the friction process, and (b) molecular simulation (MD) of the self-diffusion in the confined IL.

Recent advances in NEMD simulations of lubricants and additives have been reviewed by Ewen and Co-workers.²⁰ Another review of atomic frictions by Dong and Co-authors,²¹ where important parameters, such as materials, surfaces, compliance, contact area, normal load, temperature and velocity, have been described in the context of both experiments and simulations. In our NEMD calculations, the AFM tip was modelled as a capped single-walled carbon nanotube (SWCNT) with the cap radius of 0.5 nm, to help us understand the underlying mechanisms of the friction behavior, as what had been done in previous studies.²²

The neat IL [P_{4,4,4,8}][BScB] was adopted as the lubricant because adding base oil does not change the observed trend, which would be explained later in results and discussion. The simulation box has the dimension of $4.61 \times 4.61 \times 16.5 \text{ nm}^3$, with 150 [P_{4,4,4,8}][BScB] molecules. The bottom of the simulation box was modeled via a fixed Si surface. Our NEMD friction simulation protocol started placing the capped SWCNT tip 2.0 nm (the initial insertion depth, D_{tip}) into the IL/Si system to ensure the tip surrounded by the IL molecules, i.e., 5.2 nm away from the IL/Si interface (IL thickness of $\sim 7.2 \text{ nm}$). We applied varying external normal loads to approach the tip to the IL/Si interface and make intimate contact between the tip and ILs. And we simultaneously slid the IL/Si(111) interface laterally with the tip at a constant velocity of 1.0 m/s. In our NEMD friction calculation, the non-bonded interactions, consisted of van der Waals (vdW) and electrostatic interactions, between different atoms were described by the L-J 12-6 and

Coulombic potentials, respectively. The SWCNT tip was modeled as neutrally charged particles, so there exist no long-range electrostatic interactions, but only short-range van der Waals forces between the IL and the neutrally modeled tip. The cutoff distance for non-bonded interactions was 1.5 nm, and the particle-particle particle-mesh (PPPM) method was employed to calculate these interactions.²³ The friction force along the tip moving path were determined via an estimation of averaged interactions between the IL and the neutrally modeled SWCNT tip during sliding. It is noting that our friction calculation started placing the SWCNT tip 5.2 nm away from the IL/Si interface which is much larger than the 1.5 nm cutoff distance, indicative of no interactions between the tip and Si substrate. The Si surface is therefore simply served herein as a rigid wall to hold simulation box. About the MD simulation for the self-diffusion of the confined IL, we applied a slit-pore model to calculate self-diffusion properties of confined [P_{4,4,4,8}][BScB], to understand the dynamics of those near-tip IL molecules when the tip approaches the substrate, as demonstrated in Figure 32. The slit pore was composed of the rigid graphene tip and rutile (110) substrate with the thickness of 1.17 nm.

Here in diffusion calculations, the surface of the substrate is critical. In order to evaluate the mobility of ILs during AFM tip approaching, the entire ILs diffusion confined between the tip and the substrate has been to consider. This is different from that in NEMD friction calculations, which focused on the tip sliding interface, and the IL molecules around the sliding tip is critical in NEMD simulations. The rutile was thus adopted to model the substrate in MD simulations to mimic the material used in AFM experiments, because native dense titanium dioxide layers²⁴ are usually formed on the Ti surface. Three pore sizes were investigated: $W_{\text{slit}} = 5, 7$ and 9 nm. The diffusion coefficient can be determined from the Einstein Relation: $\langle |r(t) - r(0)|^2 \rangle = 2dDt$, where $r(t)$ is the position of the mass center of IL [P_{4,4,4,8}][BScB] molecule at time t , D is the diffusion coefficient.²⁵

7.2.5 Contact Angle, Density and Viscosity Measurements.

Contact angles were measured using a Fibro 1121/1122 DAT-Dynamic absorption and contact angle tester equipped with a CCD camera at room temperature and ambient humidity. Four drops of IL/oil mixtures were placed on Ti substrates manually via a syringe fixture. An Anton-Paar DMA 4100 density meter was used to measure the density at 20 °C. Viscosity was measured with a Lovis 2000 ME Microviscometer (Anton-Paar falling ball type viscometer) at 20 °C using a sealed sample tube.

7.3 Results and Discussion

We studied a combination of ionic liquid anions and cations, and their mixture with the base oil, diethylene glycol dibutyl ether (DEGDDBE). The chemical structures of the phosphonium cations, $[P_{4,4,4,8}]^+$, $[P_{6,6,6,14}]^+$ and anions, $[BOB]^-$, $[BMB]^-$, $[DCA]^-$, $[BScB]^-$, as well as the base oil DEGDDBE are shown in Figure 33.

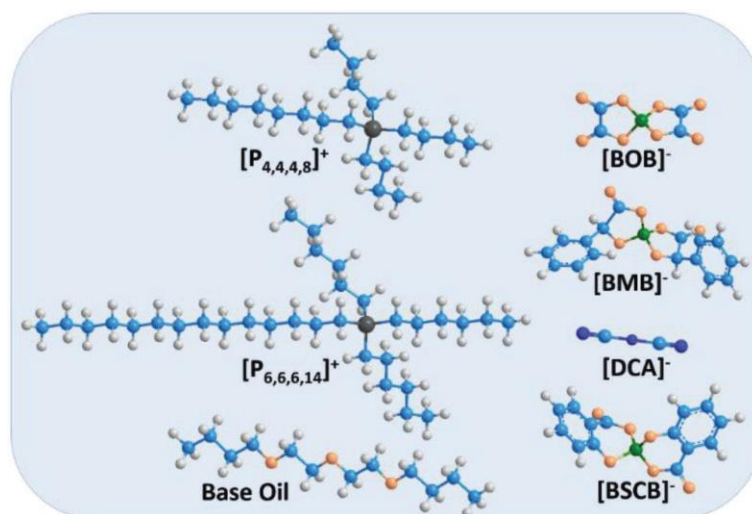


Figure 33. Structures of two cations, $[P_{4,4,4,8}]^+$ and $[P_{6,6,6,14}]^+$; four anions, $[BOB]^-$, $[BMB]^-$, $[DCA]^-$, and $[BScB]^-$; base oil DEGDDBE. Color codes are: P (black), B (olive), C (blue), H (gray), O (orange), N (navy).

The 75 wt% IL/oil mixtures in our work demonstrate the similar viscosity dependence on anions of ILs as neat ILs.¹⁶ The dependence of densities for IL/oil mixtures on anions also follows the same trend observed in neat ILs.¹⁶ This is indicative of the addition of base oil has no influence on the dependence of viscosities & densities on anions observed in our IL/oil mixtures. Our experience has shown that surface wetting properties exhibit strong effects on the interfacial friction.²⁶ We thus examined the IL/oil wettability on Ti substrates, and observed no significant differences in contact angles of different IL/oil mixtures on Ti substrates, indicating the wetting behavior for different IL/oil mixtures on Ti surfaces is similar. So we can exclude the possibility that the following different friction forces of different IL/oil systems result from the interfacial wetting behavior.

7.3.1 Negative Friction-Load Dependence in IL/Oil Mixtures at Titanium Interfaces Observed by AFM

The friction properties of the IL/oil mixture coated Ti surfaces were probed by AFM with the 20 nm radius Si₃N₄ tip. As shown in Figure 34(a), a negative friction-load dependence was observed for all the studied 75wt% IL/oil mixtures at Ti interfaces, that is, the friction force decreases as the normal load increases. This negative load dependent behavior was not only observed in 75wt% IL mixtures at Ti interfaces, but also in the neat IL-Ti system and 25 wt% IL/oil (1/3 in wt/wt) mixtures at Ti interfaces. We focused on the 75wt% IL systems in this work. The deeper and systematical investigation on the latter ones would be our next urgent step. In this work, we focused on the 75 wt% IL systems to reveal the cause of the observed phenomenon. A systematical study is undergoing to investigate substrate effect, and whether the negative friction-load dependence can be extended to other IL systems. It is worth noting, as shown in Figure 34(a),

anomalously larger friction forces than normal load were observed in 75 wt% IL systems, however, this phenomenon disappeared in 25 wt% IL systems, and occurred again in the neat IL [P6,6,6,14][BOB] coated Ti substrates. It is unusual to observe larger friction forces than normal load, but it happens, in different ways. For example, large friction forces were observed for a metal-coated AFM tip on mica in UHV at high loads, due to the wear of the surface.²⁷ In the case of an IL between negatively charged surfaces, the stable IL structures contain different layers of ions. When the interlocking of those ion layers is strongly ordered, the resulted friction force could also be larger than the normal load.²⁸⁻²⁹

We attribute the larger friction forces observed in our 75 wt% and neat IL systems to the high viscosity. Because the main cause of friction in hydrodynamic/elastohydrodynamic regimes is hydrodynamic drag, which is proportional to the lubricant viscosity.¹² This indicates that high viscous ILs could result in a high friction force.¹¹ As we expected, viscosities in 75 wt% IL/oil mixtures are much higher than that in 25 wt% mixtures, and friction forces in latter systems are smaller than normal load, with small friction coefficient. So a small amount of the addition of ILs in base oil is favorable in reducing friction, and it is necessary for us in a near future to explore the friction behavior in IL/oil mixtures by adding small amounts of ILs in base oil. In Figure 34(a), the lowest friction is observed at the Ti interfaces coated with IL containing [BScB]⁻ anion. By comparing the two ILs containing [BScB]⁻ anion, the IL containing phosphonium cation [P_{6,6,6,14}]⁺ with longer chain provided lower friction forces. On the contrary, without ILs, for the bare Ti surface and the Ti surface lubricated by the neat base oil (DEGDBE), there is a positive friction-load dependence: the measured friction force increases linearly when the normal load increases, following existing tribological models previously reported.^{7, 13, 30} The fitted friction coefficients from Figure 34(b) were 0.48 and 0.13 for the bare and the base oil lubricated Ti surfaces

respectively. Pertinent questions are why ‘negative’ situation of friction-load dependence occurs at titanium surfaces lubricated with 75wt% IL/oil mixtures, but not at the bare Ti surface and the Ti surface lubricated with neat DEGDBE. What is the origin of the negative friction-load dependence for IL/oil mixtures at Ti interfaces? The resolution of the friction data is insufficient to determine the observed ‘negative notion’, friction loops and molecular simulation would be performed further to manifest the friction-load relationship.

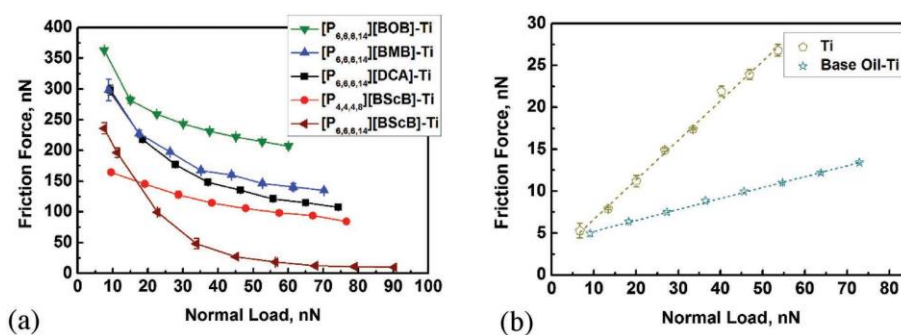


Figure 34. Friction measurements for (a) the IL/oil mixtures coated Ti interfaces, where 75 wt% of ILs, namely, $[P_{6,6,6,14}][BOB]$, $[P_{6,6,6,14}][BMB]$, $[P_{6,6,6,14}][DCA]$, $[P_{4,4,4,8}][BScB]$, and $[P_{6,6,6,14}][BScB]$, have been studied; (b) bare Ti and base oil lubricated Ti interfaces.

7.3.2 Interfacial Chemical and Topographical Properties.

Friction properties can be greatly influenced by chemical composition changes of the interface. The Ti surfaces coated by the $[P_{4,4,4,8}][BScB]$ -base oil mixture are examined by X-ray photoelectron spectroscopy (XPS) before and after friction tests in order to get deeper insights into any chemical reactions occurring at the interfaces. Figure 35(a) shows the survey spectra of the $[P_{4,4,4,8}][BScB]$ -base oil coated Ti surface. It clearly reveals the presence of C 1s, O 1s, P 2p, B 1s on the surface, before and after AFM measurements, and no significant changes were observed in binding energies (< 0.1 eV). This indicates the surface compositions of IL/oil mixtures at Ti interfaces are not influenced by AFM sliding procedure. In addition, no new peaks were observed

in the high-resolution spectrum of the C 1s after AFM friction measurements (Figure 35b). As seen in the high-resolution spectrum of the C 1s electron region before and after AFM measurements, three major carbon-containing functional groups are present at 284.7, 286.2 and 288.6 eV, respectively. The C 1s peak component at 284.7 eV (C-C/C=C)³¹ is attributed to alkyl chains of the [P_{4,4,4,8}] cation and DEGDBE, as well as the aromatic ring of the [BScB] anion. A distinct C-O peak at 286.2 eV and the presence of C(=O)-O bond at 288.6 eV³¹ are assigned to the aromatic ring of the [BScB] anion. Moreover, electron regions of O 1s, P 2p, B 1s + P 2s, exhibit in the same way before and after AFM sliding procedure. The XPS analysis was also performed for other systems involving [P_{6,6,6,14}][BOB]-, [P_{6,6,6,14}][BMB]-, [P_{6,6,6,14}][DCA]-, [P_{6,6,6,14}][BScB]- base oil mixtures at Ti surfaces. Comparing the spectroscopy information before and after the AFM measurements, no changes in both the shape of signal and binding energy values were observed, demonstrating no chemical reactions occurred during AFM sliding.

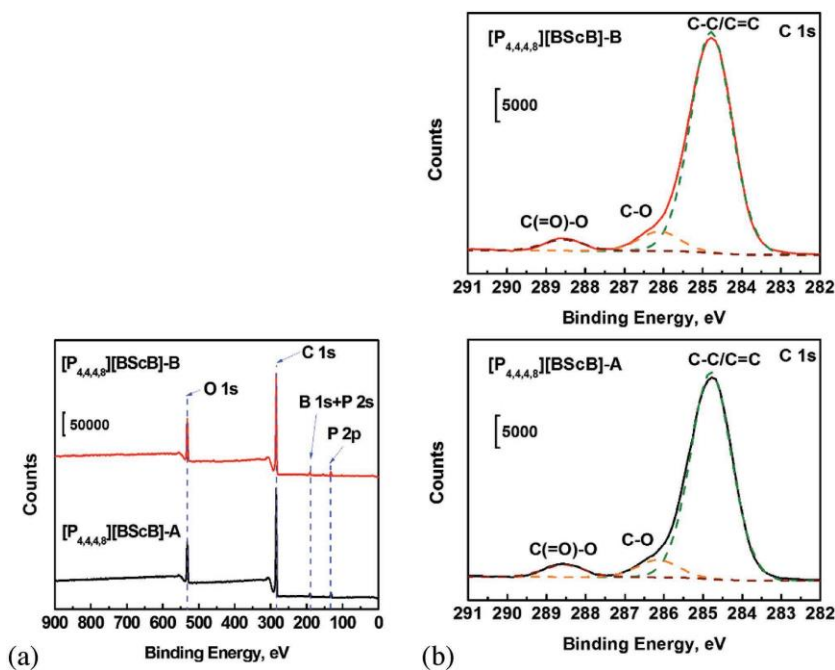


Figure 35. XPS spectra of [P_{4,4,4,8}][BScB]-oil mixtures at Ti interfaces, before ([P_{4,4,4,8}][BScB]-B) and after ([P_{4,4,4,8}][BScB]-A) AFM friction measurements: a) survey, b) high resolution C 1s scans.

For the Ti surface coated by the [P_{4,4,4,8}][BScB]-base oil mixture, two typical examples were presented in Figure 36: one is the topographic image at a small normal load, 9.6 nN, and the RMS roughness is 97.9 nm; the other is at a large normal load, 76.6 nN, and the RMS roughness is 98.5 nm. It is apparent that no significant disruption (or roughness change) was observed as the load increased. Similarly, this absence of disruptions holds true to other studied systems.

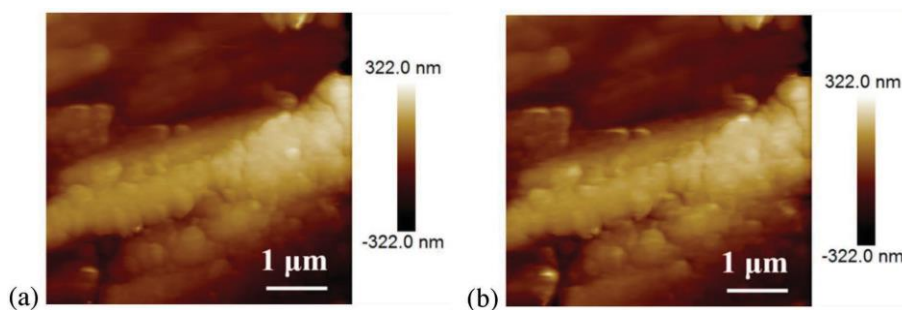


Figure 36. Topographic images of [P_{4,4,4,8}][BScB]-oil mixtures at Ti interfaces at a) smaller normal load of 9.6 nN and b) larger normal load of 76.6 nN.

7.3.3 Friction Loops Dependence.

As illustrated in Figure 37, at smaller normal loads, e.g., $F_N = 28.7$ nN, AFM tip shears against the IL/oil mixture layer far away from the Ti surface. However, the probe penetrates the near surface layer³²⁻³⁴ at higher loads, e.g., $F_N = 76.6$ nN, and shears against a different IL/oil mixture layer which can be substantially suppressed on the Ti surface. From the recorded high-resolution traces, where the friction force is plotted as a function of the lateral displacement, the friction does not always remain as a constant and changes locally. As illustrated in Figure 37, a decrease of the friction loop width was observed when the normal load was increased from 28.7 nN to 76.6 nN. It is concluded that the frictional interaction strength of the studied IL/oil mixtures, which is the difference between the forward and the backward friction traces, demonstrated the order: [P_{6,6,6,14}][BOB] > [P_{6,6,6,14}][BMB] > [P_{6,6,6,14}][DCA] > [P_{4,4,4,8}][BScB] > [P_{6,6,6,14}][BScB]. Such

order is in agreement with the friction force measurements of Figure 34(a). The frictional interaction strength corresponds to the magnitude of dissipation energy due to friction, and provides a quantitative measurement of the energy lost during a friction loop.³⁵

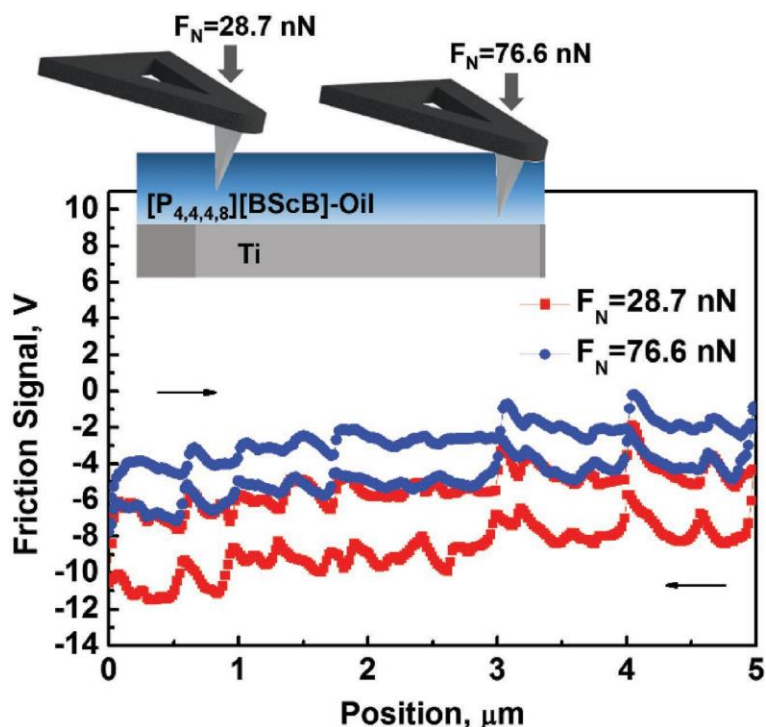


Figure 37. Typical friction loops taken for $[P_{4,4,4,8}][BScB]$ with concentration of 75 wt% in oil at Ti interfaces at two different normal loads (F_N). Friction values, here given in V, are calculated as the average difference for each interfaces, in the friction loop between the back and forth scans. The back-and-forth displacement is in the directions indicated by black arrows.

7.3.4 Negative ‘Friction-Load Dependence’ Observed by Simulation.

In order to reveal the fundamental mechanism at the molecular level, we performed a series of non-equilibrium molecular dynamics (NEMD) simulations to study the atomic-scale sliding friction in ILs that is not accessible by AFM. Since the negative friction-load dependence was observed only when the ILs were used in the AFM experiments. We observed also a negative load

dependent behavior in the neat IL-Ti system, so we adopted the neat IL [P_{4,4,4,8}][BScB] as the model to simplify the friction calculation process. The AFM tip was modeled by a capped carbon nanotube. Figure 38 shows the calculated friction force as a function of different normal loads, and a smaller friction was observed when increasing the normal load. The simulation results reveal a similar negative friction-load dependence as observed in our experiments, although there are differences in the magnitude of the friction and load. The larger friction forces than normal load were also observed in the neat IL system using NEMD simulations, in agreement with that were found in AFM experiments, and we attributed this unusual phenomena still to the high viscosity. The fact that both experiments and simulations exhibit the same trending, despite their very different speeds and tips, suggests the mechanisms observed in simulations are indeed applicable to the corresponding experiments.

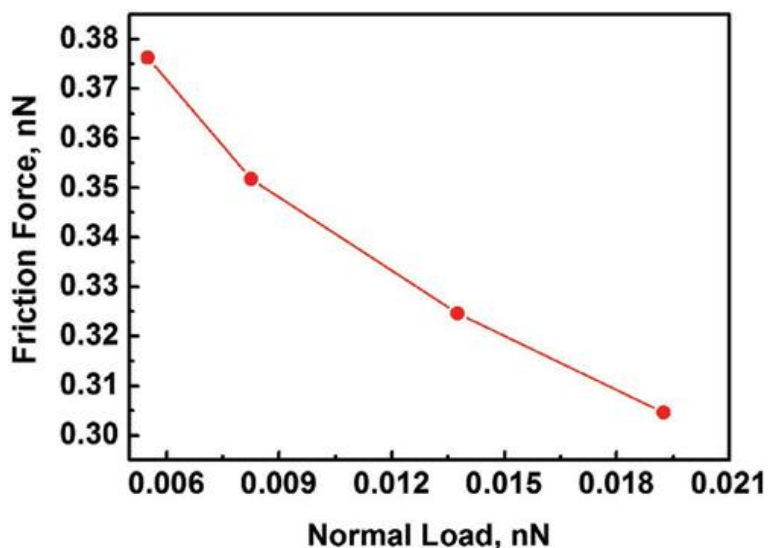


Figure 38. Friction as a function of normal load in the [P_{4,4,4,8}][BScB] case, from NEMD simulations.

7.3.5 Structural Changes of Ionic Liquids

The changes in ion packing, i.e., structural changes, as the AFM tip penetrates the ILs layer at higher loads, were further observed in the $[P_{4,4,4,8}][BScB]$ system around the tip during AFM scanning. The orientational probability of cations and anions was an excellent way to interpret the local structure of the ionic liquid. To determine the orientation behavior of cations and anions at the tip interface, we defined the vector P_{4-1} , P_{4-2} , P_{4-3} , P_8 and B_1 , B_2 of cation and anion respectively using molecular simulation as shown in insets in right panels of Figures 39(a) and (b). We then defined angle θ of alkyl chain vector P_{4-1} , P_{4-2} , P_{4-3} , P_8 in cation $[P_{4,4,4,8}]^+$ with respect to the normal vector z , and angle ψ of the vector B_1 , B_2 in anion $[BScB]^-$ to the normal vector z .

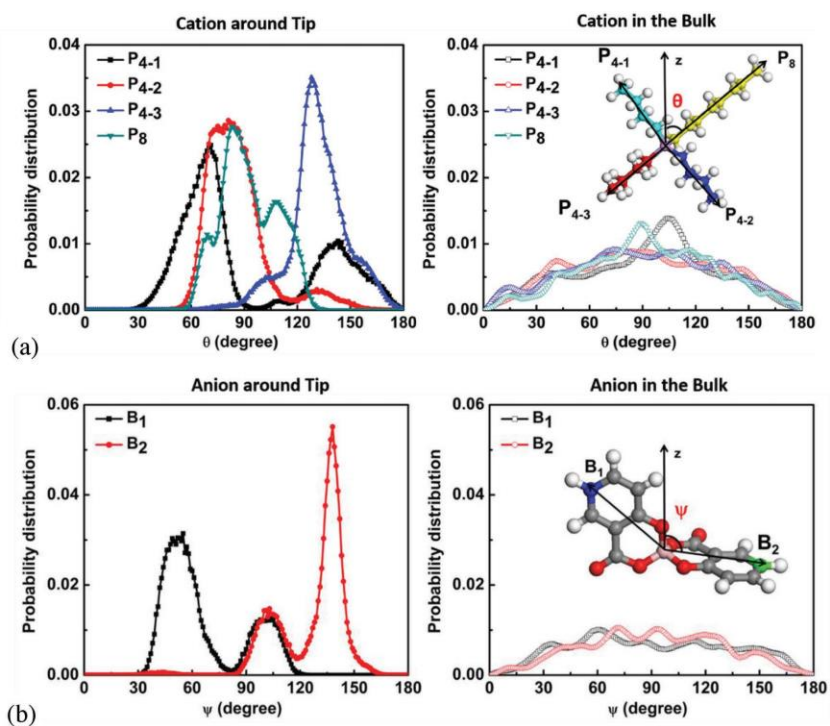


Figure 39. Orientational probabilities of (a) the angle θ between the interface normal vector z and the alkyl chain vector P_{4-1} , P_{4-2} , P_{4-3} , P_8 in the cation $[P_{4,4,4,8}]^+$ (left) around the tip and (right) in the bulk system, (b) the angle ψ between the interface normal vector z and the vector B_1 , B_2 in the anion $[BScB]^-$ (left) around the tip and (right) in the bulk system. The insets in right panels of (a) and (b) show the vector definition for the orientation analysis of cation and anion, respectively.

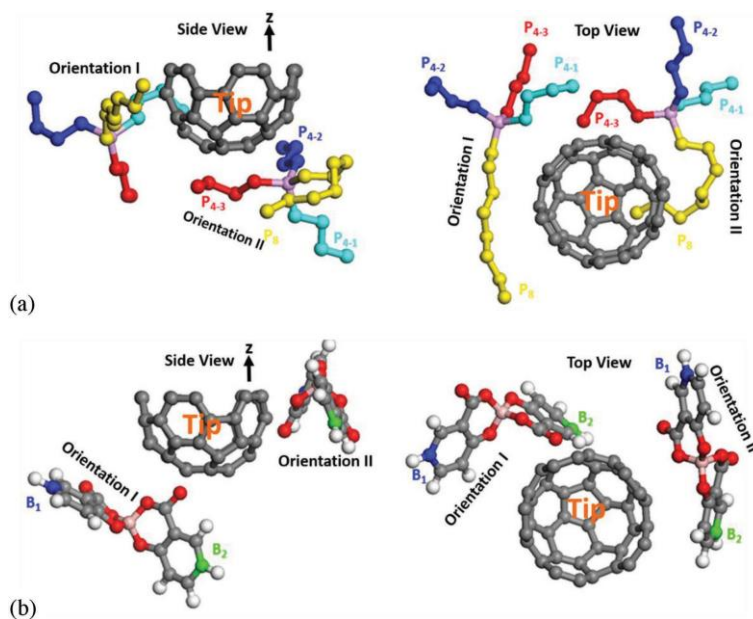


Figure 40. (a) and (b) are the sketch map showing the main orientations of P₄₋₁, P₄₋₂, P₄₋₃, P₈ in the cation [P_{4,4,4,8}]⁺, and B₁, B₂ in the anion [BScB]⁻, respectively. Here hydrogen atoms were not shown in (a) and (b) to make the illustration more clear.

We evaluated the probability distribution of θ and ψ for the cation alkyl chains P₄₋₁, P₄₋₂, P₄₋₃, P₈, and the anion B₁, B₂ around the AFM tip during scanning. In the case of the cation shown in Figure 8(a), the θ distribution for alkyl chains is dominated by large peaks around $\theta \approx 60^\circ$, 90° , 130° , 90° (orientation I), $\theta \approx 150^\circ$, 90° , 130° , 90° (orientation II), which indicates that two of the cation alkyl chains are orientated perpendicular to the normal vector z , with two other chains tilted pointing to z (see the sketch in Figure 40a). The cation alkyl chains around the tip preferentially orient parallel with the tip scanning route, as the normal load increases. The resulted flat-oriented cation alkyl chains at a higher normal load, would be favorable in reducing friction force, and be responsible for the ‘negative friction-load dependence’. For the anion, two main preferential orientations with tilts exist, i.e., orientation I with peaks at $\psi \approx 50^\circ$, 110° , orientation II with peaks at $\psi \approx 110^\circ$, 135° , corresponding to the dominant orientation of the anions already seen in the

sketch map in Figure 40(b). Specifically, in both orientation I and II of anions, one of the benzene rings points to the scanning tip, leading to an electro-repulsion because of delocalized π electrons in benzene ring and tip, which may contribute to the lower friction. Nevertheless, the distributions of both cations and anions (right in Figure 8a and b) in bulk system show almost no orientation ordering, i.e., no preferred orientation, in comparison with the orientation ordering in near-tip layer.

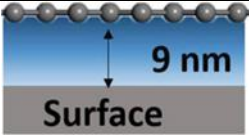
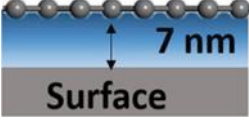
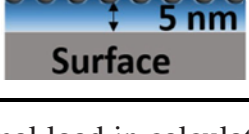
7.3.6 Diffusion Coefficient-Structural Changes

Such structural reorientations observed in Figures 39 and 40 are possible if the diffusion is enhanced for the IL molecules. To support the enhanced diffusion hypothesis for the parallel oriented structure changes of ILs as the AFM tip penetrates the ILs layer at higher loads, we designed three slit-pore models to confine the neat [P4,4,4,8][BScB] using molecular dynamics simulation. The NEMD and the diffusion calculations are connected but not identical, and the diffusion calculations have qualitatively verified the enhanced diffusion mechanism. Our goal is to compare IL diffusion between the tip and the substrate during the AFM tip approaching to help us understand structural changes of ILs. In AFM experiments and NEMD friction calculations, the tip moves closer to the substrate as the external normal load increases. So we employed slit-pore models to mimic the tip approaching the substrate by varying the confinement width.

It may be expected that confined ILs exhibit slower self-diffusion, such as the confined octamethylcyclotetrasiloxane between an AFM gold tip and mica.³⁶ We highlight a substantially enhanced diffusion coefficient in more strongly confined system, i.e., 5 nm slit width. The diffusion in our cases speeds up in the more strongly confined 5 nm slit pore. As shown in **Table 9**, three slit-pore width 5, 7, and 9 nm were modeled. The diffusion coefficients in 5, 7, and 9 nm slit pore are, respectively, $(3.42\text{--}3.94)\times 10^{-12}$, $(1.19\text{--}1.38)\times 10^{-12}$, and $(1.02\text{--}1.20)$

$\times 10^{-12} \text{ m}^2 \text{ s}^{-1}$. One can safely assume that further increase of the slit-pore width in our systems will produce similar diffusion coefficients to the bulk. The repulsive normal loads at 5, 7, and 9 nm slit-pore walls are, respectively, 707, 788, and 810 nN, indicating that larger normal loads limit the ionic mobility to result in smaller diffusion coefficient. Here it is noteworthy that the loads in calculating diffusion coefficient were produced by varying slit-pore widths, different from that in friction calculations which were applied directly by external normal loads.

Table 9. Normal loads and diffusion coefficients of $[\text{P}_{4,4,4,8}][\text{BScB}]$ confined in the slit pore (between tip and substrate), calculated by MD simulations.

Slit width [nm]	Normal load ^{a)} [nN]	Diffusion coefficient (D) [$10^{-12} \text{ m}^2 \text{ s}^{-1}$]
	810	1.02–1.20
	788	1.19–1.38
	707	3.42–3.94

a) Normal load in calculating diffusion coefficient was produced by varying slit-pore widths, different from that in friction calculations which were applied directly by external normal loads.

Both the acceleration and reduction of the diffusion could occur in more strongly confined systems, but the interpretation of diffusion trends varies. For example, some theorists attributed the diffusion enhancement to the tight hydrogen-bonding network in the liquid molecules and the confined space which shields these hydrogen bonds from fluctuations.³⁷ The frictionless surface of the confined walls was also a possible explanation.³⁸ But it was unclear whether the flow enhancement in confined spaces can be attributed simply to the

presence of a nearly frictionless surface.³⁹⁻⁴⁰ The diffusivity increase was also found to be dependent on the liquid polarity.⁴¹ However, it is uncommon to observe an increased internal energy in the confined liquids, while the self-diffusion in confined conditions exceeds that in the bulk phase. Because stronger intermolecular interactions usually imply smaller diffusivity.⁴² Some investigation ascribed the reduced diffusion in nonpolar fluids to the solidification of confined fluid molecules.³⁶ NMR diffusometry experiments showed a higher diffusion coefficient of ethylammonium nitrate ionic liquid confined between parallel glass plates of 4.1 μm as compared with the diffusivity in the bulk. The authors explained the diffusion differences were probably related to electrostatic interactions, hydrogen bonding, nanoscale ordering, structural parameters in confinement.⁴³ Another experimental technique, transmission electron microscopy, suggested that the confined fluid mobility was greatly retarded because of the defects of confined walls.⁴⁴

Therefore, it is difficult to pinpoint a single dominant reason for the diffusion acceleration or reduction, and further experimental and theoretical studies are needed to fully understand varying diffusion phenomena. As for our confined ILs, it is difficult to accurately explain the diffusion acceleration in the confined 5 nm slit pore, but we plan next to calculate the interactive energy of ILs with the tip and substrate. This can be utilized to evaluate the binding strength of the confined ILs to tell if the surface attractive interactions retard the liquid mobility or not.

The enhanced diffusion in the smaller width between the tip and surface in our case led to an increase in the near-surface mobility of ions. The faster overall dynamics of the confined [P_{4,4,4,8}][BScB] system makes the structure change in cations of ILs easier into a parallel orientation as the tip penetrates the ILs layer at higher loads. The resulting parallel orientation of ILs, is thus responsible for the lower friction force⁴⁵⁻⁴⁶ at higher loads than that at lower loads. In addition, the liquid mass transport and diffusion has been found strongly related to the interfacial

friction,⁴⁷⁻⁴⁸ so that the faster diffusion probably also makes a direct contribution to the negative friction-load dependence in our systems.

7.4 Conclusions

We have measured negative “friction–load dependence” of IL/ oil mixtures at Ti interfaces which is associated with the locally structural changes in ILs during approach of an AFM tip. The negative phenomenon was also confirmed by our NEMD simulations, in which the friction force declines as the normal load increases. Both AFM measurements and NEMD simulations showed larger friction forces than the normal loads, which is attributed to the high viscosity. Neither chemical reactions nor morphologies were observed at IL/oil mixtures at Ti interfaces before and after AFM friction measurements. NEMD simulations revealed a structural reorientation of the studied IL as the normal load increases, i.e., the cation alkyl chains of ILs change the orientation to preferentially stay parallel to the tip scanning path, similar to the “blooming lotus leaf.” This reoriented IL structures produce a new sliding interface and reduce the friction force. We further varied the slit-pore width between the tip and the surface using MD simulations to mimic the tip approaching the surface at different loads. And a faster diffusion of ILs was observed in the smaller slit-pore model, which facilitates such structural reorientation at higher normal loads. The resulted new sliding surface to the tip is responsible for the observed smaller friction forces at higher normal loads, i.e., the negative friction–load dependence. A systematic study would be continued, including the type of IL and base oil; the ratio of IL/base oil; the hydrophobic/hydrophilic nature of the tip; the sliding speed of the tip as well as the shape and the contacting surface area; the thickness of the lubricant layer (the IL/base oil mixture); the effect of the supporting substrate.

7.5 References

1. Eswaraiah, V.; Sankaranarayanan, V.; Ramaprabhu, S., Graphene-Based Engine Oil Nanofluids for Tribological Applications. *ACS Appl. Mater. Interfaces* **2011**, *3* (11), 4221.
2. Mate, C. M., *Tribology on the Small Scale : A Bottom up Approach to Friction, Lubrication, and Wear*. Oxford University Press: Oxford, New York, USA, 2008.
3. Gao, J. P.; Luedtke, W. D.; Gourdon, D.; Ruths, M.; Israelachvili, J. N.; Landman, U., Frictional Forces and Amontons' Law: From the Molecular to the Macroscopic Scale. *J. Phys. Chem. B* **2004**, *108* (11), 3410.
4. Deng, Z.; Smolyanitsky, A.; Li, Q. Y.; Feng, X. Q.; Cannara, R. J., Adhesion-Dependent Negative Friction Coefficient on Chemically Modified Graphite at the Nanoscale. *Nat. Mater.* **2012**, *11* (12), 1032.
5. Deng, Z.; Klimov, N. N.; Solares, S. D.; Li, T.; Xu, H.; Cannara, R. J., Nanoscale Interfacial Friction and Adhesion on Supported Versus Suspended Monolayer and Multilayer Graphene. *Langmuir* **2013**, *29* (1), 235.
6. Ye, Z. J.; Martini, A., Atomistic Simulation of the Load Dependence of Nanoscale Friction on Suspended and Supported Graphene. *Langmuir* **2014**, *30* (49), 14707.
7. Tripathi, M.; Awaja, F.; Paolicelli, G.; Bartali, R.; Iacob, E.; Valeri, S.; Ryu, S.; Signetti, S.; Speranza, G.; Pugno, N. M., Tribological Characteristics of Few-Layer Graphene over Ni Grain and Interface Boundaries. *Nanoscale* **2016**, *8* (12), 6646.
8. Thormann, E., Negative Friction Coefficients. *Nat. Mater.* **2013**, *12* (6), 468.
9. Smolyanitsky, A.; Killgore, J. P., Anomalous Friction in Suspended Graphene. *Phys. Rev. B* **2012**, *86* (12), 125432.

10. Smolyanitsky, A.; Zhu, S. Z.; Deng, Z.; Li, T.; Cannara, R. J., Effects of Surface Compliance and Relaxation on the Frictional Properties of Lamellar Materials. *RSC Adv.* **2014**, *4* (51), 26721.
11. Zhou, F.; Liang, Y. M.; Liu, W. M., Ionic Liquid Lubricants: Designed Chemistry for Engineering Applications. *Chem. Soc. Rev.* **2009**, *38* (9), 2590.
12. Li, H.; Somers, A. E.; Howlett, P. C.; Rutland, M. W.; Forsyth, M.; Atkin, R., Addition of Low Concentrations of an Ionic Liquid to a Base Oil Reduces Friction over Multiple Length Scales: A Combined Nano- and Macrotribology Investigation. *Phys. Chem. Chem. Phys.* **2016**, *18* (9), 6541.
13. Tome, L. C.; Marrucho, I. M., Ionic Liquid-Based Materials: A Platform to Design Engineered CO₂ Separation Membranes. *Chem. Soc. Rev.* **2016**, *45* (10), 2785.
14. Somers, A. E.; Khemchandani, B.; Howlett, P. C.; Sun, J. Z.; MacFarlane, D. R.; Forsyth, M., Ionic Liquids as Antiwear Additives in Base Oils: Influence of Structure on Miscibility and Antiwear Performance for Steel on Aluminum. *ACS Appl. Mater. Interfaces* **2013**, *5* (22), 11544.
15. Zhang, S. G.; Zhang, J. H.; Zhang, Y.; Deng, Y. Q., Nanoconfined Ionic Liquids. *Chem. Rev.* **2017**, *117* (10), 6755.
16. Shah, F. U.; Glavatskih, S.; MacFarlane, D. R.; Somers, A.; Forsyth, M.; Antzutkin, O. N., Novel Halogen-Free Chelated Orthoborate-Phosphonium Ionic Liquids: Synthesis and Tribophysical Properties. *Phys. Chem. Chem. Phys.* **2011**, *13* (28), 12865.
17. Shah, F. U.; Gnezdilov, O. I.; Filippov, A., Ion Dynamics in Halogen-Free Phosphonium Bis(Salicylato)Borate Ionic Liquid Electrolytes for Lithium-Ion Batteries. *Phys. Chem. Chem. Phys.* **2017**, *19* (25), 16721.
18. Shah, F. U.; Gnezdilov, O. I.; Gusain, R.; Filippov, A., Transport and Association of Ions in Lithium Battery Electrolytes Based on Glycol Ether Mixed with Halogen-Free Orthoborate Ionic Liquid. *Sci. Rep.* **2017**, *7*, 16340.

19. Liu, W. H.; Bonin, K.; Guthold, M., Easy and Direct Method for Calibrating Atomic Force Microscopy Lateral Force Measurements. *Rev. Sci. Instrum.* **2007**, *78* (6), 063707.
20. Ewen, J. P.; Heyes, D. M.; Dini, D., Advances in Nonequilibrium Molecular Dynamics Simulations of Lubricants and Additives. *Friction* **2018**, *6* (4), 349.
21. Dong, Y. L.; Li, Q. Y.; Martini, A., Molecular Dynamics Simulation of Atomic Friction: A Review and Guide. *J. Vac. Sci. Technol. A* **2013**, *31* (3), 030801.
22. Ye, Z. J.; Egberts, P.; Han, G. H.; Johnson, A. T. C.; Carpick, R. W.; Martini, A., Load-Dependent Friction Hysteresis on Graphene. *ACS Nano* **2016**, *10* (5), 5161.
23. Hockney, R. W.; Eastwood, J. W., *Computer Simulation Using Particles*. 2nd ed.; IOP: Bristol, U.K: 1988.
24. Buettner, K. M.; Valentine, A. M., Bioinorganic Chemistry of Titanium. *Chem. Rev.* **2012**, *112* (3), 1863.
25. Chen, Q.; Moore, J. D.; Liu, Y. C.; Roussel, T. J.; Wang, Q.; Wu, T.; Gubbins, K. E., Transition from Single-File to Fickian Diffusion for Binary Mixtures in Single-Walled Carbon Nanotubes. *J. Chem. Phys.* **2010**, *133* (9), 094501.
26. An, R.; Huang, L. L.; Long, Y.; Kalanyan, B.; Lu, X. H.; Gubbins, K. E., Liquid-Solid Nanofriction and Interfacial Wetting. *Langmuir* **2016**, *32* (3), 743.
27. Carpick, R. W.; Agrait, N.; Ogletree, D. F.; Salmeron, M., Variation of the Interfacial Shear Strength and Adhesion of a Nanometer-Sized Contact. *Langmuir* **1996**, *12* (13), 3334.
28. Lhermerout, R.; Diederichs, C.; Perkin, S., Are Ionic Liquids Good Boundary Lubricants? A Molecular Perspective. *Lubricants* **2018**, *6* (1), 9.
29. Smith, A. M.; Lovelock, K. R. J.; Gosvami, N. N.; Welton, T.; Perkin, S., Quantized Friction across Ionic Liquid Thin Films. *Phys. Chem. Chem. Phys.* **2013**, *15* (37), 15317.

30. Cooper, P. K.; Li, H.; Rutland, M. W.; Webber, G. B.; Atkin, R., Tribotronic Control of Friction in Oil-Based Lubricants with Ionic Liquid Additives. *Phys. Chem. Chem. Phys.* **2016**, *18* (34), 23657.
31. Mattevi, C.; Eda, G.; Agnoli, S.; Miller, S.; Mkhoyan, K. A.; Celik, O.; Mastrogiovanni, D.; Granozzi, G.; Garfunkel, E.; Chhowalla, M., Evolution of Electrical, Chemical, and Structural Properties of Transparent and Conducting Chemically Derived Graphene Thin Films. *Adv. Funct. Mater.* **2009**, *19* (16), 2577.
32. Hjalmarsson, N.; Atkin, R.; Rutland, M. W., Is the Boundary Layer of an Ionic Liquid Equally Lubricating at Higher Temperature? *Phys. Chem. Chem. Phys.* **2016**, *18* (13), 9232.
33. Black, J. M.; Zhu, M. Y.; Zhang, P. F.; Unocic, R. R.; Guo, D. Q.; Okatan, M. B.; Dai, S.; Cummings, P. T.; Kalinin, S. V.; Feng, G.; Balke, N., Fundamental Aspects of Electric Double Layer Force-Distance Measurements at Liquid-Solid Interfaces Using Atomic Force Microscopy. *Sci. Rep.* **2016**, *6*, 32389.
34. Vilhena, J. G.; Pimentel, C.; Pedraz, P.; Luo, F.; Serena, P. A.; Pina, C. M.; Gnecco, E.; Perez, R., Atomic-Scale Sliding Friction on Graphene in Water. *ACS Nano* **2016**, *10* (4), 4288.
35. Li, H.; Wood, R. J.; Rutland, M. W.; Atkin, R., An Ionic Liquid Lubricant Enables Superlubricity to Be "Switched on" in Situ Using an Electrical Potential. *Chem. Commun.* **2014**, *50* (33), 4368.
36. Xu, R. G.; Leng, Y. S., Solvation Force Simulations in Atomic Force Microscopy. *J. Chem. Phys.* **2014**, *140* (21), 214702.
37. Hummer, G.; Rasaiah, J. C.; Noworyta, J. P., Water Conduction through the Hydrophobic Channel of a Carbon Nanotube. *Nature* **2001**, *414* (6860), 188.

38. Majumder, M.; Chopra, N.; Andrews, R.; Hinds, B. J., Enhanced Flow in Carbon Nanotubes. *Nature* **2005**, *438* (7064), 44.
39. Holt, J. K.; Park, H. G.; Wang, Y. M.; Stadermann, M.; Artyukhin, A. B.; Grigoropoulos, C. P.; Noy, A.; Bakajin, O., Fast Mass Transport through Sub-2-Nanometer Carbon Nanotubes. *Science* **2006**, *312* (5776), 1034.
40. Sparreboom, W.; van den Berg, A.; Eijkel, J. C. T., Principles and Applications of Nanofluidic Transport. *Nat. Nanotech.* **2009**, *4* (11), 713.
41. Chaban, V. V.; Prezhdo, O. V., Nanoscale Carbon Greatly Enhances Mobility of a Highly Viscous Ionic Liquid. *ACS Nano* **2014**, *8* (8), 8190.
42. Servantie, J.; Muller, M., Temperature Dependence of the Slip Length in Polymer Melts at Attractive Surfaces. *Phys. Rev. Lett.* **2008**, *101* (2), 026101.
43. Filippov, A.; Gnezdilov, O. I.; Hjalmarsen, N.; Antzutkin, O. N.; Glavatskih, S.; Furo, I.; Rutland, M. W., Acceleration of Diffusion in Ethylammonium Nitrate Ionic Liquid Confined between Parallel Glass Plates. *Phys. Chem. Chem. Phys.* **2017**, *19* (38), 25853.
44. Naguib, N.; Ye, H. H.; Gogotsi, Y.; Yazicioglu, A. G.; Megaridis, C. M.; Yoshimura, M., Observation of Water Confined in Nanometer Channels of Closed Carbon Nanotubes. *Nano Lett.* **2004**, *4* (11), 2237.
45. Iacob, C.; Sangoro, J. R.; Kipnusu, W. K.; Valiullin, R.; Karger, J.; Kremer, F., Enhanced Charge Transport in Nano-Confined Ionic Liquids. *Soft Matter* **2012**, *8* (2), 289.
46. Ghoufi, A.; Szymczyk, A.; Malfreyt, P., Ultrafast Diffusion of Ionic Liquids Confined in Carbon Nanotubes. *Sci. Rep.* **2016**, *6*, 28518.

47. Thomas, M.; Corry, B.; Hilder, T. A., What Have We Learnt About the Mechanisms of Rapid Water Transport, Ion Rejection and Selectivity in Nanopores from Molecular Simulation? *Small* **2014**, *10* (8), 1453.
48. Verweij, H.; Schillo, M. C.; Li, J., Fast Mass Transport through Carbon Nanotube Membranes. *Small* **2007**, *3* (12), 1996.

Chapter 8: Conclusions and Outlook

8.1 Conclusions

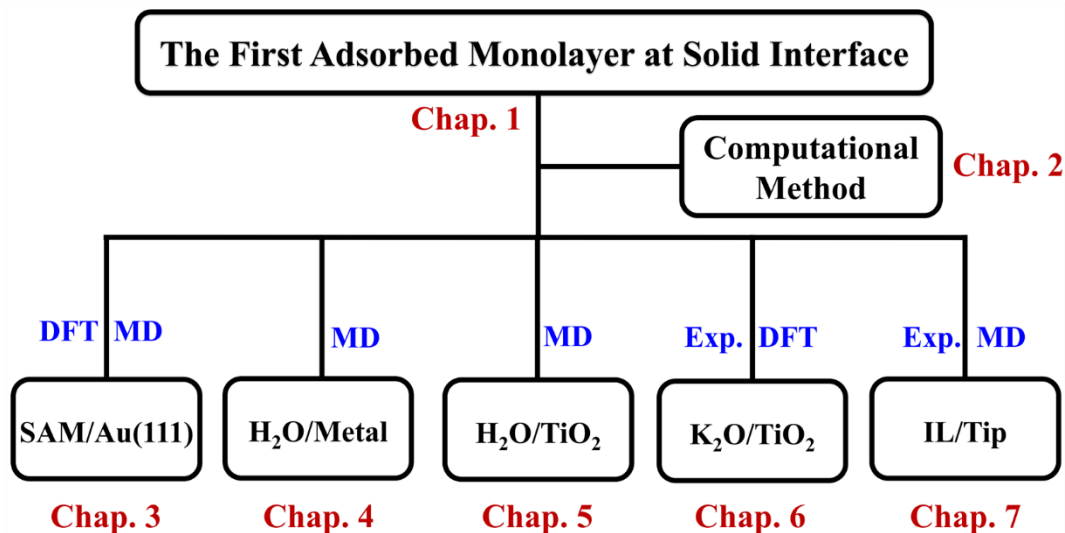


Figure 41. The tree of dissertation outline with the color codes: black-the keyword for the topic; blue-the computational method; red-the chapter number.

As shown in Figure 41, in this dissertation, we have been applying different computational methods, coupled with the experiments, to study the structures and properties of the first adsorbed monolayer at distinct solid interfaces. The results can be summarized as follows:

- a. Periodic ab initio DFT calculations were utilized to develop a new atomistic force field model for alkanethiolate (AT) SAMs on a reconstructed Au(111) surface. The new force field parameters were carefully trained to reproduce the key features, including vibrational spectra and torsion energy profiles of ethylthiolate (C_2S) in the bridge or staple motif model on the Au(111) surface, wherein, the force constants of the bond and angle terms were trained by matching the vibrational spectra, while the torsion parameters of the dihedral angles were trained via fitting the torsion energy profiles from DFT calculations. To validate the developed force field parameters, we performed classical MD simulations for both pristine and reconstructed Au–S interface models

with a $(2\sqrt{3}\times 3)$ unit cell, which includes four dodecanethiolate ($C_{10}S$) molecules on the Au(111) surface. The simulation results showed that the geometrical features of the investigated Au–S interface models and structural properties of the $C_{10}S$ SAMs are in good agreement with the ab initio MD studies.

b. We report a peculiar wetting phenomenon for Pd(100), Au(100), and their bimetallic Pd(100)/Au(100) surfaces. For pristine Pd(100), there is a water droplet coexisting with the well-defined FAWL on the surface, whereas, on pristine Au(100), the FAWL is fully wet by the water film. When the metal surfaces are uniformly compressed to different strains, we observe the wetting transition for both Pd(100) (hydrophobicity-hydrophilicity) and Au(100) (hydrophilicity-hydrophobicity) surfaces. As for the bimetallic Pd(100)/Au(100), there is also a well-designed FAWL distributed on the surface, but the other water molecules would unexpectedly shift from Pd(100) to Au(100) to form a droplet solely on Au(100) surface. Such distinct phenomenon is supposed to result from the hydrophilicity difference of FAWL on these two metal surfaces.

c. The classical MD simulations were applied to study the properties of FAWL at four TiO_2 surfaces. The calculation results reveal the characteristics of water: (a) rutile (110), O_w atoms of water are located at the top sites of Ti_{5c} , and two H atoms facing away from the surface; (b) rutile (011), water molecules lean on the surface with one H atoms directing to the surface O_{2c} atoms and the other one pointing towards to bulk water; (c) TiO_2 -B (100), water forms the “H-up” and “H-down” configurations. The “H-up” configuration has the O_w atoms atop the Ti_{5c} sites with two H atoms pointing to bulk water. The “H-down” configuration has both H atoms point to the surface O_{2c} sites; (d) TiO_2 -B (001), water has a random distribution, yet, the in-layer HBs promote the formation of small water clusters near the surface. The vibrational spectra, the HB network strength and the HB lifetime are also analyzed in this work. A significant red shift of the vibrational spectra

suggests an enhanced HB network, which also results in a much longer HB lifetime. For the studied surfaces, the TiO₂-B (100) has a most stable HB network, which is evidenced the slowest decay of the HB lifetime.

d. We have successfully synthesized the TiO₂ nanowhiskers, which show excellent SERS properties. The enhancement factor, an index of SERS performance, is 4.96×10^6 for methylene blue molecule detecting, with a detection sensitivity around $10^{-7} \text{ mol} \cdot \text{L}^{-1}$. Characterizations, such as XRD, Raman, TEM, UV–vis and Zeta potential measurement, have been performed to decrypt structural and chemical characteristics of the newly synthesized TiO₂ nanowhiskers. The photoabsorption onset of MB adsorbed TiO₂ nanowhiskers was similar to that of bare TiO₂ nanowhiskers. In addition, no new band was observed from the UV–vis of MB modified TiO₂ nanowhiskers. Both results suggest that the high enhancement factor cannot be explained by the charge-transfer mechanism. With the support of ab initio DFT calculations, we reveal that interfacial potassium is critical to maintain thermal stability of the anatase phase up to 900 °C. In addition, the deposition of potassium results in a negatively charged TiO₂ nanowhisker surface, which favors specific adsorption of methylene blue molecules and significantly improves SERS performance via the electrostatic adsorption effect.

e. The atomic force microscopy experiments and nonequilibrium molecular dynamics (NEMD) simulations demonstrate a negative friction–load dependence to ionic liquid (IL)–glycol ether mixtures, that is, the friction decreases as the normal load increases. NEMD simulations reveal a structural reorientation of the studied IL: as the normal load increases, the cation alkyl chains of ILs change the orientation to preferentially parallel to the tip scanning path. The flat-oriented IL structures, similar to the “blooming lotus leaf,” produce a new sliding interface and reduce the friction. A further MD simulation is carried out by adopting slit-pore models to mimic

the tip approaching process to confirm the dynamics of ILs. A faster diffusion of ILs in the smaller slit pore is observed. The faster diffusion of ILs in the more confined slit pore facilitates the structural reorientation of ILs. The resulted new sliding surface is responsible for the observed smaller friction at higher loads, also known as the negative friction–load dependence. These findings provide a fundamental explanation to the role of ILs in interfacial lubrications.

8.2 Outlook

In this dissertation, we developed the force field parameters for the thiolate/defective Au(111) interface. Based on the newly-developed parameters, it would be interesting to investigate the diffusion of ozone molecules on the SAMs surface. It would be also important to explore the role of grain boundary within SAMs on the diffusion motions and the reaction mechanism at the Au-S interface. It is reported that, when the SAMs are exposed to the air for a long time, they would be oxidized by the ozone molecules in the air. Till now, only few theoretical papers report the oxidation reaction at the Au-S interface.

In Chapter 4, we studied the unique wetting transition of water molecules on Pd(100) and Au(100) surfaces. On the other hand, recent studies have shown that the graphene-based 2D materials are capable of protecting metal substrate from corrosion, but little is known about underlying mechanisms and how intrinsic defects influence its anticorrosion capacity. Therefore, it would also be very interesting to investigate the behaviors of water molecules on graphene-coated metal surfaces and explore How the structural defects within graphene influence the adsorption, diffusion, and reaction of water molecules on the surface.

Titanium dioxide, as an important semiconductor metal oxide, has been widely investigated in the field of photocatalysis. It has been shown experimentally that oxygen vacancy is one of the

most important and is supposed to be the prevalent defect in titanium dioxide. However, it is still unclear and challenging to understand on how the oxygen vacancy affects the photocatalysis reaction. It would be interesting to perform reactive MD simulations to study the H₂O interactions with the defective TiO₂ surfaces. The reactive force field parameters may need to re-trained to describe the interactions accurately.

Finally, more efforts could be made to understand the behaviors of water molecules on the K₂O-coated TiO₂ surfaces. As discussed in Chapter 6, when the TiO₂ surface is covered by a monolayer K₂O, it can significantly enhance the SERS performance of TiO₂ surface. On the other hand, prior studies have shown that the pre-adsorbed potassium would remarkably influence the water dissociation. In this context, it would be quite interesting to have detailed insights into the interactions on the surface of K₂O/TiO₂ nanocomposites.